Doctoral Thesis

Provenance analysis and detrital zircons
Keys to the tectonic setting of the Makran and Sistan basins in Iran

Author(s):
Mohammadi, Ali

Publication Date:
2016

Permanent Link:
https://doi.org/10.3929/ethz-a-010593946

DISS. ETH NO. 22962

PROVENANCE ANALYSIS AND DETRITAL ZIRCONS: KEYS TO THE TECTONIC SETTING OF THE MAKRAN AND SISTAN BASINS IN IRAN

A thesis submitted to attain the degree of

DOCTOR OF SCIENCES of ETH ZURICH

(Dr. sc. ETH Zurich)

Presented by

ALI MOHAMMADI

M.Sc. in Geology. University of Tehran

Born on *20.09.1979*

citizen of

Iran

Accepted on the recommendation of

Prof. Dr. Jean-Pierre Burg, ETH Zurich, Switzerland (Examiner)

Prof. Dr. Wilfried Winkler, ETH Zurich, Switzerland (Co-examiner)

Prof. Dr. Yani Najman, Lancaster University, UK (Co-examiner)

Prof. Dr. Barbara Carrapa, University of Arizona, USA (Co-examiner)

2016

FOR MY PARENTS.

Abstract

The Makran Accretionary Wedge (MAW), presumably the largest accretionary complex in the world and the Neh Accretionary Complex, a part of the Sistan Suture Zone (SSZ), are located in southeastern and eastern Iran, respectively. The provenance analysis of the thick turbiditic sedimentary rocks in these accretionary complexes permits understanding the Cretaceous to Paleogene geological evolution, the geodynamic context and the tectonic-sedimentation relationships. The multidisciplinary provenance study, including sandstone framework, heavy mineral analysis, in situ U-Pb dating of detrital zircon and Hf isotopic ratios of dated zircons, was undertaken on Upper Cretaceous-Miocene deep marine turbiditic and deltaic sandstones of MAW and the Eocene-Oligocene turbiditic sandstones of southern part of the SSZ.

Two main detrital zircon age populations have been identified in the Upper Cretaceous-Oligocene sedimentary rocks in the Makran basin. Abundant Middle Jurassic detrital zircons with Hf isotopic compositions similar to continental crust, suggesting a rifting related magmatic provenance. Upper Cretaceous-Eocene detrital zircons with Hf isotopic compositions similar to continental crust and non-depleted mantle, suggesting a continental magmatic arc provenance. Moreover, the heavy mineral assemblages, Cr-spinel, and blue amphibole disclose ophiolite and high pressure-low temperature metamorphic rocks as supplementary provenance. Upper Cretaceous-Eocene magmatic rocks outcropping to the north of the Jaz Murian depression have been attributed to the Upper Cretaceous-Eocene arc related magmatism. In this present study the arc system has been recognized as the ″North Makran continental arc″. The change in tectonic settings from the Jurassic extension to the Late Cretaceous compression is attributed to the convergence between Arabia and Eurasia which commenced during the Late Cretaceous. The Miocene sandstones show recycling and cannibalism in the basin.

Two main detrital zircon ages have been identified in the Eocene-Oligocene sedimentary rocks of the Neh Accretionary Complex. Abundant Upper Cretaceous detrital zircons with Hf isotopic compositions similar to oceanic crust and depleted mantle suggest an intra-oceanic island arc provenance. Eocene detrital zircons with Hf isotopic compositions similar to continental crust and non-depleted mantle suggest a transitional-continental magmatic arc provenance. A similar island arc-continental arc evolution at the same time is reported for the Chagai-Raskoh arc, on the nearby Pakistan-Afghanistan border. This change in provenance is attributed to the Paleocene (65-55 Ma) collision between the Afghan plate and an intra-oceanic island arc. Furthermore heavy mineral assemblages and Cr-spinel disclose ophiolite as a subsidiary source. The westward continuation of the Chagai-Raskoh arc system, along with the associated ophiolites have been recognized as the source of detritus in the Neh Accretionary Complex.

New U-Pb measurements on zircons yield Eocene and Oligocene (ca. 40.5-44.3 Ma and ca. 28.9-30.9 Ma) crystallization ages for the Zehdan and Sah Kuh granitoids. Eocene plutons represent mantle magmas contaminated by ca. 50% of melt derived from the turbidites of the accretionary wedge in which they have been intruded. The wide range of rock compositions has been attributed to the interaction of mantle magmas with crustal turbiditic melts. Oligocene plutons represent mantle derived magmas assimilated by the surrounding turbidites. The rare setting of within-wedge intrusions is attributed to mantle upwelling reaching wedge sediments at the inception of delamination processes, which sign the end of subduction-related deformational and thermal events in the Sistan Suture Zone. This integrated provenance analysis, petrographic, geochronological and geochemical studies shed light on the evolution of the Tethys Ocean segments in SE Iran and provides constraints in assessing models for tectonic and magmatic events during plate interaction and lithospheric behaviors.

Zusammenfassung

Der vermutlich grösste Akkretionskomplex der Welt, der Akkretionskeil im Makran (MAW), und der Neh-Akkretionskomplex, als Teil der Sistan Suturzone (SSZ), befindet sich im Südosten bzw. Osten Irans. Provenanzanalyse der mächtigen turbiditischen Sedimente in diesen Akkretionskomplexen erlaubt es, die kretazische bis paläogene geologische Evolution, den geodynamischen Kontext und die tektono-sedimentären Beziehungen nachzuvollziehen. Die multidisziplinäre Provenanzanalyse, welche die Analyse der Sandsteingefüge und Schwermineralien, in-situ U-Pb Datierung an detritischen Zirkonen und Hf-Isotopenverhältnisse der datierten Zirkone beinhaltet, wurde an spät-kretazischen bis miozänen tiefmarinen Turbiditen und deltaischen Sandsteinen, und an eozän-oligozänen turbiditischen Sandsteinen des südlichen Teils der SSZ vorgenommen.

In den spät-kretazischen bis oligozänen Sedimenten des Makran-Beckens wurden hauptsächlich zwei detritische Zirkonpopulationsalter gefunden: (1) Reichlich vorhandene detritische Zirkone aus dem mittleren Jura mit Hf-Isotopenzusammensetzungen wie die kontinentale Kruste deuten auf eine magmatische Herkunft während eines Riftings; (2) Spät-kretazische bis eozäne detritische Zirkone mit Hf-Isotopenzusammensetzungen wie die kontinentale Kruste und ein nicht-abgereicherter Mantel deuten auf die Herkunft aus einem kontinentalen magmatischen Bogen. Ausserdem enthüllen Schwermineralvereinigungen, wie Cr-Spinel und blaue Amphibole, ophiolithische und hochdruck-niedrigtemperatur metamorphe Gesteine als zusätzliche Quelle. Spät-kretazische bis eozäne magmatische Gesteine, die im Norden der Jaz-Murian Senke aufgeschlossen sind, wurden dem spät-kretazischen bis eozänen Bogenmagmatismus zugeschrieben. In dieser Untersuchung konnte das Bogensystem als ″Nord-Makran Kontinentalbogen″ identifiziert werden. Die Änderung der tektonischen Konfiguration, von jurassischer Extension zu spät-kretazischer Kompression, wird der Konvergenz zwischen Arabien und Eurasien, welche in der späten Kreide begann, zugeschrieben. Die miozänen Sandsteine zeigen Recycling und Kannibalismus im Becken.

In den eozänen bis oligozänen Sedimenten des Neh-Akkretionskomplexs wurden hauptsächlich zwei detritische Zirkonpopulationsalter gefunden. Reichlich vorhandene detritische Zirkone aus der späten Kreide mit Hf-Isotopenzusammensetzungen wie die ozeanische Kruste und der abgereicherte Mantel deuten auf eine Herkunft aus einem intra-ozeanischen Bogen. Eozäne detritische Zirkone mit Hf-Isotopenzusammensetzungen wie die kontinentale Kruste und ein nicht-abgereicherter Mantel deuten auf die Herkunft aus einem vorübergehenden kontinentalen magmatischen Bogen. Eine ähnliche Entwicklung, von Inselbogen zu kontinentalem Bogen, zeigt der Chagai-Raskoh Bogen in der Nähe zur pakistanisch-afghanischen Grenze. Die Änderung der Herkunft wird der paläozänen (65-55 Ma) Kollision zwischen der Afghan-Platte und dem intra-ozeanischen Bogen zugeschrieben. Ausserdem zeigen

Schwermineralvereinigungen mit Cr-Spinel und blauen Amphibolen eine untergeordnet ophiolithische Quelle. Die westliche Fortsetzung des Chagai-Raskoh Bogensystems, zusammen mit den assoziierten Ophiolithen, wurden als Detritusquelle im Neh-Akkretionskomplex erkannt.

Neue U-Pb-Messungen an Zirkonen ergeben eozäne und oligozäne (ca. 40.5-44.3 Ma und ca. 28.9-30.9 Ma) Kristallisationsalter für die Zahedan und Sah Kuh Granitoide. Eozäne Plutone repräsentieren Mantelschmelzen, wobei ca. 50% davon mit Schmelzen aus den Turbiditen des Akkretionskeils kontaminiert sind, in welchen sie intrudierten. Die grosse Bandbreite an Gesteinszusammensetzungen wurde der Wechselwirkung zwischen den Mantel- und krustalen turbiditischen Schmelzen zugeschrieben. Oligozäne Plutone repräsentieren aus dem Mantel stammende Magmen, welche von den umgebenden Turbiditen assimiliert wurden. Die seltene Konfiguration einer Intrusion in den Keil wird dem Mantelauftrieb zugeschrieben, der die Keilsedimente zu Beginn des Delaminationsprozesses erreicht, was wiederum das Ende des subduktions-bezogenen Deformations- und thermischen Events in der Sistan Suturzone kennzeichnet. Die hier angewandte Integration der Provenanzanalyse, der petrographischen, geochronologischen und geochemischen Studien wirft Licht auf die Entwicklung der Tethys-Ozean-Segmente im Südosten Irans und liefert neue Rahmenbedingungen für die Beurteilung tektonischer und magmatischer Modelle während Platten-Wechselwirkungen und für die Beurteilung lithosphärischen Verhaltens.

Contents

Chapter I

Introduction

1. Introduction

1.1 General introduction

This thesis deals with the Makran Accretionary Wedge in southeast Iran and in the southern part of the Sistan Suture Zone, also exposed in southeast Iran. The analytical work is dedicated to the provenance analysis and the age and source determination of detrital zircons in sandstones of the thick turbiditic sedimentary rocks to ascertain the tectonic settings of the studied basins and of the source areas.

1.1.1 Provenance of sediments

The term of provenance is derived from the Latin verb *provenire*, meaning to originate from. Sedimentary provenance studies were first published in the 19th century as microscopic investigation of heavy minerals in recent sands (Ludwig, 1874; Meunier, 1877). The technique has considerably advanced since Dickinson (1970) and Pettijohn et al. (1974). These authors have shown that detrital modes of sandstones, determined by the Gazzi-Dickinson method, are useful to identify the tectonic setting of the provenance of a suite of sandstones and reconstruct the sediment history from erosion of parent rocks to burial of their detritus. Clastic sedimentary sequences shed from orogenic belts provide a rich, and arguably unique record of crustal exhumation and erosion. In particular, the detrital content of sandstones mirrors the exposed rocks that supply grains to the studied basins (Dickinson and Valloni, 1980). The quantification of detrital components provides neither an estimation of the age nor the nature of the parental magmas of the source-rocks. For standard provenance analysis, researchers combined quantification of detrital assemblages with other methods (paleocurrent data, heavy mineral study, detrital zircon U-Pb ages, Hf-isotopic ratios, geochemistry of detrital zircons and several other method) to reconstruct the paleogeography of the source-rock and the geodynamic evolution of the investigated area.

1.1.2 Aims of the thesis

The Makran is the critical link between the greater Himalayan orogenic system and the Zagros fold and thrust system, and it is one of the best exposed and thickest accretionary complex in the world. Makran accretionary wedge joins the the Sistan suture zone at its northern margin nearly on the Iran Pakistan border (Fig. 1.1). The Sistan basin contains abundant turbidite units of Eocene to Oligocene age, which may or may not correlate with the onset of major turbidite deposition in the Makran basin during Late Oligocene. The present study evaluated together these two adjacent basins to better understand their (i) Cretaceous to Paleogene geological history, geodynamic context at that time, (iii) the source of the thick turbiditic sedimentary rocks, and (iv) their tecono-sedimentay relationships. Furthermore the south Sistan Suture Zone exposes granitoids intruded into Eocene sedimentary rocks. Studying these intrusions will provide information on the tectono-magmatic history of this part of the Tethys collisional system (Fig. 1.1).

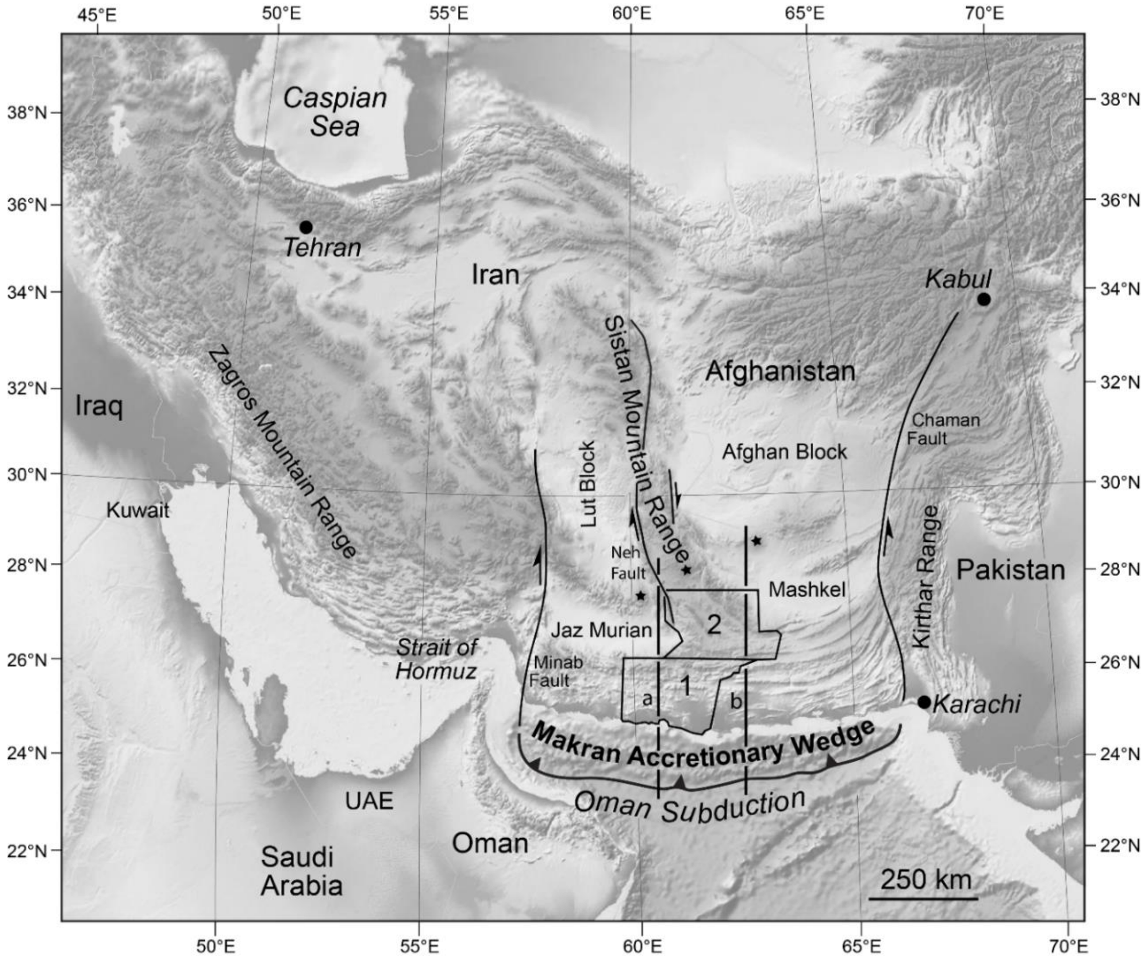

Figure 1.1: Tectonic setting of the Makran Accretionary Wedge and the Sistan Mountain Range. Framed: 1= studied area of onshore Makran; 2= studied area of Sistan Basin. Stars are the three major and active volcanic centres of Makran magmatic arc. a and b= Cross-sections in Figure 1.3. Background: shaded relief map ETOPO1 (http://www.ngdc.noaa.gov/mgg/global/relief/ETOPO1).

A multidisciplinary study combining fieldwork, sandstone framework analysis, heavy minerals determination and U-Pb age and Hf isotopic composition of detrital zircons were carried out to answer the following questions:

- What are the sources of the thick clastic sediments in the Makran accretionary wedge and the south Sistan basin (Neh accretionary wedge)?

- What is the tectono-sedimentary development of the Makran and south Sistan basins?

- What is the differences between the Iranian and Pakistani parts of the Makran wedge?

- What is the temporal relationship between the Makran and the Sistan basins?

- What are the timing and the spatial distribution of magmatic events and how do they fit the tectonic history of Tethys?

- When did the change from extension to compression take place?

- Can this change be depicted by lithological changes in the source area?

The present PhD thesis seeks answers in the provenance of Upper Cretaceous to Miocene siliciclastic sandstones of the onshore Makran accretionary wedge and the South Sistan Basin, in Iran. Results combine field work data, modal framework grain composition of sandstones, heavy mineral analysis and zircon single grain (ICP-MS laser ablation U-Pb age and Hf isotopic ratio) studies. This thesis will:

- Provide evidence from Hf-isotopic compositions of dated detrital zircons for different compositions of source rocks.

- Evaluate the timing and spatial distribution of magmatic and metamorphic events, separating rift-related continental magmatism to the north of Makran, and oceanic island arc and continental arc magmatism in the Chagai-Raskoh belt (northeast of South Sistan Basin).

- Evaluate the tectono-magmatic model of Late Cretaceous and Paleogene magmatism along the northern margin of the Tethys Ocean and its implications to clarify the geodynamics setting.

- Understand the differences between the western Makran (Iran), the eastern Makran (Pakistan), and the South Sistan Suture Zone to reconstruct the geodynamic settings since the Late Cretaceous.

- Determine the petrological and geochemical features and constrain with U-Pb dating of magmatic zircons the crystallization ages of the Zahedan-Shah Kuh magmatic belt in the south Sistan Basin.

- Finally identify the origin and tectonic affiliation of the Zahedan - Shah Kuh magmatic belt in the Sistan suture zones.

1.2 Study area

The provenance of the detrital material in the Makran accretionary wedge has been a subject of research for decades. It has been suggested that pre-Miocene sedimentary rocks in Makran were supplied from the Himalaya through the Paleo-Indus submarine fan, whereas Miocene to recent deposits are reworked older sedimentary rocks of the accretionary wedge (Fig. 1.2; Critelli et al., 1990; Qayyum et al., 2001; Grigsby et al., 2004; Ellouz-Zimmermann et al., 2007a; Ellouz-

Zimmermann et al., 2007b; Kassi et al., 2007; Carter et al., 2010; Kassi et al., 2013; Kassi et al., 2015). Much less work has been done in the Sistan Mountains (Carter et al., 2010). According to Carter et al. (2010) sedimentary rocks of the Eocene and Oligocene sedimentary rocks of the South Sistan Basin were also supplied from the Himalaya through the Paleo-Indus submarine fan.

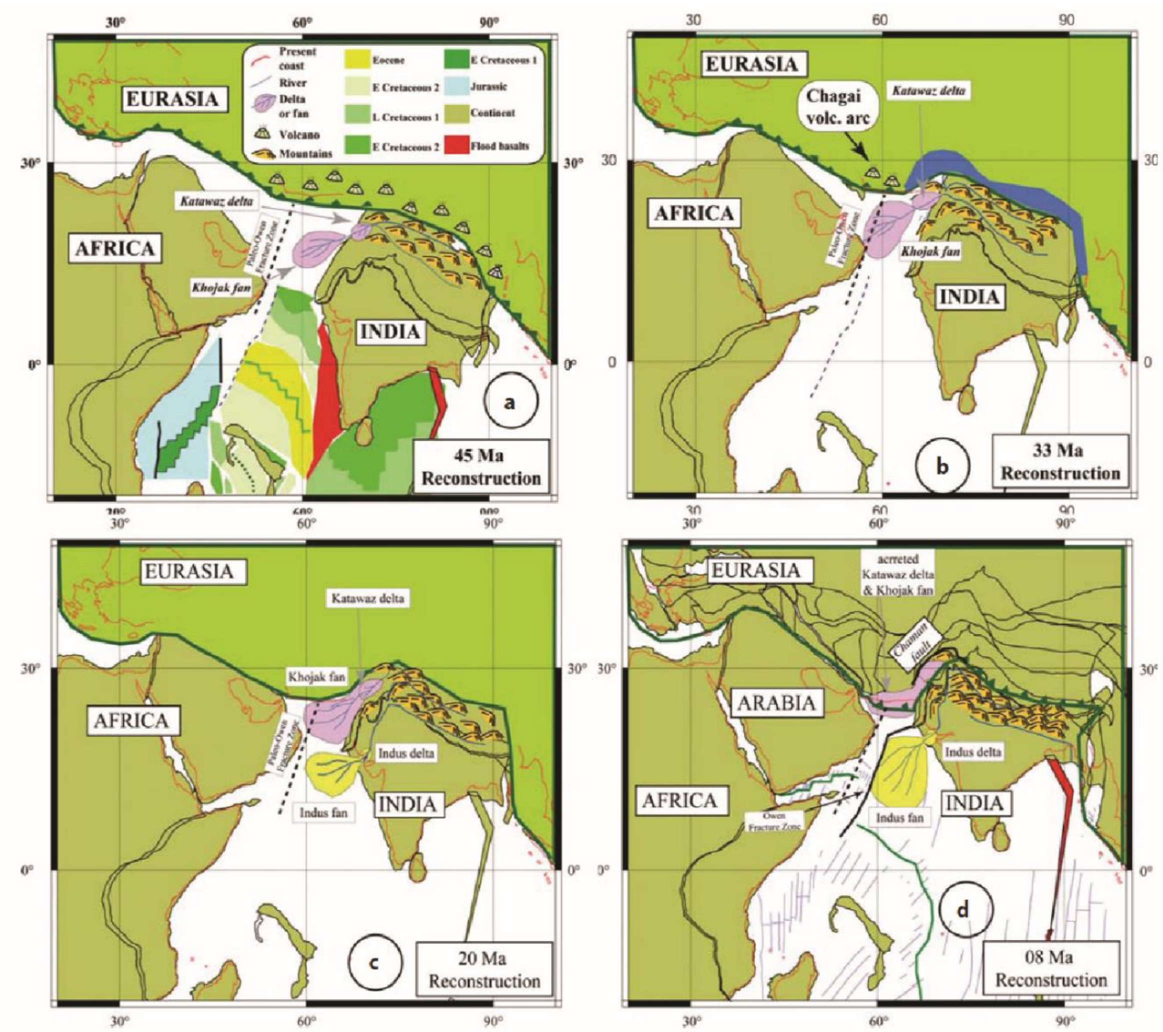

Figure 1.2: Figure 2 of Ellouz-Zimmermann et al. (2007a). Plate kinematics in a fixed Eurasia reference frame and sedimentary inputs in the Arabian Sea Eocene time.

1.2.1 Tectonic Overview

The active Makran accretionary wedge, located in SE Iran and SW Pakistan extends ~ 1000 km along strike between the Minab-Zendan dextral fault system to the West and the Chaman sinistral fault in the East. (Fig. 1.1). Makran belongs to the Alpine-Himalayan orogenic system and results from the convergence between the Arabian and Eurasian plates (White, 1982; Platt et al., 1985). The Makran accretionary wedge is more than 350 km wide along the shortening direction and grows both vertically and laterally by scraping sediment material of the northwards subducting Arabian lithosphere (Platt et al., 1985). The accretionary wedge is divided into an active southern part (submarine wedge; 100-150 km) and a passive northern part (onshore wedge; 200-250km), which are separated by a south-dipping normal faults close to today's shoreline (Kukowski et al., 2001; Ellouz-Zimmermann et al., 2007a; Grando and McClay, 2007; Bourget et al., 2013). The present rate of convergence between Arabia to the south and Eurasia to the north is about 2 cm a^{-1} (Vigny et al., 2006; Masson et al., 2007). The Makran subduction zone exhibits a strong segmentation between east and west seismic behaviors (Byrne et al., 1992). No large-magnitude earthquake is known in western Makran where the recorded seismicity is sparse (Fig. 1.3a). In contrast, big earthquakes and active seismicity characterize eastern Makran (Fig. 1.3b).

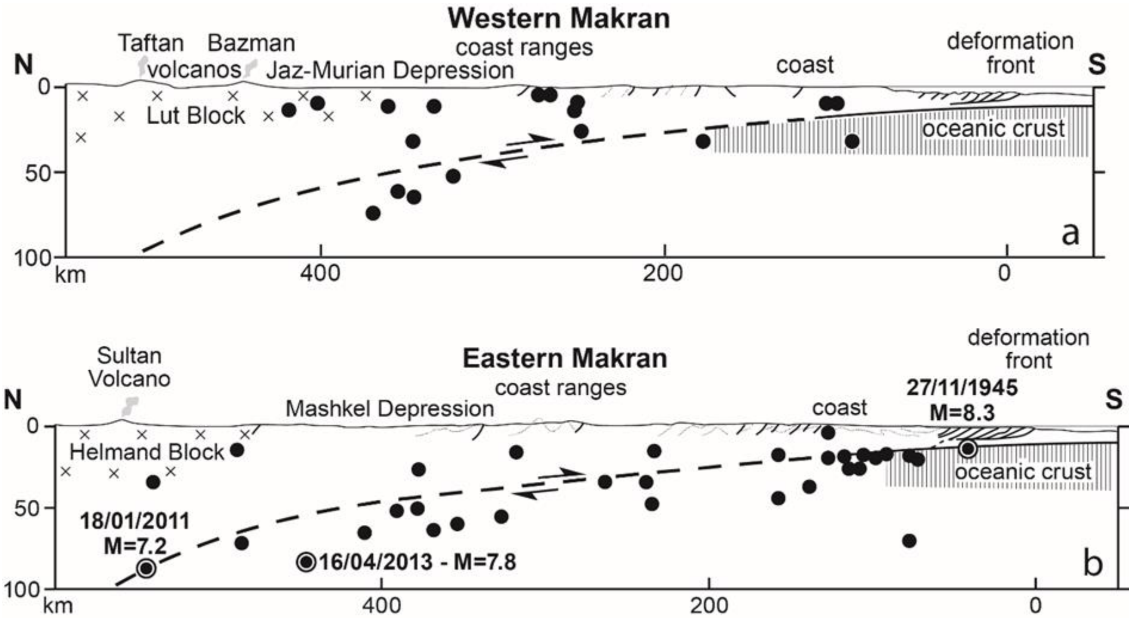

Figure 1.3: Cross-sections across western (a) and eastern (b) Makran with main geologic features and projected focal mechanisms (solid black circles), modified after Byrne et al. (1992) and complemented with magnitude >4 events up to the present by Haghipour and Burg (2014). Location of (a) and (b) in Fig. 1.1. The magnitude 7.2 earthquake of 18, January 2011 and the magnitude 7.8 earthquake of 16 April, 2013, below eastern Makran are normal faulting events within the bending Arabian lithosphere. Oblique crosses indicate continental basement. Catalogue from: http://earthquake.usgs.gov/earthquakes/eqarchives/epic/.

The Makran wedge toe migrates southward at ~ 1 cm/a since the Pleistocene (White, 1982; Platt et al., 1985). To the North of the Jaz Murian and Mashkel basins, three major and active volcanic centres represent the continental magmatic arc of the Makran subduction zone (Farhoudi and Karig, 1977): Bazman (Saadat and Stern, 2011; Pang et al., 2014) and Taftan (Pang et al., 2014) in Iran and Kuh-e-Soltan (Nicholson et al., 2010) in Pakistan (Fig. 1.1). Less work has been done on the onshore Iranian Makran (Jacob and Quittmeyer, 1979; McCall and Kidd, 1982; McCall, 1983; McCall, 1985; McCall et al., 1994; McCall, 1995, 1997, 2002; Hosseini-Barzi and Talbot, 2003; Burg et al., 2008; Dolati, 2010; Hunziker et al., 2010; Haghipour et al., 2012; Burg et al., 2013; Dolati and Burg, 2013; Haghipour, 2013; Ruh, 2013; Ruh et al., 2013; Haghipour and Burg, 2014; Haghipour et al., 2014; Hunziker, 2014; Hunziker et al., 2015) than there are seismic profiles through the offshore Makran (Von Rad et al., 1995; Fruehn et al., 1997; von Rad et al., 1999a; Ellouz-Zimmermann et al., 2007b; Grando and McClay, 2007) and on the Pakistani part of the accretionary wedge (Platt et al., 1985; Platt and Leggett, 1986; Platt et al., 1988; Kopp et al., 2000). This may be explained by the rugged and not easily accessible landscape of the onshore Makran. Nevertheless, the extremely good outcrop conditions and the excellent sedimentary and stratigraphic records make the Makran an excellent field area to study the provenance of sedimentary rocks.

The northwest-southeast trending Sistan Suture Zone (SSZ) of east Iran, which is also referred to as the Eastern Iranian Mountain Range, separates the continental Lut sub-block of Central Iran, to the west, from the Afghan Block, to the east (e.g. Freund, 1970; Şengör, 1990b; Fig.1.1). The Sistan Suture Zone is attributed to the Paleocene (~ 89-55 Ma) closure of a small branch of a relatively short-lived, N-S arm of the Neo-Tethys Ocean along an easterly dipping subduction zone (Berberian and King, 1981; Camp and Griffis, 1982). Subduction beneath the Afghan block is inferred from Late Cretaceous-Paleocene calc-alkaline volcanism (Tirrul et al., 1983; Fig. 1.4).

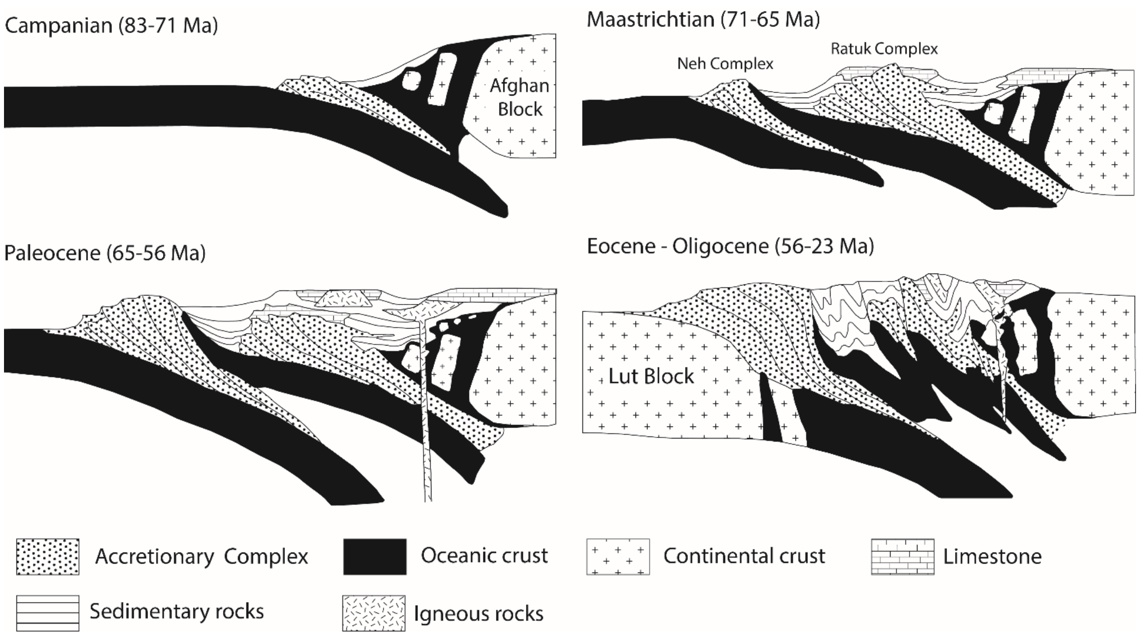

Figure 1.4: tectonic evolution and double subduction model of the North and Middle parts of the Sistan Suture Zone redrawn after figure 10 of Tirrul et al. (1983).

This Cretaceous-Paleogene oceanic basin is documented by ophiolites now exposed in ″Mélange″ zones (Rad et al., 2005). The bulk of the mountain range consists in an accretionary complex (Tirrul et al., 1983). Three phases of deformation were identified (Camp and Griffis, 1982; Tirrul et al., 1983). The oldest folding event produced E-W trending structures, which were subsequently refolded along NNW trending axial surfaces and dissected by conjugate left- and right-lateral strike-slip faults. These two deformation episodes took place between the late Eocene and early Miocene. The third, ongoing deformation event involves N-S right-lateral strike-slip faulting and associated folding and is related to the ongoing collision of Arabia and Eurasia (Berberian and King, 1981). Right-lateral transpression in Sistan accommodates the northward movement of the Lut block with respect to Sistan. The boundary between the Jaz Murian and the Sistan Suture

Zone is the site of intense deformation bringing ophiolitic units to the surface. The cumulative right-lateral displacement is >10 km (Walker and Jackson, 2004).

1.2.2 Makran Accretionary Wedge

On the basis of tectonic and stratigraphy, the onshore Iranian Makran has been divided into four major east-west-oriented units separated by major thrust zones (Fig. 1.5). These units are from north to south, i.e. from the structural top to bottom: (1) North Makran, (2) Inner Makran, (3) Outer Makran and (4) Costal Makran (Dolati, 2010).

North Makran includes: (1) ophiolitic mafic and ultramafic rocks with their upper crustal pillow lavas and Cretaceous deep-marine radiolarites and turbidites; these rocks were eroded and unconformably covered by Upper Cretaceous-Paleocene shallow water sedimentary rocks; (2) the base of North Makran is the Bashakard thrust, which developed tectonic imbrication of ophiolites and intermediate rocks, Upper Cretaceous volcanoclastic sandstones, shales, conglomerates and shallow water limestone and marbles; (3) Small outcrops of Eocene turbidites are unconformable and scattered in the north-central part.

Inner Makran exposes Eocene-Oligocene and locally Miocene rocks between the Bashakard thrust in the north and the Ghasr Ghand Thrust in the south (Fig. 1.5). In between, several thrust sheets are dominated by: (1) Lower Eocene deep marine sedimentary rocks, pillow lavas and associated volcaniclastic sandstones that grade upwards into Middle Eocene deeper marine turbiditic sequences; (2) Lower Oligocene shale-dominated distal (outer fan) turbidites that grade into Upper Oligocene sandstone-dominated inner and outer fan turbidites followed by Uppermost Oligocene shale-dominated slope and delta turbidites. This upward more clastic and proximal evolution suggests progradation of submarine fans followed by the deposition of slope sediments grading into pro-delta turbidites; (3) Lower Miocene sedimentary rocks dominated by marl and calcareous shallow water sandstones passing to Middle Miocene deltaic sandstones and shales. The Lower Miocene pro-delta turbidites are grading upward to shallow shelf, deltaic and tidal sandstones and shales. Miocene synsedimentary deformation is testified by growth structures and the upward shallowing of sedimentary facies (Dolati, 2010; Fig. 1.5).

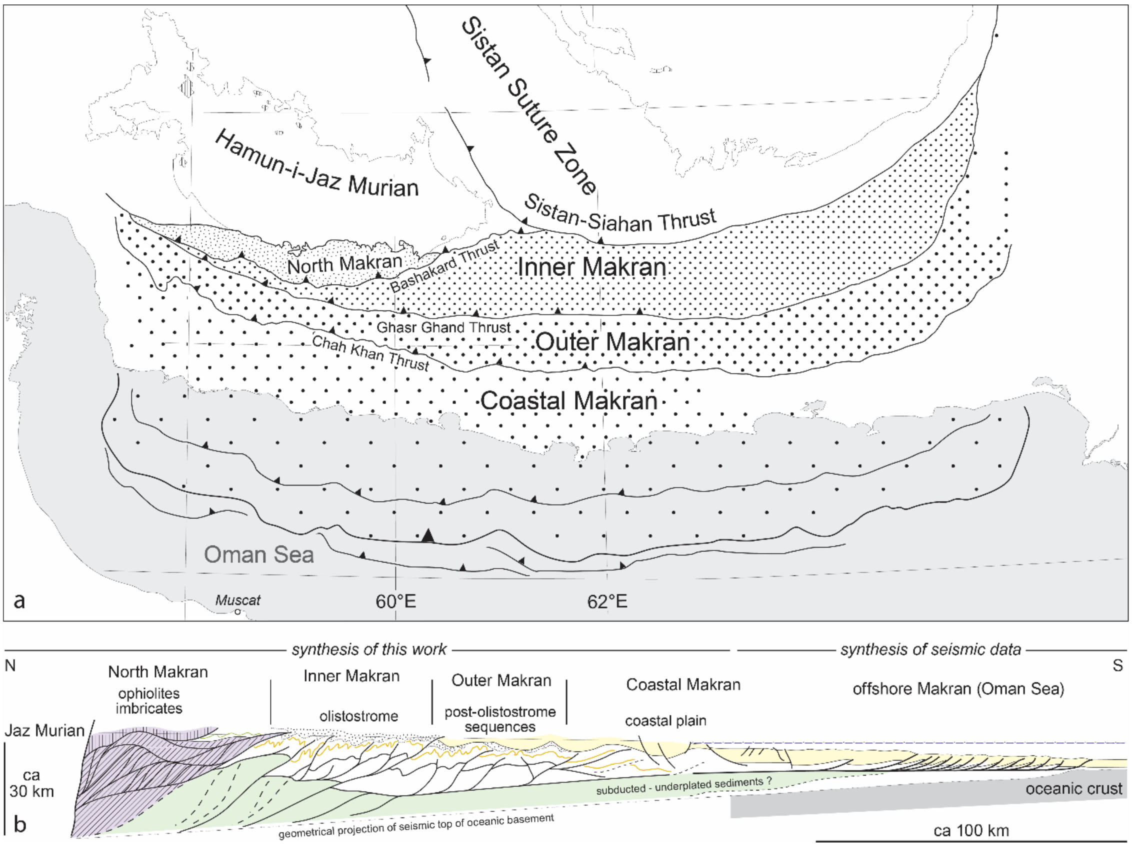

Figure 1.5: a) General tectonic setting and simplified structural map of the Makran accretionary wedge, modified from Haghipour et al. (2014). b) Figure 12.19 from Burg et al. (2013), general, synthetic profile across the Makran accretionary system.

Outer Makran mostly exposes Lower to Middle Miocene sedimentary rocks between the Ghasr Ghand and Chah Khan thrusts. The Lower Miocene is dominated by marls and thick-bedded sandstones that grade laterally into shallow shelf, deltaic and tidal calcareous sandstones, siltstones, marls and coral limestones. The Middle Miocene sandstone and shale dominated deep marine turbidites grade up-section to the shallowing upward deposition to shelf environment.

Coastal Makran, between the Chah Khan thrust in the north and the coast, is covered by Upper Miocene marlstone, channelized calcareous sandstones and polymictic conglomerates with mollusc shells, herringbone structures and mud cracks suggesting a shallow-water depositional environment. Pliocene-Pleistocene shallow-water calcareous sandstones and marls are overlain by Pliocene-Pleistocene thick-layered continental conglomerates. Generally, Coastal Makran preserves a fill-up basin of Pliocene age (Dolati, 2010).

Altogether, Makran as an accretionary wedge started with deep marine deposition and submarine volcanic activity in the Early Cretaceous and became a shelf environment in Pliocene-Pleistocene times (Burg et al., 2013). Estimated thicknesses in the Makran are very great. Sequences of individual turbidite units bounded by major faults have been estimated at 10-14 km thick (McCall, 2003). A gigantic, Early Tortonian mud-and-debris flow covers today an area of ~ 10′000 km^2 with an incomparable landscape (Burg et al., 2008). The olistostrome includes blocks of ophiolites and oceanic sedimentary rocks derived from the ophiolite-bearing, imbricate thrust zone of North Makran, and reworked chunks of the turbidites on which it rests with an erosional unconformity. In the Iranian Makran, the Cenozoic turbidite is late Paleocene through early Miocene in age and the structures provide no evidence at all that the Eocene, Oligocene and early Miocene turbidite sequences have been significantly disturbed by folding or faulting prior to the Miocene early Pliocene shallow sediment deposition. The intense folding, faulting and dislocation, involving reverse faults and a duplex structure, which characterizes the Cenozoic of the Makran (and indeed affects the Mesozoic rocks also), appears to relate to an intense and widespread culminating episode in the late Miocene-early Pliocene. An episode accompanied by a jump of the subduction front to its present position offshore and which was followed by uplift and the deposition of immense, scattered molassic continental fanglomerates of Pliocene-Pleistocene age in front of the uplifted, folded rocks (McCall, 2003).

Towards the North, the imbricate and mélange zone of North Makran is bordered by the desertic Jaz Murian (Iran) and Mashkel (Pakistan) depressions (Figs 1.1; 1.5), which are interpreted as forearc basins (e.g. McCall, 1997). These two depressions are geographically separated by the NNW-SSE striking Sistan suture Zone (Fig. 1.1; Tirrul et al., 1983).

The offshore Makran Accretionary Wedge has been intensely investigated by seismic profiling (Ellouz-Zimmermann et al., 2007a; Ellouz-Zimmermann et al., 2007b; Grando and McClay, 2007; Bourget et al., 2010; Bourget et al., 2011; Bourget et al., 2013; Fig. 1.6). The Upper Oligocene and Miocene sedimentary rocks are detached over one or more décollement layers formed by water-saturated and shale-rich sediments within turbidites. The northern part of the offshore Makran consists of a shelf and a flat slope with high accumulation rates leading to normal faulting seen in coastal Makran (Bourget et al., 2010).

Nearly E-W striking normal faults cut sedimentary rocks younger than Upper Miocene in the Coastal Makran (Fig 1.7). They formed during regional extension, which is also responsible for sediment-filled fissures (Dolati, 2010) and normal faults in the Pakistani Makran (e.g. Harms et al., 1984). These normal faults are likely analogous to the listric normal faults cutting Pliocene-Pleistocene shelf sequences in offshore seismic sections (e.g. Harms et al., 1984; Platt et al., 1985; Grando and McClay, 2007; Fig. 1.6). They formed in a crustal regime while convergence effects are deep-seated, perhaps close to the subducting slab (Jacob and Quittmeyer, 1979; Byrne et al., 1992; Engdahl et al., 2006). Study of syndeformational sediments (growth strata) in the Makran shoreline shows episodes of deposition during subsidence, as a result of obliqueslip normal faulting, alternating with episodes of erosion during uplift, driven by oblique-slip thrusting

(Hosseini-Barzi and Talbot, 2003). The geometry of the growth strata preserved in the limbs of the fault propagation folds in the outer part of the Makran accretionary prism reveals limb rotation as the main folding mechanism with uplift rate of the growing folds exceeding the sedimentation rate suggesting active thrusting at the wedge front. The growth strata patterns also indicate a synchronous activity of many of the thrusts of the imbricate fan system that exhibit a sequence of thrusting propagating toward the foreland (Grando and McClay, 2007). The contact between the Jaz Murian depression and the Makran accretionary wedge also shows important NW-SE to N-S dipping normal faults (Dolati and Burg, 2013). The southern part of the offshore Makran is a typical, active fan.

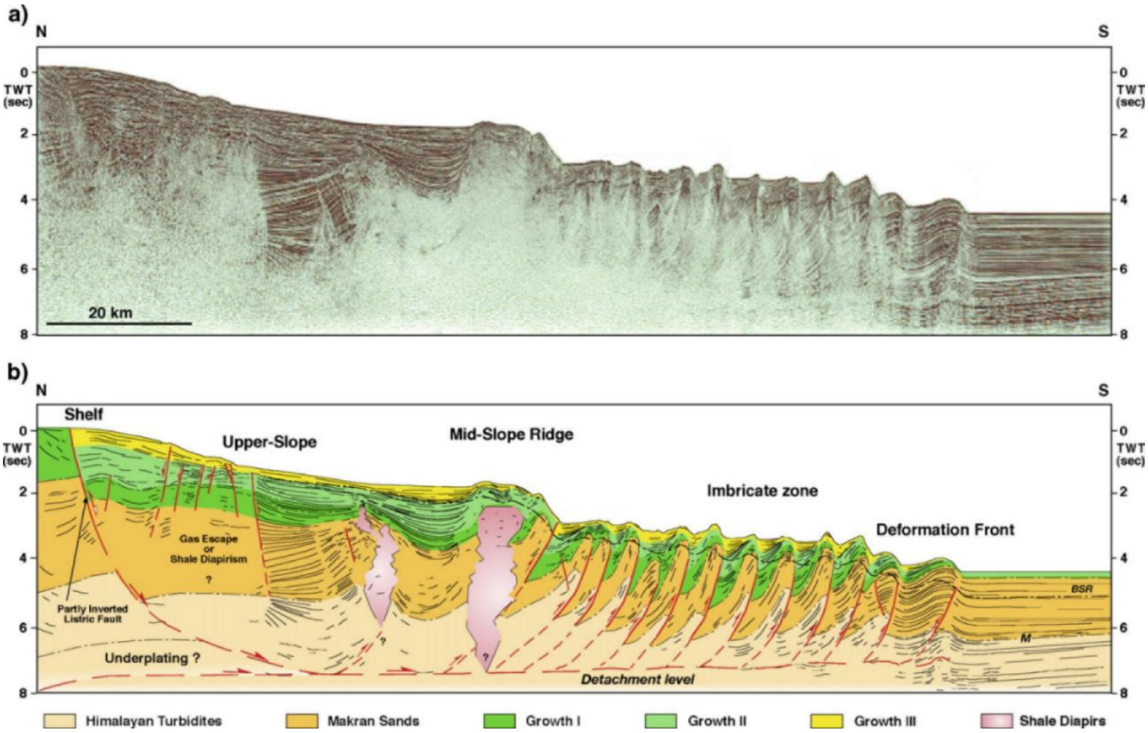

Figure 1.6: (a) N-S seismic profile across the western sector of the offshore Makran accretionary prism. (b) Interpretation of seismic line in (a). Note the normal faults in the shelf and upper slope domain with a major, south dipping listric normal fault and a related roll-over anticline. Diapirs of over pressured shales are associated with thrusting in the mid-slope domain. The lower slope consists of thrust fault-related imbricate fans. Vertical exaggeration at the sea floor is approximately 6:1. Figure 5 of Grando and McClay (2007).

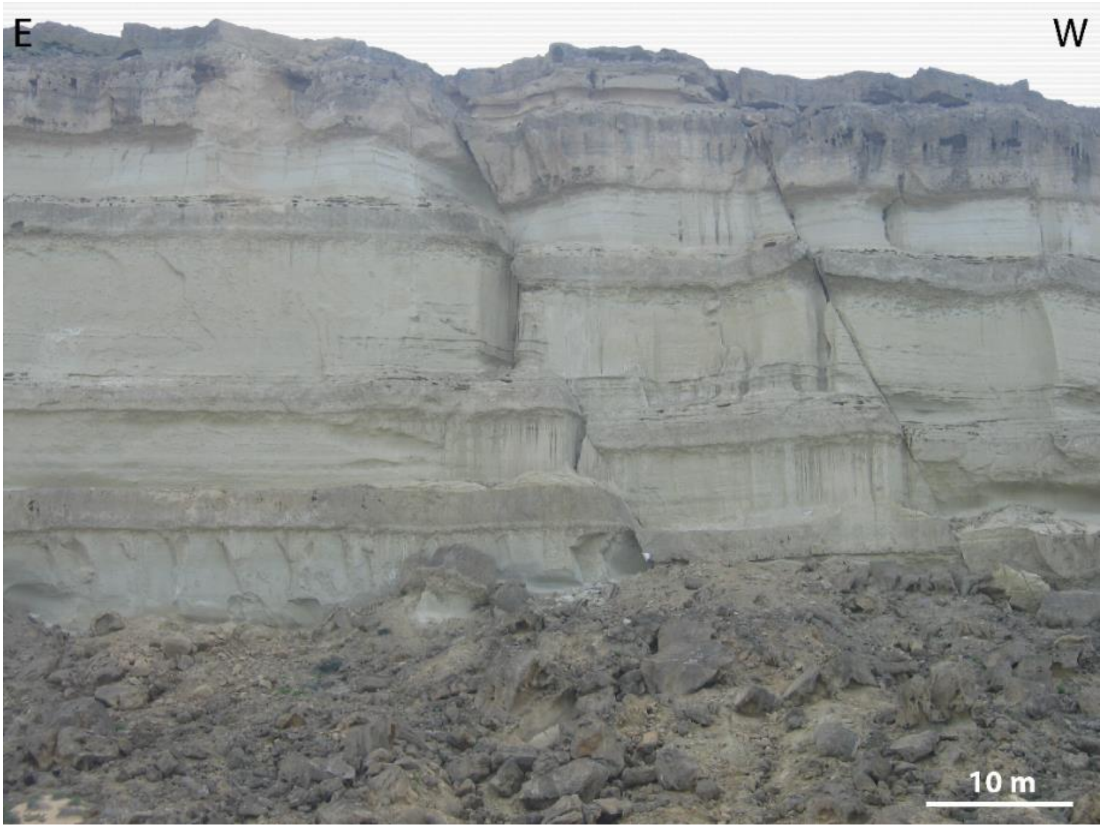

Figure 1.7: Planar normal faults in the coastal Makran at 25º21´11.34″N/60º18´10.44″E.

1.2.3 Sistan Suture Zone

The Sistan Accretionary Wedge is subdivided into three northwest-trending: the Ratuk Backstop Complex to the east, the Sefidabeh Forearc Basin in the middle and the Neh Accretionary Complex to the west (Camp and Griffis, 1982; Tirrul et al., 1983; Fig. 1.8). Southern part of the Sistan basin as an accretionary wedge started with deep marine turbiditic deposition in Eocene and became a shelf environment in Oligocene-Miocene. Folding and thrusting of Eocene-Oligocene turbidites mark the closure of the basin (Bröcker et al., 2013). Collision of the Lut Block with the subduction complex in Mid-Eocene times (Camp and Griffis, 1982) produced widespread deformation and intrusion of the Eocene and Oligocene, Zahedan-Shah Kuh magmatic belt (Berberian and Berberian, 1981). Collision of the Sistan basin is not related to the India-Asia collision. The present southwest vergence of the accretionary prism basins indicated by consistent facing of ophiolites, metamorphic and shear foliation, and fold asymmetry (Tirrul et al., 1983). A regional system of folds and transcurrent faults testifies continued E-NE compression (Walker and Jackson, 2004). These structures are buried below mildly deformed Miocene volcanic rocks. Miocene calc-alkaline activity was limited to sporadic volcanism in the north and minor felsic and intermediate intrusions farther south (Tirrul et al., 1983). These units are largely undeformed and not related to major faults (Camp and Griffis, 1982). The youngest magmatic event is recorded by late Miocene-Pliocene mafic flows that are weakly alkaline and related to dextral faults (Tirrul et al., 1983). The subdivision of the Sistan accretionary wedge into the Neh Accretionary Complex, Ratuk Backstop Complexe and Sefidabeh Forearc Basin may prove to be arbitrary for the continuation of the belt to the northwest (Fig 1.8).

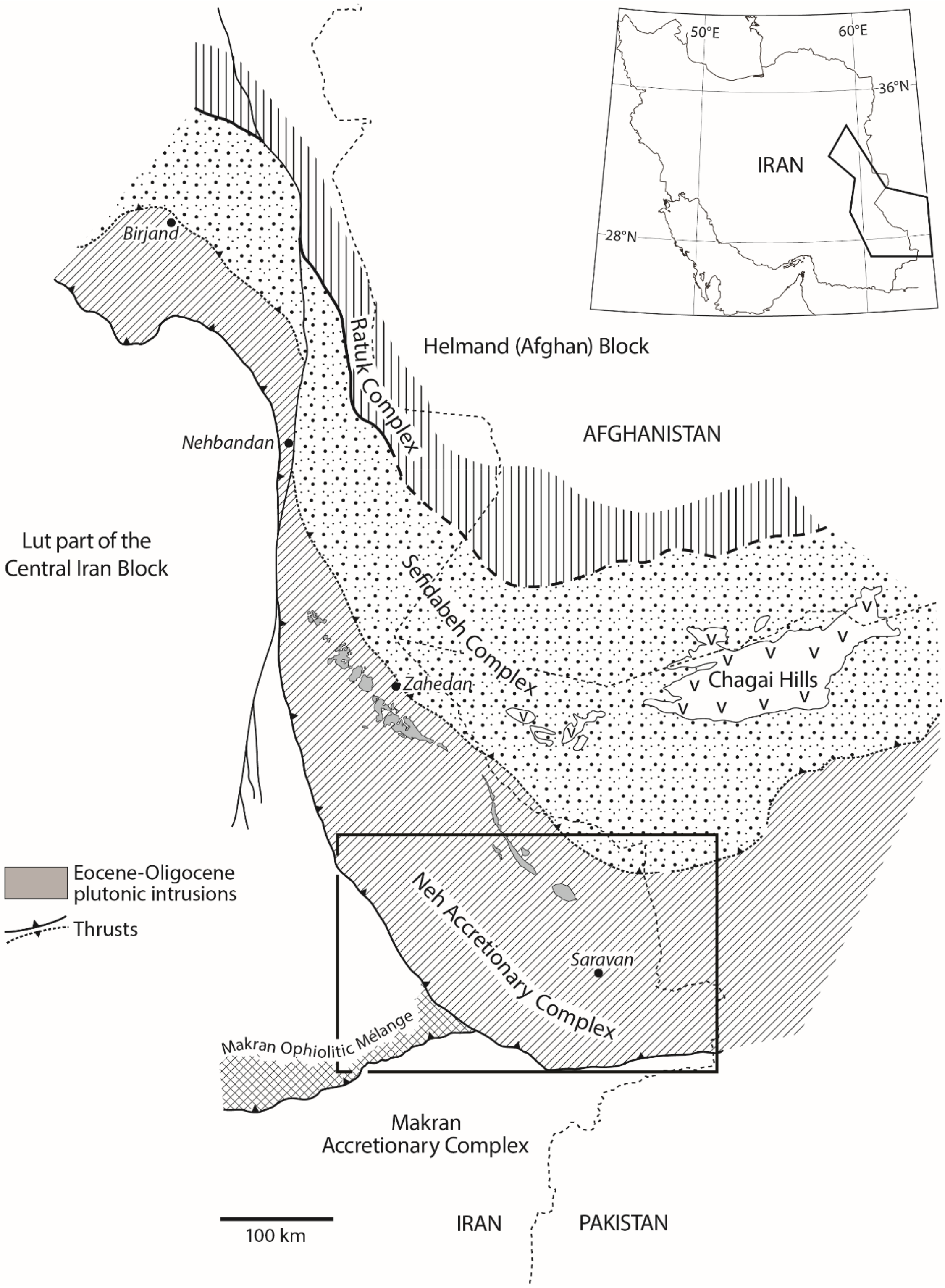

Figure 1.8: Sistan Basin including Neh Accretionary Complex, Rahtuk Backstop Complex and Sefidabeh Forearc Complex between Lut Iran Block and Afghan Block.

1.2.3.1 Neh Accretionary Complex

The Neh Complex consists of ophiolitic mélanges, Upper Cretaceous shallow water limestone, Eocene-Oligocene deep marine turbidities and their very low grade metamorphic equivalents. Eocene-Oligocene turbidites are deformed and disrupted by thrust faults and make up large parts of the Neh Complex (Tirrul et al., 1980; Tirrul et al., 1983). These turbiditic sequences are typically several hundred meters thick and dominated by Bouma-type sandstone and shale sequences (e.g. Samimi Namin et al., 1994). Eocene and Oligocene calc-alkaline plutons (Sadeghian et al., 2005) intrude the meta-sedimentary rocks in a NW-SE trending belt, parallel to the Sistan Suture Zone (McCall, 1997). The main lithologies of the largest plutons are granite-granodiorite-quartz monzonite (Camp and Griffis, 1982). Some authors (e.g. McCall, 2002; Carter et al., 2010) interpret the southern Neh Complex as a transitional zone between the Sistan and Makran basins.

1.2.3.2 Ratuk backstop Complex

The Ratuk Complex, formed before the Maastrichtian, is the oldest part of the suture zone. It comprises Cretaceous ophiolitic mélanges, metamorphic rocks including eclogites, blueschists and epidote amphibolites and sedimentary rocks including lower Cretaceous limestone, upper Cretaceous turbiditic sandstones, Eocene nummulitic limestones and Neogene conglomerates (e.g. Tirrul et al., 1983; Bröcker et al., 2013; Delavari et al., 2014). Ophiolite components (peridotite, serpentinite, orthopyroxenite, gabbro, norite, plagiogranite, basalt, radiolarite) constitute about 30% of the Ratuk complex (Zarrinkoub et al., 2012; Bröcker et al., 2013). Rb-Sr, ^{40}Ar-^{39}Ar and U-Pb ages of the blueschist, epidote amphibolites and eclogite provided 85-87 Ma (Rad et al., 2009; Bröcker et al., 2013). These regionally consistent ages document Late Cretaceous metamorphic processes in the geodynamic evolution of the Sistan Basin

1.2.3.3 Sefidabeh Forearc Basin

The Sefidabeh Forearc Complex between the Neh Complex, in the west, and the Ratuk Complex, in the east, unconformably covers both the Neh and Ratuk Complexes (Babazadeh and De Wever, 2004). This basin is interpreted as a forearc because of its location, sedimentological character and age (Tirrul et al., 1983). It comprises an 8 km thick, essentially clastic sequence of Cenomanian to Eocene sedimentary rocks including both deep and shallow marine limestones and calc-alkaline volcanic intercalations on its eastern side (Tirrul et al., 1983). Olistostromes with ophiolitic clasts are present (Camp and Griffis, 1982). In the Sefidabeh basin, Upper Eocene deep marine sedimentary rocks pass transitionally upward into red bed continental sedimentary rocks, which indicates shallowing upward of the basin (Camp and Griffis, 1982). Late Eocene regional deformation of the Sefidabeh basin is reported by Freund (1970). The Sefidabeh basin was closed by the Late Eocene as the Lut and Afghan blocks became sutured by continental collision (Camp and Griffis, 1982). The configuration of Tethys in the Mesozoic and Early Cenozoic involves a continental sliver extending from the Sanandaj-Sirjan/Bajgan-Durkan complexes and tapering to the Upper Cretaceous shelf limestone of Kuh-e-Birk near the Pakistan frontier. This continental sliver stretched between two oceans, the inner ocean to the north and the outer ocean to the south (McCall, 1995). The inner and outer oceans are likely to have merged in the southern part of the Sistan Ocean (our study area). The south Sistan Basin deposited in the Sistan Ocean and extends in the Eocene - Lower Oligocene deep marine turbidites of the Pakistan Makran. This basin closed after the Early Oligocene and before the shallow water Upper Oligocene sedimentary rocks (McCall, 1997).

1.3 Methods

We applied provenance analysis on Upper Cretaceous to Miocene turbiditic sandstone samples from the onshore Iranian Makran accretionary wedge and Eocene to Oligocene sandstone samples from the south Sistan Basin. Since there is no Cretaceous sandstone in the south Sistan Basin, there is no analysis for this period.

1.3.1 Paleocurrent analysis

Paleocurrent indicators are oriented sedimentary structures left by ancient currents (Hoffman, 1969). Paleocurrent direction is a common tool of provenance analysis. Paleocurrent orientations were determined from flute casts (90% of all paleocurrent measurements) and asymmetric ripple marks (10%) on turbiditic sandstones. In Flute cast measuring the long axis gives the direction of flow, with the tapered end pointing toward the flow and the steep end up current. The concavity of the flute cast also point stratigraphically up (Figs. 1.9a, b, c). The short and steeper side of asymmetric ripple marks faces the current direction (Figs. 1.9d, e). Current direction in scour marks is defined like for flute casts (Fig. 1.9f). Palaeocurrents are based on less deformed rocks, or where the fold hinge lines were horizontal. Readings of paleo-current directions were rotated to horizontal around the local strike direction of bedding (Gastaldo, 2004) and plotted in rose diagrams. Onshore Makran sandstones and south Sistan Basin (Neh Accretionary Complex) sandstones were analysed separately.

1.3.2 Sandstone framework analysis

Diverse tectonic settings have specific detrital modes and sediment-dispersal patterns (Dickinson and Suczek, 1979). Modal framework grain analysis of the studied sandstones was performed with the Gazzi-Dickinson method on thin sections stained for carbonates and feldspars (Dickinson, 1970; Norman, 1974). At least 300 representative points in each thin section were used to perform a statistically reliable grain analysis. We furthermore applied the Zuffa method (Zuffa, 1985) to count lithic fragments. Minerals larger than 0.063 mm within rock fragments were counted as monomineralic grains. Results are converted to percentages for compositional comparisons (Weltje and von Eynatten, 2004). Typically, only framework (non-matrix) grains are counted. We employed five standard complementary triangular diagrams (QFL, QmFLt, LvhLsLm, QmPK and QpLvLsm to classification of the sandstones (Folk, 1968) and to interpret the geodynamic setting of the source terranes (Dickinson and Valloni, 1980).

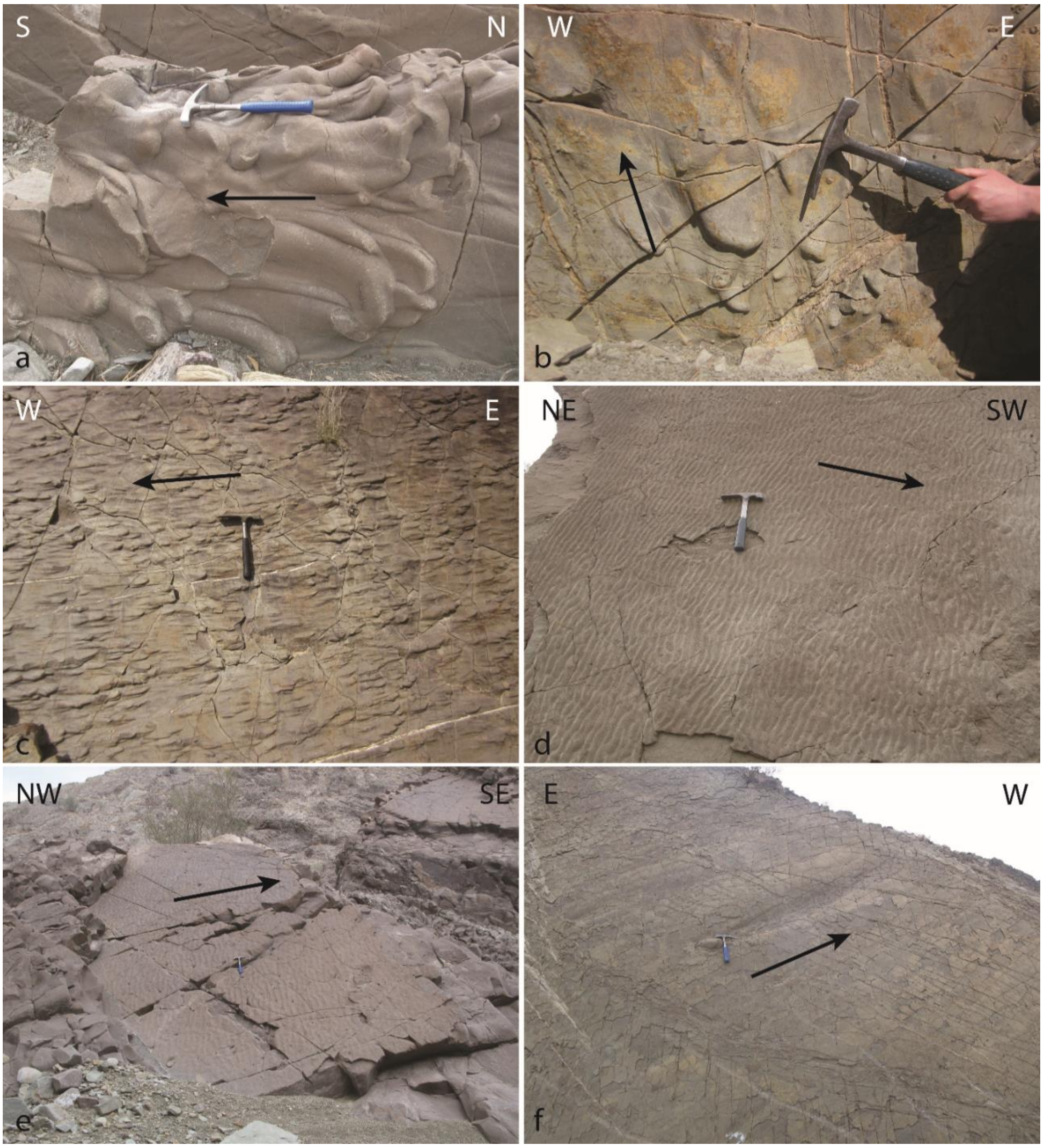

Figure 1.9: a) Flute cast in Eocene sandstone of the Inner Makran at 26°29′08.3″N/59°59′08.6″E; b and c) flute cast in Eocene sandstone of the South Sistan Basin at 27°47′37.6″N/61°57′41.1″E and 26°47′04.8″N/62°33′35.0″E respectively; d) asymmetric ripple mark in Miocene sandstone of the Outer Makran at 26°02′09.8″N/59°40′09.6″E; e) asymmetric ripple mark in Oligocene sandstone of the Inner Makran at 26°15′32.0″N/59°56′52.1″E; f) scour marks in Eocene sandstones of the Inner Makran at 26°19′00.9″N/60°22′45.8″E. Arrow are paleocurrent direction.

1.3.3 Heavy minerals study

Heavy mineral assemblages are sensitive and widely-used tracers in the determination of sediment provenance (Morton and Hallsworth, 1999; Mange and Wright, 2007; Hallsworth and Chisholm, 2008). For heavy mineral studies, sample preparation and separation followed the standard techniques (Smale, 1990; Mange and Maurer, 1992). To obtain the transparent heavy mineral fractions (density ≥ 2.9 g/cm^3 and typically <1% of bulk rock), the sandstones were crushed by SelFrag apparatus batch equipment using high voltage (130-150 KV) pulse power technology to liberate morphologically intact minerals. From the < 2 mm sieved fraction the carbonate was dissolved in warm (60 - 70°C) 10% acetic acid. The heavy minerals were extracted in separation funnels from the 0.063-0.4 mm sieve fraction (Mange and Maurer, 1992) using bromoform (density 2.88 g/cm^3). The bulk heavy mineral fractions were mounted in piperines between a glass slab and cover (Martens, 1932). Mineral identification and quantification were carried out under a petrographic microscope using the mid-point ribbon and fleet counting methods (Mange and Maurer, 1992). At least 200 grains were counted per sample.

1.3.4 Cathodoluminescence (CL) and Back Scattered Electron (Jacobsen and Wasserburg) imaging

The external morphology and internal zoning patterns of zircons have paragenetic and petrogenetic significance (Poldervaart and Eckelmann, 1955). In zircons, Dy^{3+} is considered to be the principal spectral factor (Remond, 1977; Mariano, 1989), though other constituents such as Sm^{3+}, Eu^{2+}, Tb^{3+} and Y^{3+} may be CL emitters (Yang et al., 1992). The main use of CL zircon imaging has been an adjunct to U-Pb dating by identifying the different types of zircon domains that can be dated in situ. Determining the age of different domains within crystals helps understanding the various geological processes (magmatism, metamorphism, hydrothermal alteration) recorded during the multi-stage history of the grain (Rubatto and Gebauer, 2000). BSE techniques were employed to investigate surface morphology of the zircons, crystal shape and also inclusions of other minerals in zircons. The CL and BSE images for all individual detrital and magmatic zircon grains were taken from a split screen on a CamScan CS44 scanning electron microscope (SEM; Tescan a.s., Brno, Czech Republic) at the ETH- Zurich.

1.3.5 Laser ablation ICP-MS

1.3.5.1 Zircon geochronology (U-Pb system)

Zircon geochronology has developed rapidly during the past two decades, following the technical advances that enable determining U-Pb ages from individual crystals (Thirlwall and Walder, 1995; Woodhead et al., 2004; Hawkesworth and Kemp, 2006; Kemp et al., 2006; Zeh et al., 2007). The U-Th-Pb system is a very powerful tool for geochronology due to three different decay systems: ^{238}U-^{206}Pb (half-life of 4.47 Ga), ^{235}U-^{207}Pb (half-life of 0.70 Ga), and ^{232}Th-^{208}Pb (half-life of 14.01 Ga). These three decay systems yield chronometers that are based on the measurement of $^{206}Pb/^{238}U$, $^{207}Pb/^{235}U$, and $^{208}Pb/^{232}Th$ respectively (Jaffey et al., 1971). In practice, for zircon, the measured critical isotopes include $^{206}Pb/^{238}U$, $^{206}Pb/^{207}Pb$, and $^{206}Pb/^{204}Pb$. $^{208}Pb/^{232}Th$ is generally not used because of the lower Th concentration in zircon and the possibility that the Pb/Th system is decoupled from the Pb/U system. $^{207}Pb/^{235}U$ is not measured because it can be calculated more reliably from $^{206}Pb/^{238}U$, $^{206}Pb/^{207}Pb$, and $^{238}U/^{235}U$ ratios. $(^{207}Pb/^{235}U) = (^{206}Pb/^{238}U)/(^{206}Pb/^{207}Pb)\times137.82$. $^{206}Pb/^{204}Pb$ is commonly measured so that $^{206}Pb/^{238}U$ and $^{206}Pb/^{207}Pb$ can be corrected for Pb incorporated at the time of crystallization. Analyses utilizing standard-sample bracketing are also conducted by laser ablation inductively coupled plasma mass spectrometry (LA-ICP-MS), which uses a laser beam to excavate material from a polished sample surface and then conducts isotope analyses with a mass spectrometry (Fryer et al., 1993; Košler et al., 2002). This method also yields ages with a precision and accuracy of 1-2%, but it has a more rapid analysis.

Provenance analysis and reconstructing tectonic setting are the most common applications of detrital zircon U-Pb geochronology (Gehrels, 2014). Detrital and magmatic zircons were extracted from sandstone and granitoids samples (ca. 2 kg) using standard mineral separation techniques, including SelFrag high voltage fragmentation, dissolution of carbonate cement in cold hydrochloric acid (only for sandstone samples) and heavy liquid (methylene iodide, density 3.32 g/cm^3) separation. Handpicked zircons in three different sizes (fine, medium and coarse) were mounted in epoxy blocks and polished down to expose their core and coated by carbon (~ 30 µm). For provenance analyses on sandstones (detrital zircon U-Pb dating) by LA-ICP-MS, only magmatic domains were investigated, and we did not date inherited cores, while for granites geochronology both inherited cores and also magmatic domains of zircons were dated. All analyzed zircons were controlled and photographed by CL and BSE imaging to determine the internal structures and inclusions of the grains prior to isotopic analysis.

Laser ablation ICP-MS analyses were performed on an Elan 6100 DRC instrument coupled to an in-house- built 193 nm Excimer laser at the ETH Zurich. Helium gas (1.1 l/min) was used as the carrier gas in the ablation cell. The laser was run at pulse rate of 10 Hz with energy of 0.5 mJ/pulse and a spot size of 30 µm. The accuracy and reproducibility within each run of analysis were monitored by periodic measurements of the GJ-1 external standard, with $^{207}Pb/^{206}Pb$ age of 608.5 ± 0.4 Ma (Jackson et al., 2004). Data reduction was performed using the GLITTER software to calculate the relevant isotopic ratios, ages and errors (Van Achterbergh et al., 2001). Concordia and frequency probability diagrams were performed using ISOPLOT v.3.0

(Ludwig, 2003). A Concordant age is given by the overlapping of the error ellipse with the Concordia age curve. In this study, only concordant ages are considered for Hf isotope analysis. The frequency U-Pb age distribution diagram or probability density plot described by Ludwig (2003) includes a histogram representing the number of individual zircons grains within a short age range and the probability curve depicts the mean age peaks of the contained age populations in one sample.

1.3.5.2 Hf isotopes

In addition to its advantage for U-Pb dating, zircon provides high-quality Hf isotope record that reflect the protolith origin (Kemp et al., 2005). Hafnium is an especially important minor element in zircon since its isotopic composition is a sensitive detector of crustal and mantle processes (Vervoort et al., 1999). The significance of the Hf isotopes method in zircon grains, when associated with the U-Pb age method, enables characterizing the isotopic composition of the magma from which the zircons formed. Therefore, the Hf isotopes yield isotopic constrains on the source of detrital zircons and accordingly of the host sandstones. The Lu-Hf isotope system can be utilized to track the history of chemical differentiation of the silicate Earth (crust and mantle) by virtue of the fact that fractionation of Lu from Hf occurs during magma generation (Fig. 1.10; Kinny and Maas, 2003). The $^{176}Lu/^{177}Hf$ ratio of zircon is usually < 0.0005, which means that time-integrated changes to the $^{176}Hf/^{177}Hf$ ratio as a result of in situ decay of ^{176}Lu proceed at virtually negligible rates. Hence, zircon effectively preserves the initial $^{176}Hf/^{177}Hf$ ratio, providing an enduring record of the Hf isotopic composition of their source environment at the time of crystallization (Kinny and Maas, 2003). The Hf isotope ratios can be related to the crustal residence age or the average time elapsed since the source of the magmas from which the zircons crystallized were extracted from a mantle reservoir (Hawkesworth and Kemp, 2006).

The analysis of hafnium isotope ratios was performed on dated zircon grains with concordant U-Pb ages on a Nu plasma MC-ICP-MS (Nu instrument Ltd) attached to a 193 nm UV ArF excimer laser, at the Institute of Geochemistry and Petrology, ETH Zurich. Laser repetition rate of 5 Hz, spot size of 60 µm and He transporter gas (0.8-1.11 l/min) were applied. The energy density used, was 10-20 J cm^{22} and Standard Mud Tank zircon was used for external correction. Each ablation was preceded by a 40 second background measurement, and ablated zircon was measured within 60 s. For the accurate measurement of Hf isotope ratios in zircon, the isobaric interference of ^{176}Yb and ^{176}Lu on ^{176}Hf were corrected by measuring ^{171}Yb ($^{176}Yb/^{171}Yb$ = 0.897145) and ^{175}Lu ($^{176}Lu/^{175}Lu$ = 0.026549), respectively. Age correction to calculate initial $^{176}Hf/^{177}Hf$ ratios were obtained using a ^{176}Lu decay constant of 1.867×10^{-11} $year^{-1}$. The estimate of $\varepsilon\text{-}Hf_{(t)}$ (time-corrected) values was based on zircon U-Pb ages and the chondritic values ($^{176}Hf/^{177}Hf$ = 0.282772, $^{176}Lu/^{177}Hf$ = 0.0332; (Blichert-Toft and Albarède, 1997).

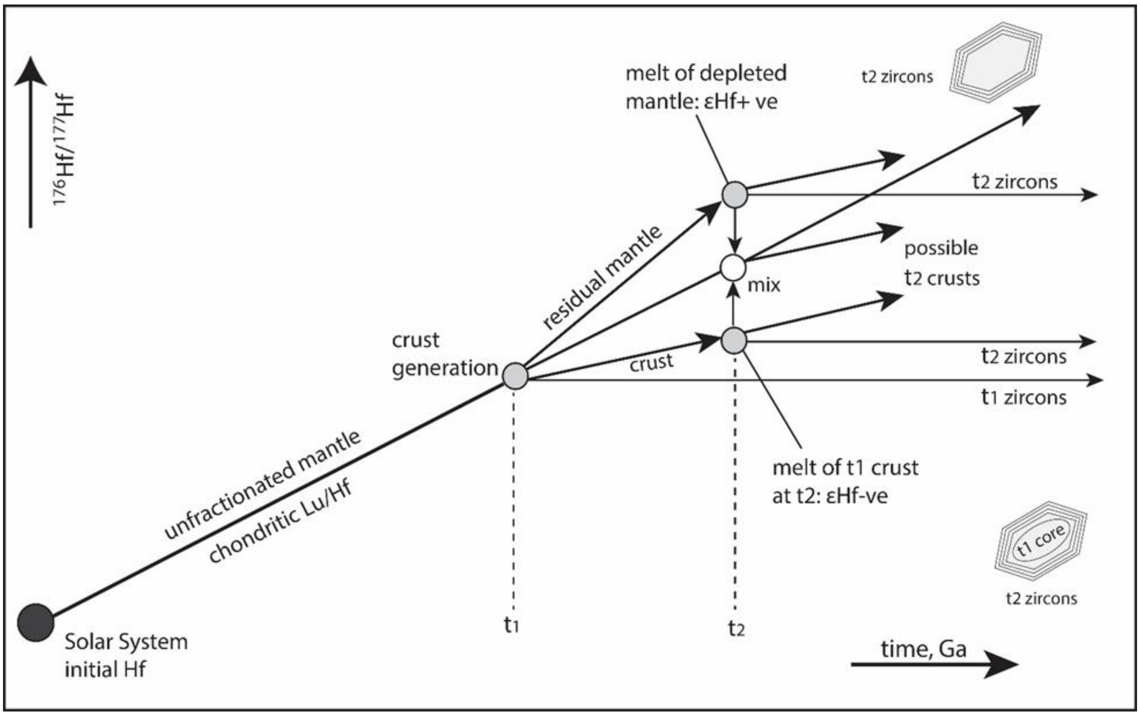

Figure 1.10: Schematic Hf isotope evolution diagram, modified after Patchett and Tatsumoto (1981), showing how an episode of partial melting in Earth's Mantle at time t1 results in divergent Hf isotope evolution paths for the newly generated crust (low Lu/Hf) and the residual mantle (high Lu/Hf). Having extremely low Lu/Hf, any zircons formed within that crust will preserve its initial $^{176}Hf/^{177}Hf$ ratio, and hence over time diverge in composition from the remainder of the host rock. At time t2 a variety of possible sources may contribute to newly formed crust. If wholly derived from depleted mantle, the initial ε-Hf will be positive, however mixing with an undepleted or enriched source, for example by crustal contamination, may result in low positive, zero, or negative ε-Hf at the time of crystallization depending on the balance of components. Any inherited zircon core at t2 would be expected to have lower ε-Hf than the newly crystallized host rock.

1.3.5.3 Trace elements

Trace elements were measured at ETH Zurich with Laser Ablation-Inductively Coupled Plasma-Mass Spectrometry (LA-ICP-MS) on XRF fused discs calibrated without matrix-matching standards (Günther, 2002). The spectrometer was set up for 27 trace elements (Cs, Rb, Ba, Th, U, Nb, Ta, La, Ce, Pb, Pr, Sr, Nd, Sm, Zr, Hf, Eu, Gd, Tb, Dy, Y, Ho, Er, Ti, Tm, Yb, Lu). Data acquisition time per spot was about 1 minute and energy density was 15 J/cm^2 at a frequency of 12 Hz. For each disc we analysed three spots (90 µm diameter). Concentration of CaO were obtained by XRF analysis were used as internal standards and calibrated against NIST 610 for data correction with SILLS program (Guillong et al., 2008). The expected measuring error is ~1%, close to the detection limit, and even smaller at higher concentrations. Trace elements analysis were done for bulk sample of magmatic rocks to determine rock types and identify the origin of the magmas and tectonic environment of the Zahedan and Shah Kuh magmatic rocks.

1.3.6 X-Ray Fluorescence (XRF)

Whole-rock X-Ray Fluorescence (XRF) analyses were performed on fused discs using a Panalytical Axios wave-length dispersive spectrometer (WDXRF, 2.4 KV) at ETH Zurich.

Samples were grinded to fine powder in an agate mill and mixed with lithium tetraborate at 1:5 ratio and molten to homogenous glass discs. The spectrometer is set up for 12 major and minor elements (SiO_2, TiO_2, Fe_2O_3, MnO, MgO, CaO, Na_2O, K_2O, P_2O_3, Cr_2O_3, NiO) and 19 trace elements (Rb, Ba, Sr, Nb, Zr, Hf, Y, Ga, Zn, Cu, Co, V, Sc, La, Ce, Nd, Pb, Th, U).

1.3.7 Thermal Ionization Mass Spectrometry (TIMS)

1.3.7.1 Rb-Sr and Sm-Nd isotopes

Rb-Sr and Sm-Nd isotopes ratio are important tools to provide information on the source of igneous melts as well as to provide age data (McCulloch and Wasse, 1978; Vervoort and Blichert-Toft, 1999). Rb, Sr, Sm and Nd isotopic compositions were determined on thermal ionization mass spectrometry (TIMS) on the Triton Plus Thermo Fisher Scientific at ETH Zurich. All whole-rock powders were prepared by grinding in an agate mill. 50 mg of each powder were dissolved in closed savillex vials up to 8 ml of 4:1 concentrated HF-HNO_3 mixture at 160˚C on hotplate in 17 ml Teflon beakers over 5 days. After digestion, a few drops of perchloric acid were added to each sample, which, after drying down, were completely dissolved in 6M HCl. For the chemical separation of Rb, Sr, Sm and Nd, three ion exchange columns filled with BioRad AG50W-X8 (H^+) cation resin (200-400 mesh). The matrix elements as well, Rb and Sr were sequentially washed off the column in 2.5M HCl. After drying down, the Rb and Sr cuts were re-dissolved in 3M HNO_3 and loaded onto pre-cleaned ion exchange columns filled with Eichrom Sr spec resin. Rubidium was washed off this column in 3M HNO_3, while Sr was eluted with 0.05M HNO_3. Only Eichrom Sr spec resin was used for the chemical separation of Sr from the spiked aliquot (Hans, 2013). High precision Sr isotope measurements were performed with Triton Plus. All runs were normalized to $^{86}Sr/^{88}Sr$ = 0.1194 and measured with ~20 V on ^{88}Sr. For each run, 600 ratios were obtained, resulting in within-run precisions of ± 2-4 ppm for $^{87}Sr/^{86}Sr$. The NBS987 standard was measured at $^{87}Sr/^{86}Sr$=0.710252 ± 0.0000027 (2σ SD). JNdi-1 was measured at $^{143}Nd/^{144}Nd$ = 0.512099 ± 0.000006 (2σ SD), (Aciego Pietri and Brookes, 2009). The average precision of our measurements is ± 4 ppm (2σ SD). Rb isotope dilution measurements were performed on a Nu Plasma MC-ICPMS at ETH Zurich using admixed Zr for mass bias correction.

1.4 Outline of the thesis

This thesis is comprised of five chapters. Chapters II, III and IV represent manuscripts submitted for publication.

Chapter II presents combined field work data, modal framework grain composition of the Upper Cretaceous to Miocene sandstone and heavy mineral analysis of the onshore Makran Accretionary Wedge. Detrital zircon single grain (CL and BSE imaging, ICP-MS laser ablation U-Pb ages) are used to evaluate crystallization ages in the source area. Hf isotope ratios of dated detrital zircons are used to infer the origin of the magmas in the source region. We obtained protolith ages from Middle Jurassic to Eocene (167-48.4 Ma). The protolith rocks belonged to a Mid-Jurassic intracontinental rift and a Late Cretaceous-Eocene continental arc. Ophiolite and blueschists were additional, minor sediment sources. Results refute opinions that the Makran detritus were supplied from Himalayan sources by a Palaeo-Indus submarine fan delta complex. Instead, the Upper Cretaceous-Oligocene erosional scree was transported by two rivers and subsequent turbiditic flows in submarine fans from a nearby complex of continental arc and ophiolites to the north. Miocene detritus recycle Eocene-Oligocene sandstones of onshore Makran.

Chapter III presents the provenance analysis of Eocene and Oligocene turbiditic sandstones of the south Sistan Basin following similar approaches as for the Makran basin. Protolith ages span from Late Cretaceous to Eocene (115-49.5 Ma). The protolith rocks belonged to a Late Cretaceous intra-oceanic island arc transformed into Eocene transitional-continental arc, likely the Sistan (westward) extension of the Chagha-Raskoh Arc in Pakistan-Afghanistan. These results do not support opinions that the Sistan detritus sourced from Himalaya by Palaeo-Indus submarine fan delta complex. Instead, the Eocene - Oligocene detritus was transported by rivers and subsequent turbiditic flows from the Afghan active margin, to the Sistan Basin.

Chapter IV focuses on the origin of the Zahedan and Shah Kuh plutonic rocks, in the southern part of the Sistan Suture Zone, to identify their tectonic affiliation and specify their temporal relation with neighboring Tethyan suture zones. We present U-Pb zircon crystallization ages combined with major and trace element analyses, Sr-Nd isotopes and Hf isotope analyses. The Zahedan and Shah-Kuh Eocene plutons consist in a series of granite-granodiorite-rhyolite dated at ca 40.5-44.3 Ma and ca 28.9-30.9 Ma. Eocene plutons represent mantle magmas contaminated by ca 50% of melt derived from the turbidites of the accretionary wedge in which they have intruded. In Oligocene time, most of the magmas were generated from mantle melting, with assimilation of the surrounding turbidites. The rare setting of within-wedge intrusions is attributed to mantle upwelling reaching wedge sediments at the inception of delamination processes, which sign the end of subduction-related deformational and thermal events in the Sistan Suture Zone.

Chapter V presents a synthesis of the work, summarizes conclusions reached in each chapter and ends with a short outlook. According to our results, the Makran and Sistan basins have different tectono-sedimentary characteristics. The Upper Cretaceous-Oligocene sedimentary rocks of Makran derive from a Middle Jurassic intracontinental rift and a Late Cretaceous-Eocene continental arc to the north. The Eocene-Oligocene sedimentary rocks of south Sistan derive from a Late Cretaceous intra-oceanic island arc and an Eocene continental arc, likely the Chagha-Raskoh Arc in Pakistan-Afghanistan. This study first introduce the Late Cretaceous-Eocene North Makran continental arc, which was located in the north of today Makran accretionary wedge (North of Jaz Murian depression) related to the Fannuj subduction.

Chapter II

Makran Provenance

2. Detrital zircon and provenance analysis of Late Cretaceous-Miocene onshore Iranian Makran strata: implications on the tectonic setting

Ali Mohammadi, Jean-Pierre Burg, Wilfried Winkler, Jonas Ruh, Albrecht von Quadt

This chapter has been submitted to Geological Society of American Bulletin

Abstract

A multidisciplinary provenance study, including sandstone framework, heavy mineral analysis, in situ U-Pb dating of detrital zircon and Hf isotopic ratios of dated zircons, was undertaken on Upper Cretaceous-Miocene deep marine turbiditic and deltaic sandstones of Makran Accretionary Wedge, SE Iran, to determine their sedimentary provenance and tectonic setting. Sandstone framework modes reveal magmatic arc as source of Upper Cretaceous-Oligocene detritus and a recycling source of Miocene sandstones. Heavy mineral assemblages, Cr-spinel and blue amphibole disclose ophiolite and high pressure-low temperature metamorphic rocks (blueschists) as supplementary provenance. 2931 laser ablation ICPMS U-Pb detrital zircon ages on 21 sandstone samples yield three major age peaks at ca 167, 88.7 and 48.9 Ma. 241 in-situ Hf isotope analyses of dated zircons give evidence for dominantly igneous source rocks. Two main detrital zircon ages are identified: 1) abundant Middle Jurassic grains with Hf isotopic compositions of continental crust, suggesting a rifting related magmatic provenance. 2) Upper Cretaceous-Eocene grains with Hf isotopic compositions of continental crust and non-depleted mantle, suggesting a continental magmatic arc provenance. This change in provenance is attributed to the Late Cretaceous convergence between Arabia and Eurasia.

Key words: Makran, turbidite, provenance analysis, detrital zircon, Hf isotopes, tectonic setting.

2.1 Introduction

The Makran, in SE Iran and SW Pakistan, is one of the largest, active accretionary wedges on Earth. This accretionary wedge results from the convergence between the Arabian and Eurasian plates (White and Klitgord, 1976; White, 1982; McCall, 1983; Platt et al., 1985; McCall, 1997, 2002). It extends over ~ 1000 km along strike between the Minab-Zendan dextral fault system in the west and the Chaman sinistral fault in the east (Fig. 2.1). From rear to toe, the Makran accretionary wedge is more than 350 km wide (Platt et al., 1985). The active southern part (100-150 km submarine prism) is separated from a more passive northern part (200-250 km onshore) by normal faults close to today's shoreline (Kukowski et al., 2001; Ellouz-Zimmermann et al., 2007b; Grando and McClay, 2007; Burg et al., 2013). Northward subduction of the Arabian plate initiated during Late Cretaceous. Current subduction rate estimated by GPS measurements is about 2 cm/a in a N-S direction (Vigny et al., 2006; Masson et al., 2007). Southward migration of the Makran wedge toe is ~1 cm/a since the Pleistocene (White and Louden, 1982; Platt et al., 1985). Compared to previous work focussing on seismic profiles offshore Makran (Von Rad et al., 1995; Fruehn et al., 1997; von Rad et al., 1999a; von Rad et al., 1999b; von Rad et al., 2002; Ellouz-Zimmermann et al., 2007b; Grando and McClay, 2007) and on the Pakistani part of the accretionary wedge (Jones, 1960; Platt et al., 1985; Platt and Leggett, 1986; Platt et al., 1988; Kopp et al., 2000), less work has been performed on the onshore Iranian Makran (e.g. McCall and Kidd, 1982; White, 1982; McCall, 1983; McCall, 1985; McCall, 1995, 1997, 2002; Hosseini-Barzi and Talbot, 2003; Burg et al., 2008; Dolati, 2010; Burg et al., 2013; Haghipour, 2013; Ruh, 2013; Ruh et al., 2013; Hunziker et al., 2015).

The provenance of the detrital material in the Makran accretionary wedge has been subject of research for decades (Critelli et al., 1990; Kassi et al., 2007; Carter et al., 2010; Kassi et al., 2013; Kassi et al., 2015). It has been suggested that pre-Miocene sedimentary rocks of eastern Makran were supplied from the Himalaya (Paleo-Indus fan), whereas Miocene to recent deposits were reworked from the growing accretionary wedge (e.g. Critelli et al., 1990; Qayyum et al., 2001; Grigsby et al., 2004; Ellouz-Zimmermann et al., 2007a; Ellouz-Zimmermann et al., 2007b; Kassi et al., 2007; Carter et al., 2010; Kassi et al., 2011; Kassi et al., 2013; Kassi et al., 2015). The present work aims to augment our knowledge of the Mesozoic and Cenozoic geological history of the western (Iranian) Makran by investigating the provenance of Cretaceous to Miocene siliciclastic sandstones. The assessment of the detrital source rocks of sandstones is of great importance for detecting the tectonic evolution of sedimentary basins. We present combined results from fieldwork, modal framework grain composition of the sandstone and heavy mineral analysis to characterize the lithologies in the source areas of the Makran basin from late Cretaceous to Miocene times. Detrital zircon ICP-MS laser ablation U-Pb ages are used to evaluate the crystallization age ranges in the source area. Hf isotope ratios of dated detrital zircons are used to infer the origin of magmas in the source region. Finally, we discuss the sourcing of the detrital material from rifting related magmatic rocks, continental arc and ophiolites. Himalayan-sourced rocks, which were inferred by earlier investigation, were not identified.

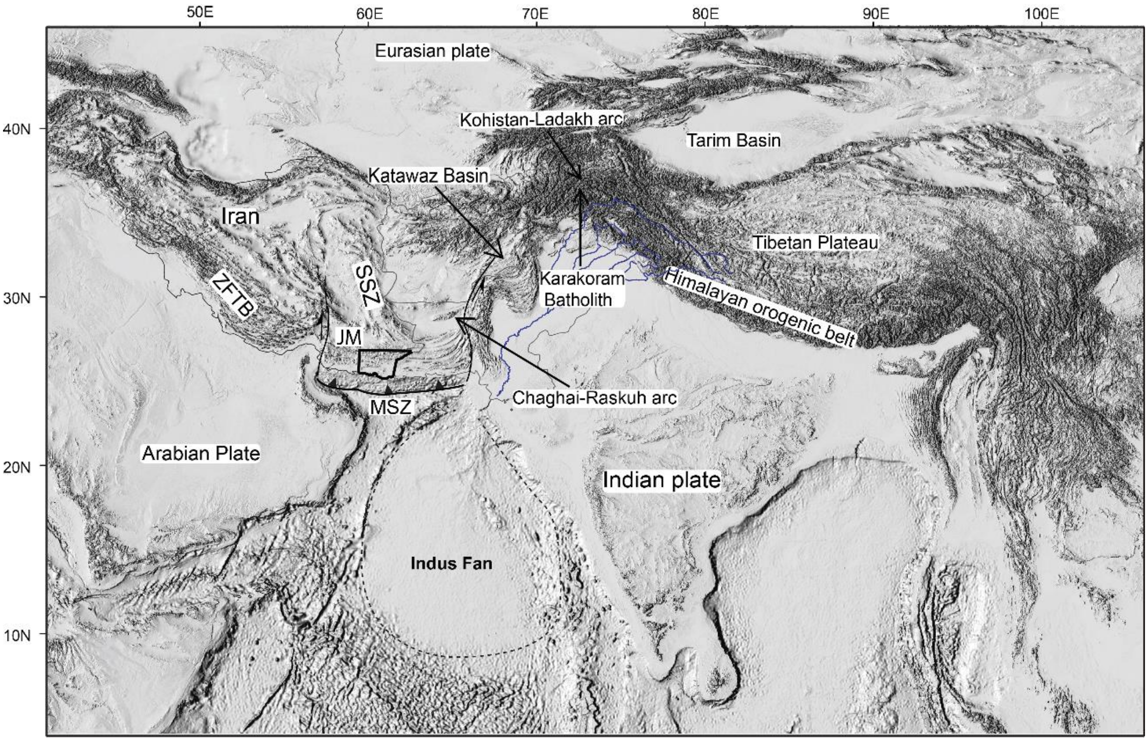

Figure 2.1: Tectonic setting of the Makran subduction zone and Himalayan orogenic belt. Framed: studied area; ZFTB: Zagros Fold and Thrust Belt; SSZ: Sistan Suture Zone; JM: Jaz Murian depression; MSZ: Makran Subduction Zone. Background: shaded relief map ETOPO1 (http://www.ngdc.noaa.gov/mgg/global/relief/ETOPO1).

2.2 Geological framework of studied sandstones

The onshore Iranian Makran is subdivided into four major, east-west oriented zones based on tectonic framework and stratigraphy. These are from north to south, from the structural top to bottom: (1) North Makran, (2) Inner Makran, (3) Outer Makran and (4) Coastal Makran (Dolati, 2010). These four zones are delimited by major thrusts (Fig. 2.2).

North Makran includes: (1) ophiolitic mafic and ultramafic rocks with their upper crustal pillow lavas and Cretaceous deep-marine radiolarites and turbidites; these rocks were eroded and unconformably covered by Upper Cretaceous-Paleocene shallow water sedimentary rocks; (2) the base of these rock units is the Bashakard thrust, which developed tectonic imbrication of ophiolites and intermediate rocks, Upper Cretaceous volcaniclastic sandstones, shales, conglomerates and shallow water limestone and marbles; (3) Small outcrops of Eocene turbidites are scattered in the north-central part.

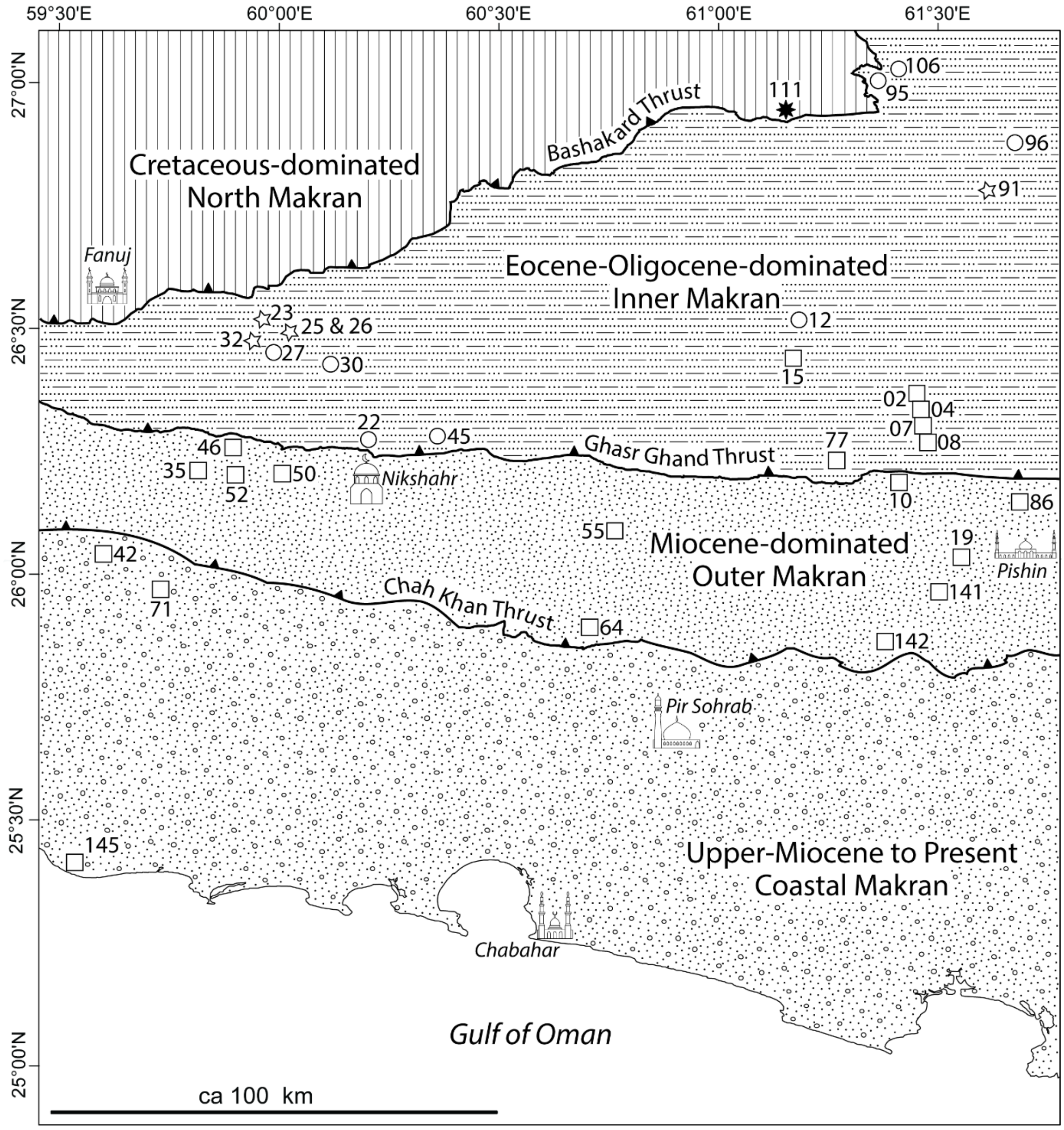

Figure 2.2: Major structural and lithological units of Makran after Dolati (2010). Numbered = location of samples used for U-Pb dating of detrital zirocns; symbols according to stratigraphic age: Eight-branch star = Cretaceous, five-branch stars = Eocene, Circles = Oligocene, Squares = Miocene. Names in italic are main cities.

Inner Makran exposes Eocene-Oligocene and locally Miocene rocks between the Bashakard thrust in the north and the Ghasr Ghand Thrust in the south (Fig. 2.2). In between, several thrust sheets are dominated by: (1) Lower Eocene deep marine sedimentary rocks, pillow lavas and associated volcaniclastic sandstones that grade upwards into Middle Eocene deeper marine turbiditic sequences; (2) Lower Oligocene shale-dominated distal (outer fan) turbidites that grade into Upper Oligocene sandstone-dominated inner and outer fan turbidites followed by Uppermost Oligocene shale-dominated slope and delta turbidites. This upward more clastic and proximal evolution suggests progradation of submarine fans followed by the deposition of slope sediments grading into pro-delta turbidites; (3) Lower Miocene sedimentary rocks dominated by marl and calcareous shallow water sandstones passing to Middle Miocene deltaic sandstones and shales.

The Lower Miocene pro-delta turbidites are grading upward to shallow shelf, deltaic and tidal sandstones and shales. Miocene synsedimentary deformation is testified by growth structures and the upward shallowing of sedimentary facies (Dolati, 2010; Figs. 2.2; 2.3).

Outer Makran mostly exposes Lower to Middle Miocene sedimentary rocks between the Ghasr Ghand and Chah Khan Thrusts (Fig. 2.2). The Lower Miocene is dominated by marls and thick-bedded sandstones that grade laterally into shallow shelf, deltaic and tidal calcareous sandstones, siltstones, marls and coral limestones. The Middle Miocene sandstone and shale dominated deep marine turbidites grade up-section to the shallowing upward deposition to shelf environment (Fig. 2.3).

Coastal Makran, between the Chah Khan thrust in the north and the coast (Fig. 2.2), is covered by Upper Miocene marlstone, channelized calcareous sandstones and polymictic conglomerates with mollusc shells, herringbone structures and mud cracks suggesting a shallow-water depositional environment. Pliocene-Pleistocene shallow-water calcareous sandstones and marls are overlain by Pliocene-Pleistocene thick-layered continental conglomerates. Generally, Coastal Makran preserves a fill-up basin of Pliocene age (Dolati, 2010; Figs. 2.2; 2.3).

2.3 Methods

Thirty-four medium-grained turbiditic and deltaic sandstones (with prefix 11 AM and 12 AM in the ETH collection) from eleven lithostratigraphic units of the onshore Makran accretionary wedge have been investigated (Figs. 2.2; 2.3; Table. 2.1). We combined sandstone framework, heavy mineral study, detrital zircon U-Pb ages and Hf-isotopic ratios of dated zircons to reconstruct the lithological composition of the source-rocks and the tectonic evolution of the source area. Analytical methods including separation, identification and quantification techniques are described in Appendix A.

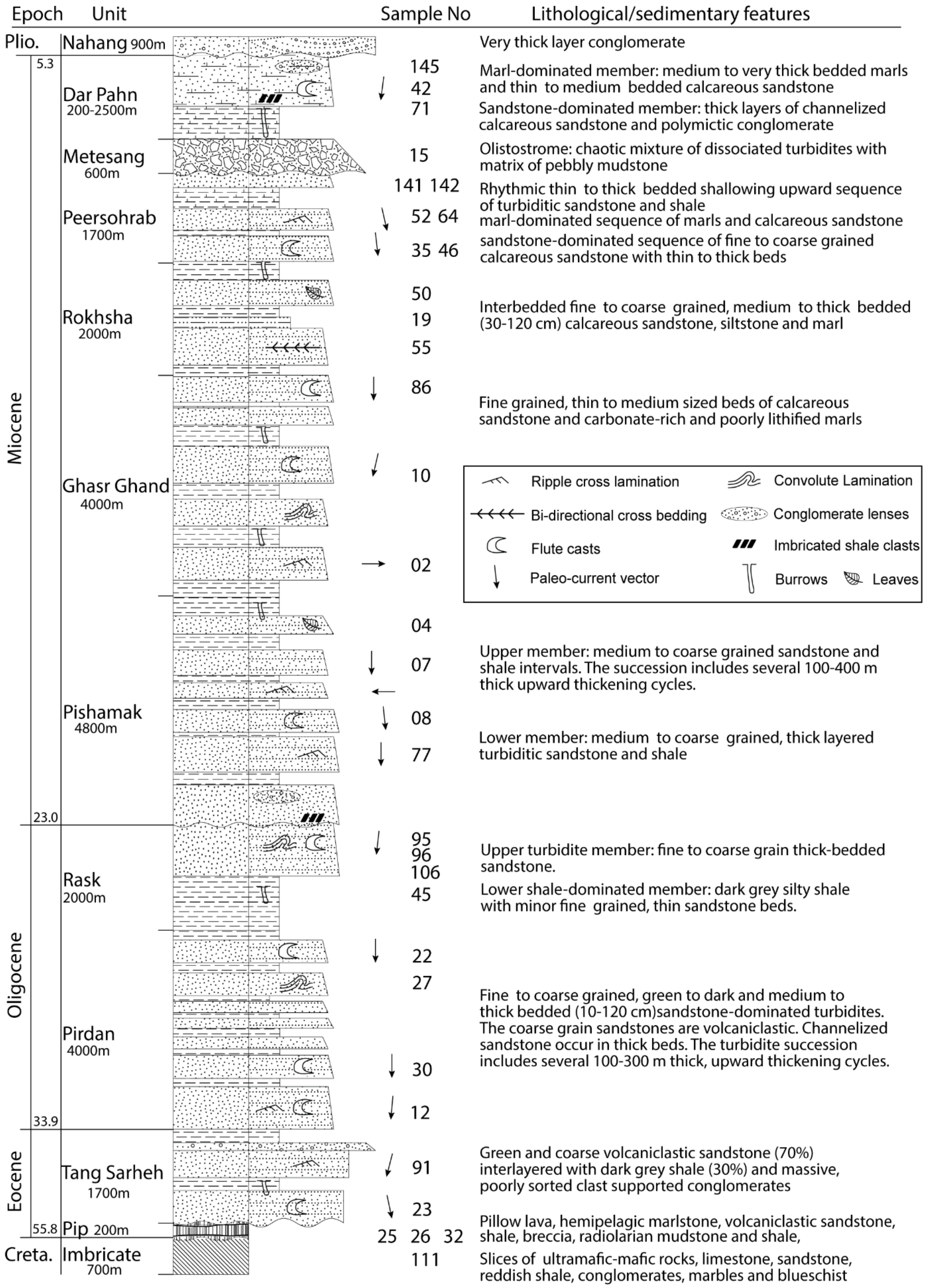

Figure 2.3: Composite stratigraphic section of the onshore Makran accretionary wedge with paleocurrent directions, sedimentary structures, sampling points and comments on lithological and sedimentary features.

Table 2.1. Geographical location (degree, minute, second), ages and characteristics of the analyzed samples in the Makran sandstones.

Sample No:	**Latitude N deg min sec**	**Longitude E deg min sec**	**Stratigraphic age**	**Stratigraphic age**	**Lithology / infered depositional environment**	**MFA**	**HM**	**DZA**
11 AM 02	26 22 38	61 26 06	Miocene	Aquitanian- Lower Burdigalian	Medium grained sandstone with hummocky cross-bedding, deltaic	MFA	HM	DZA
11 AM 04	26 21 47	61 26 17	Miocene	Aquitanian- Burdigalian	Fine grained turbidity sandstone	MFA	HM	DZA
11 AM 07	26 19 31	61 24 07	Miocene	Aquitanian- Burdigalian	Fine grained turbidity sandstone, bioturbation	MFA	HM	DZA
11 AM 08	26 19 25	61 25 07	Miocene	Aquitanian- Burdigalian	Fine grained turbidity sandstone with flute cast	MFA	HM	DZA
11 AM 10	26 12 59	61 25 35	Miocene	Aquitanian- Lower Burdigalian	Coarse grained turbidity sandstone with flute cast	MFA	HM	DZA
11 AM 12	26 30 49	61 11 14	Oligocene	Upper Rupelian- Lower Chattian	Fine grained turbidity sandstone with flute cast	MFA		
11 AM 15	26 28 45	61 14 26	Miocene	Tortonian	Medium grianed sandstone, oliststorme	MFA	HM	DZA
11 AM 19	26 03 31	61 32 03	Miocene	Upper Burdigalian	Fine grained turbidity sandstone with flute cast, alternated with bioturbated shale	MFA	HM	DZA
11 AM 22	26 16 53	60 10 27	Oligocene	Upper Rupelian- Lower Chattian	Fine grained turbidity sandstone	MFA	HM	DZA
11 AM 23	26 31 47	59 57 15	Eocene	Lutrtian- B35artonian- Priabonian	Fine grained turbidity sandstone, alternated with bioturbated shale	MFA	HM	DZA
11 AM 25	26 29 08	59 59 08	Eocene	Upper Yepresian- Lower Lutetian	Coarse grained pyroclastic sandstone, greenish		HM	
11 AM 26	26 29 17	59 58 45	Eocene	Upper Yepresian- Lower Lutetian	Pyroclastic sandstone, yellowish	MFA	HM	
11 AM 27	26 28 13	60 00 09	Oligocene	Upper Rupelian- Chattian	Coarse grained turbidity sandstone with ripple cast, alternated with bioturbated shale	MFA	HM	DZA
11 AM 30	26 28 14	60.01 43	Oligocene	Upper Rupelian- Chattian	Coarse grained sandstone, strongly weathered	MFA		
11 AM 32	26 30 59	59 57 31	Eocene	Upper Yepresian- Lower Lutetian	Medium grained pyroclastic sandstone, greenish	MFA	HM	DZA
11 AM 35	26 17 21	59 54 25	Miocene	Langhian- Lower Serravallian	Medium to coarse grained sandstone, deltaic	MFA		
11 AM 42	26 03 16	59 40 05	Miocene	Upper Tortonian- Lower Messinian	Medium to coarse grained sandstone, deltaic	MFA		
11 AM 45	26 19 28	60 23 18	Oligocene	Chattian	Coarse grained sandstone with flute cast	MFA	HM	
11 AM 46	26 17 16	59 55 16	Miocene	Langhian- Lower Serravallian	Coarse grained sandstone with through cross-bedding	MFA	HM	DZA
11 AM 50	26 12 58	60 02 01	Miocene	Upper Burdigalian	Medium grained sandstone with flute cast	MFA		
11 AM 52	26 15 32	59 56 54	Miocene	Upper Burdigalian	Medium to coarse grained sandstone with through cross-bedding, deltaic	MFA	HM	DZA
11 AM 55	26 07 22	60 57 31	Miocene	Upper Burdigalian	Coarse grained sandstone with through cross-bedding, deltaic	MFA	HM	DZA
11 AM 64	25 56 48	60 37 37	Miocene	Langhian- Lower Serravallian	Coarse grained sandstone with flute cast, bioturbation, deltaic	MFA		
11 AM 71	25 59 52	59 46 26	Miocene	Upper Tortonian- Lower Messinian	Medium grained sandstone with through cross-bedding, shelf environment	MFA	HM	DZA
11 AM 77	26 21 52	61 19 13	Miocene	Aquitanian- Burdigalian	Fine grained turbidity sandstone, alternated with bioturbated shale	MFA		
11 AM 86	26 12 50	61 43 17	Miocene	Aquitanian- Lower Burdigalian	Medium grained sandstone with ripple mark and bioturbation	MFA	HM	
11 AM 91	26 48 51	61 36 07	Eocene	Lutetian- Bartonian- Priabonian	Medium grained sandstone with ripple mark	MFA	HM	DZA
12 AM 95	27 03 48	61 21 06	Oligocene	Chattian	Fine grained turbidity sandstone with flute cast and load cast	MFA	HM	DZA
12 AM 96	26 54 47	61 35 59	Oligocene	Chattian	Medium grained turbidity sandstone with cross-bedding	MFA		
12 AM 106	27 03 41	61 22 58	Oligocene	Chattian	Fine grained turbidity sandstone alternation with shale, bioturbation	MFA	HM	DZA
12 AM 111	26 57 39	61 09 18	Cretaceous	Upper Certaceous	Fine grained sandstone in imbricate zone	MFA	HM	DZA
12 AM 141	26 01 50	61 30 49	Miocene	Langhian- Lower Serravallian	Medium grained sandstone with ripple mark	MFA	HM	DZA
12 AM 142	25 59 43	61 29 11	Miocene	Langhian- Lower Serravallian	Fine grained sandstone with ripple mark	MFA	HM	DZA
12 AM 145	25 30 26	59 59 48	Miocene	Upper Tortonian- Lower Messinian	Dark colour medium grained sandstone, fossil placer on the beach		HM	DZA

Analysis key: MFA: modal framework analysis, HM: heavy minerals, DZA: detrital zircon age and Hafnium isotopes.

2.4 Results

2.4.1 Paleocurrents

Paleocurrent directions (61 in Eocene, 58 in Oligocene and 133 in Miocene sandstones)were measured from 229 flute casts and 23 asymmetric ripple marks. Readings were rotated to horizontal around the local strike direction of bedding. Measurements indicate a regional N to S paleoslope with a source area to the north of the Makran basin (Fig. 2.4).

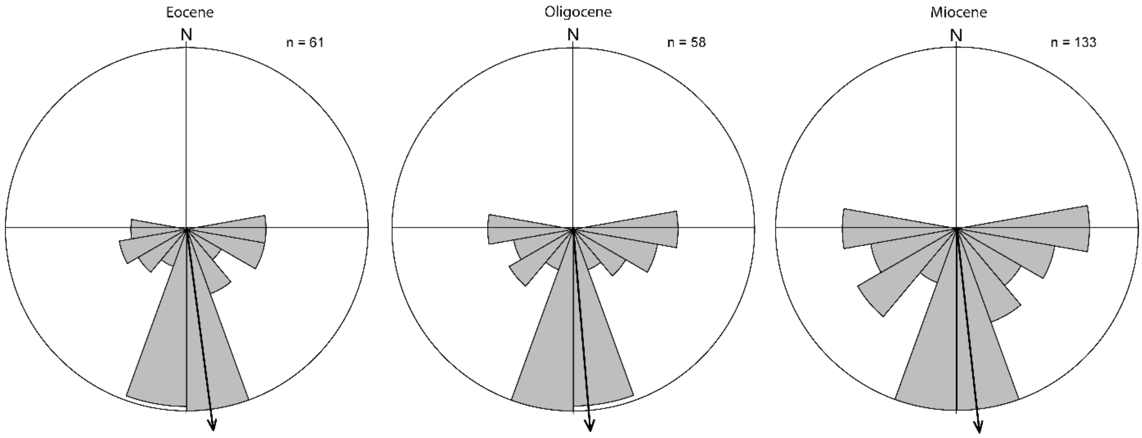

Figure 2.4: Rose diagrams of paleocurrent measurements from 229 flute casts and 23 asymmetric ripple marks restored to horizontal around the local strike of bedding. Arrow: average direction.

2.4.2 Modal framework

The studied sandstones classify mainly as feldspathic litharenite, lithic arkose and litharenite (Fig. 2.5a). Quartz grains are mostly mono-crystalline (75%) and feldspar is dominantly plagioclase (>90%) with minor amounts of K-feldspar (Fig. 2.5b). Rock fragments are represented by sedimentary, volcanic and metamorphic grains (Figs. 2.5c, d). Volcanic rock fragments are mainly andesite and volcanic glass. Sedimentary lithic grains mainly comprise siltstone, limestone and dolomite. Metamorphic lithic grains generally consist of low-grade to medium-grade phyllites and schists. The transitional-dissected arc nature of the source ternaries is inferred for the Eocene-Oligocene sandstones. A recycled orogenic nature of the source area is implied for most of the Miocene detritus (Figs. 2.5e, f).

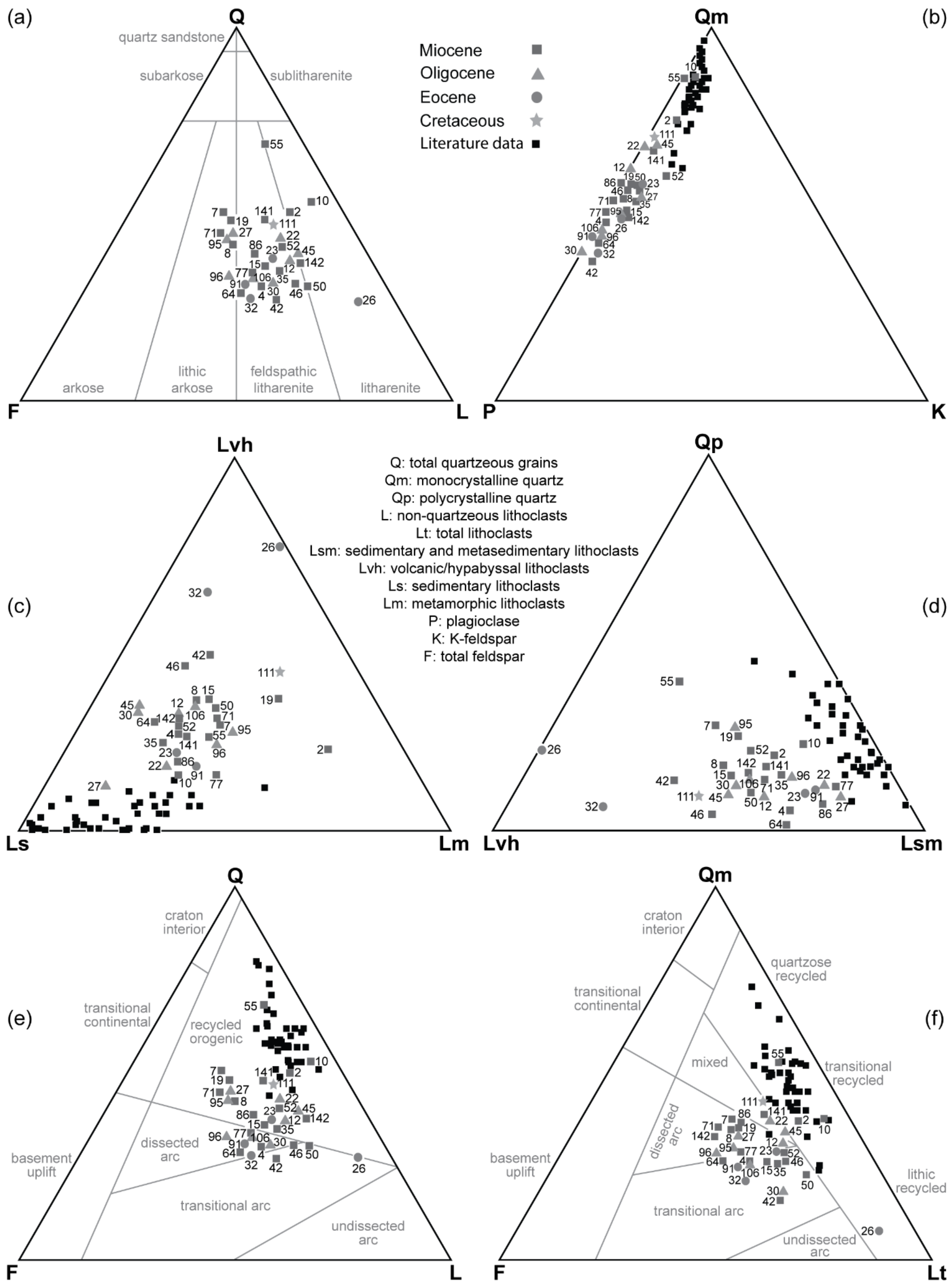

Figure 2.5: Detrital composition and classification of the Makran sandstones in provenance discrimination diagrams: (a) sandstone classification diagram Folk (1980); (b) Qm-P-K diagram after Dickinson and Suczek (1979); (c) Lvh-Ls-Lm diagram after Dickinson (1985); (d) Qp-Lvh-Lsm diagram after Dickinson and Suczek (1979); (e) QFL Dickinson (1985) and (f) QmFLt Dickinson (1985). Literature data on Katawas basin from Qayyum et al. (1996)

2.4.3 Heavy minerals

Heavy mineral suites show very variable compositions including (1) ultra-stable minerals (zircon, tourmaline, rutile, monazite, brookite, anatase and sphene; ZTR = 3-76% of 200 counted grains) and apatite derived from continental crust sources and recycled sandstones (Mange and Wright, 2007). Most detrital zircon crystals (80%) are euhedral to anhedral, suggesting short transport distances from source to sink. (2) a group of metastable minerals (epidote group, garnet, staurolite, chloritoid, kyanite, andalusite and blue amphibole shows a variably abundant (1 to 72% of 200 counted grains) in heavy mineral assemblage, which suggests variable detrital sources, mainly in medium-grade metamorphic rocks or in garnet-bearing granitoids, (3) Cr-spinel (up to 12% of total grain count) implies partly important sourcing of the detrital material from ophiolitic ultramafic rocks, (4) hornblende (up to 23% of total grain count) either supplied from basic metamorphic or igneous rocks, and (5) a local pyroxene-rich source (up to 88% of total grain count) in Eocene pyroclastic sandstone formations overlying pillow lavas (Fig. 2.6, samples 25 and 26). Early Eocene pyroclastic sandstones generally show more volcanic minerals (up to 95%; samples 25 and 26, Fig. 2.6). Blue amphibole (5-20%) occurs in several samples of Eocene-Oligocene and Miocene sandstones (Fig. 2.6).

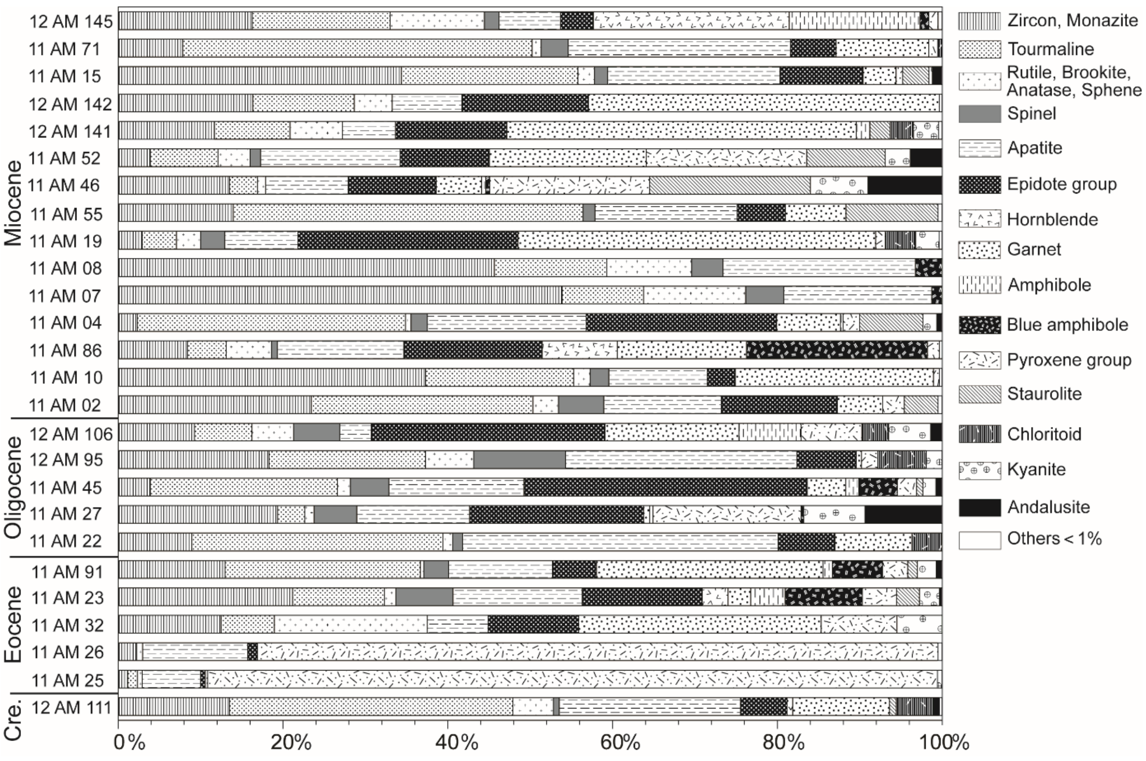

Figure 2.6: Heavy mineral assemblages of the Makran accretionary wedge sandstones arranged in reconstructed stratigraphical order, showing the relative abundance of heavy mineral species.

Early Miocene deltaic sandstones in Outer Makran (samples 07, 08 and 55) reveal high amounts of ZTR minerals (64 to 81% of total grain count; Fig. 2.6). The negative and positive trend of the ZTR indexes, respectively, with sandstone ages (Morton and Hallsworth, 1999) indicates that the proportion of metastable grains in the heavy mineral assemblage decreases with time (Fig. 2.7). This implies that the heavy mineral content is partly controlled by cannibalism and recycling.

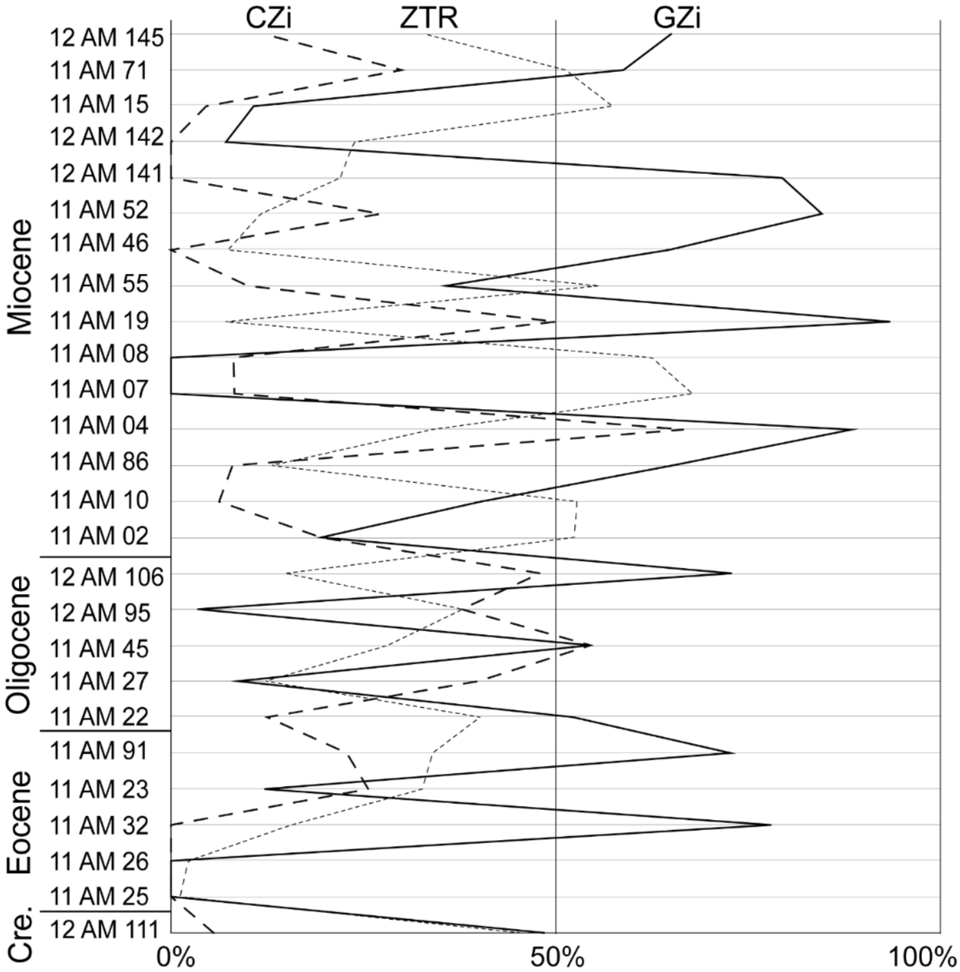

Figure 2.7: Provenance-sensitive heavy minerals index ratios (Morton and Hallsworth, 1999) calculated for sandstones in the Makran accretionary wedge. GZi = [garnet / (garnet + zircon)]×100; CZi = [chromian spinel / (chromian spinel + zircon)]×100; ZTR = zircon + tourmaline + rutile.

2.4.4 Detrital zircon dating and Hf isotope geochemistry

U-Pb dating by laser ablations ICP-MS on detrital zircons was conducted on 21 Upper Cretaceous to Miocene turbiditic and deltaic sandstone samples (Fig. 2.2; Table. 2.1). Only concordant ages were used, as shown in Concordia diagrams with probability density curves for each sample (Figs. 2.8; 2.9; 2.10; 2.11a, b). Zircon ages older than 1100 Ma were not plotted due to their rarity. The results call attention to strong Middle Jurassic, Late Cretaceous and Eocene magmatic activity in the source areas. In western Makran dominant zircon age populations of Eocene-Oligocene sandstones are peaking at 87 Ma (Late Cretaceous) and 48.4 Ma (Eocene). The Miocene sandstone of western Makran have zircon ages similar to the Eocene-Oligocene sandstones and few Middle Jurassic grains (main peak at 165.8 Ma; Fig. 2.11a). In eastern Makran age distributions are peaking at 167 Ma (Mid Jurassic), 88.7 Ma (Late Cretaceous) and 48.9 Ma

(Eocene; Fig. 2.11b). Neoproterozoic-Cambrian (563-868 Ma) zircon grains are in minor amount (≤ 5% of total zircon grain). The contemporaneous occurrence of Eocene zircons in Eocene sedimentary rocks implies syn-sedimentary magmatism and short-time reworking of magmatic zircons in the basin (Fig. 2.12).

The hafnium isotope ratio analysis was performed on dated zircon grains large enough and with internal growth structures thick enough for laser beams (30 and 60 µm for U-Pb dating and Hf analyses, respectively).Zircons older than 600 Ma were not analyzed because of their rarity and low importance for the present purpose. Middle Jurassic evolved epsilon hafnium ε-$Hf_{(t)}$ ranges from +2 to -13 (Fig. 2.13). Negative ε-$Hf_{(t)}$ suggest magmatic zircons with continental crust signature. Zircons with Cretaceous-Eocene ages show a large variation in ε-$Hf_{(t)}$ from -17 to +14. The Hf isotopic composition for zircons, clustering at 95-145 Ma (Early Cretaceous) indicate ε-$Hf_{(t)}$ values of -17 to +11. Zircons at 33-95 Ma (Late Cretaceous-Eocene) show ε-$Hf_{(t)}$ values of -6 to +14 with three grains between -11 and -17 (Fig. 2.13). Compared to the Middle Jurassic zircons, Upper Cretaceous and Eocene zircons show more positive ε-$Hf_{(t)}$ between the (CHUR) and depleted mantle lines. Mixed positive and negative ε-$Hf_{(t)}$ values indicate continental crust and non-depleted mantle signatures as for subduction-related magmatism in continental arcs (Patchett, 1983; Blichert-Toft and Albarède, 1997; Naing et al., 2014).

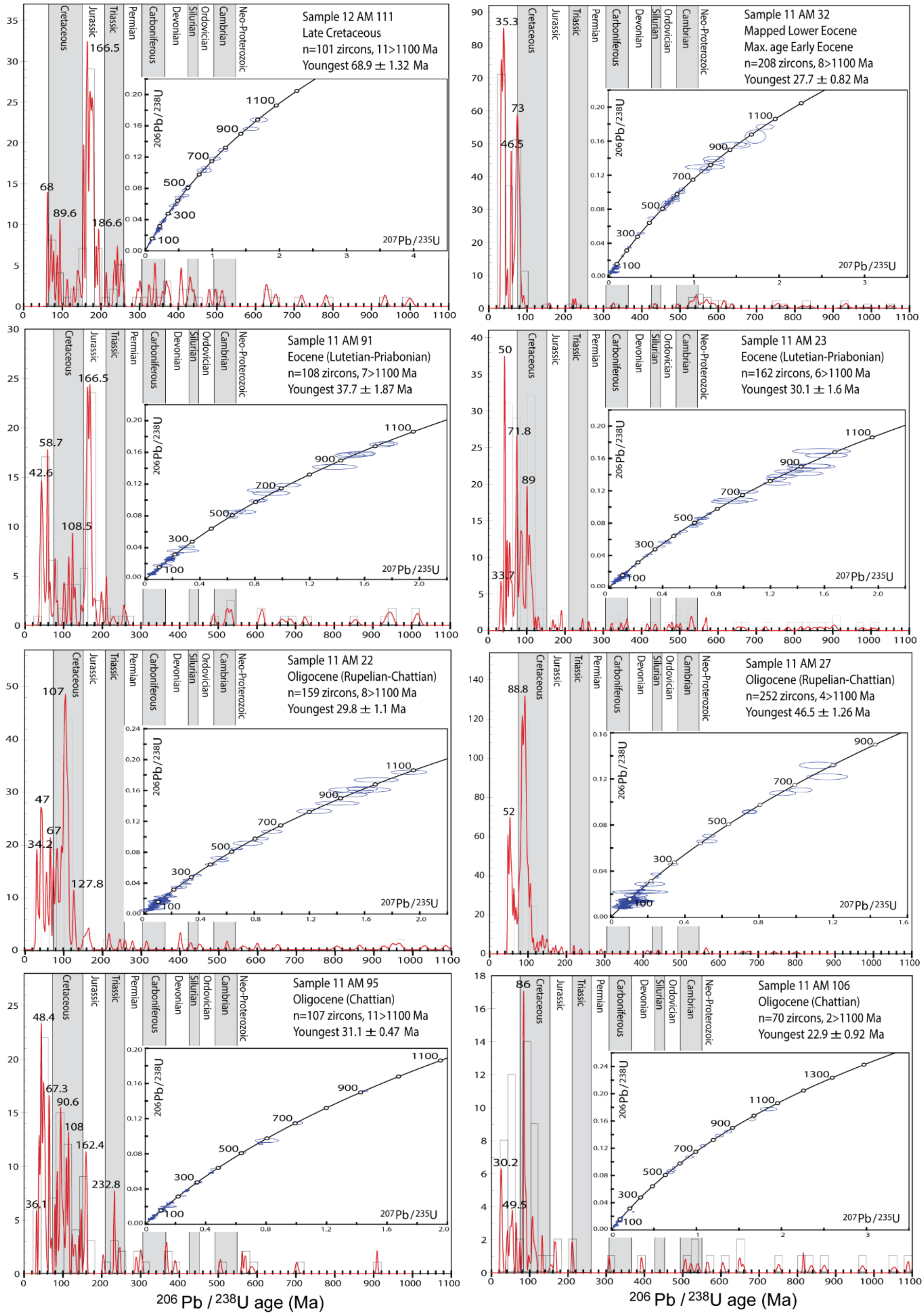

Figure 2.8: Probability density diagrams for detrital zircon $^{206}Pb/^{238}U$ age populations with corresponding Concordia plots of concordant detrital zircons of the samples 111, 32, 91, 23, 22, 27, 95 and 106. Ages with discordance greater than 5% are not included. Time scale after Gradstein et al. (2012).

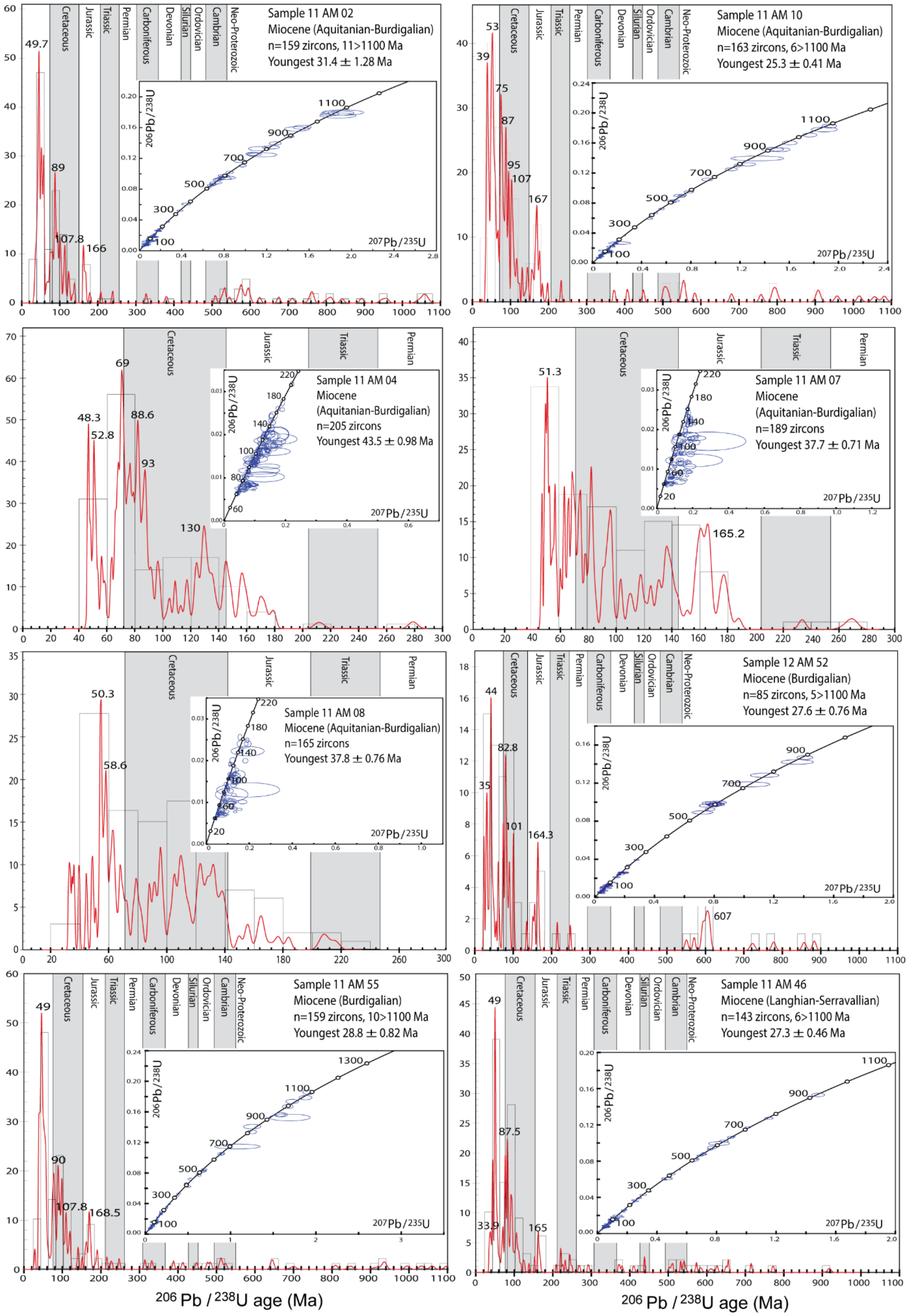

Figure 2.9: Probability density diagrams for detrital zircon $^{206}Pb/^{238}U$ age populations with corresponding Concordia plots of concordant detrital zircons of samples 02, 10, 04, 07, 08, 52 55 and 46. Ages with discordance greater than 5% are not included. Time scale after Gradstein et al. (2012).

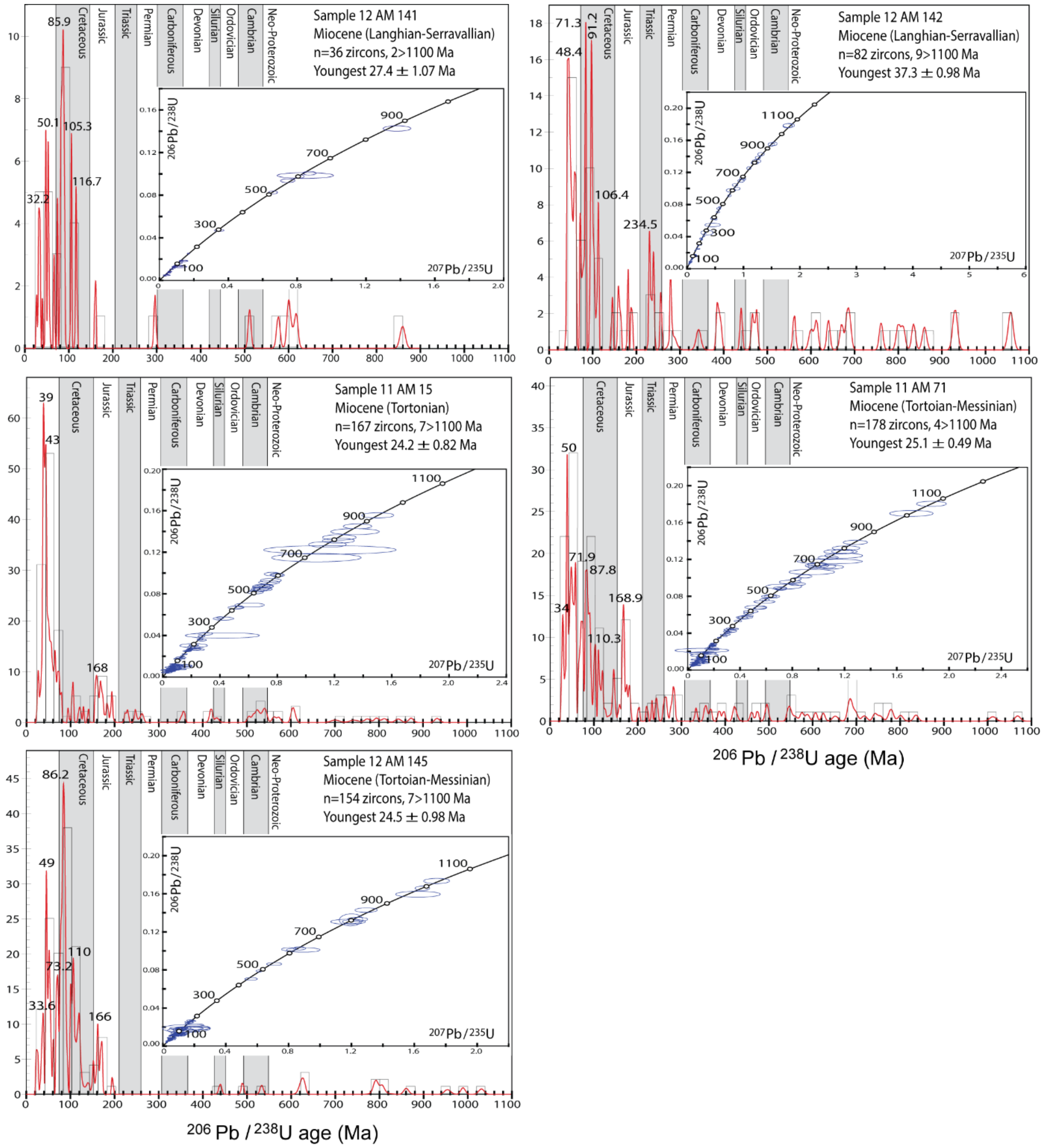

Figure 2.10: Probability density diagrams for detrital zircon $^{206}Pb/^{238}U$ age populations with corresponding Concordia plots of concordant detrital zircons of samples 141, 142, 15, 71 and 145. Ages with discordance greater than 5% are not included. Time scale after Gradstein et al. (2012).

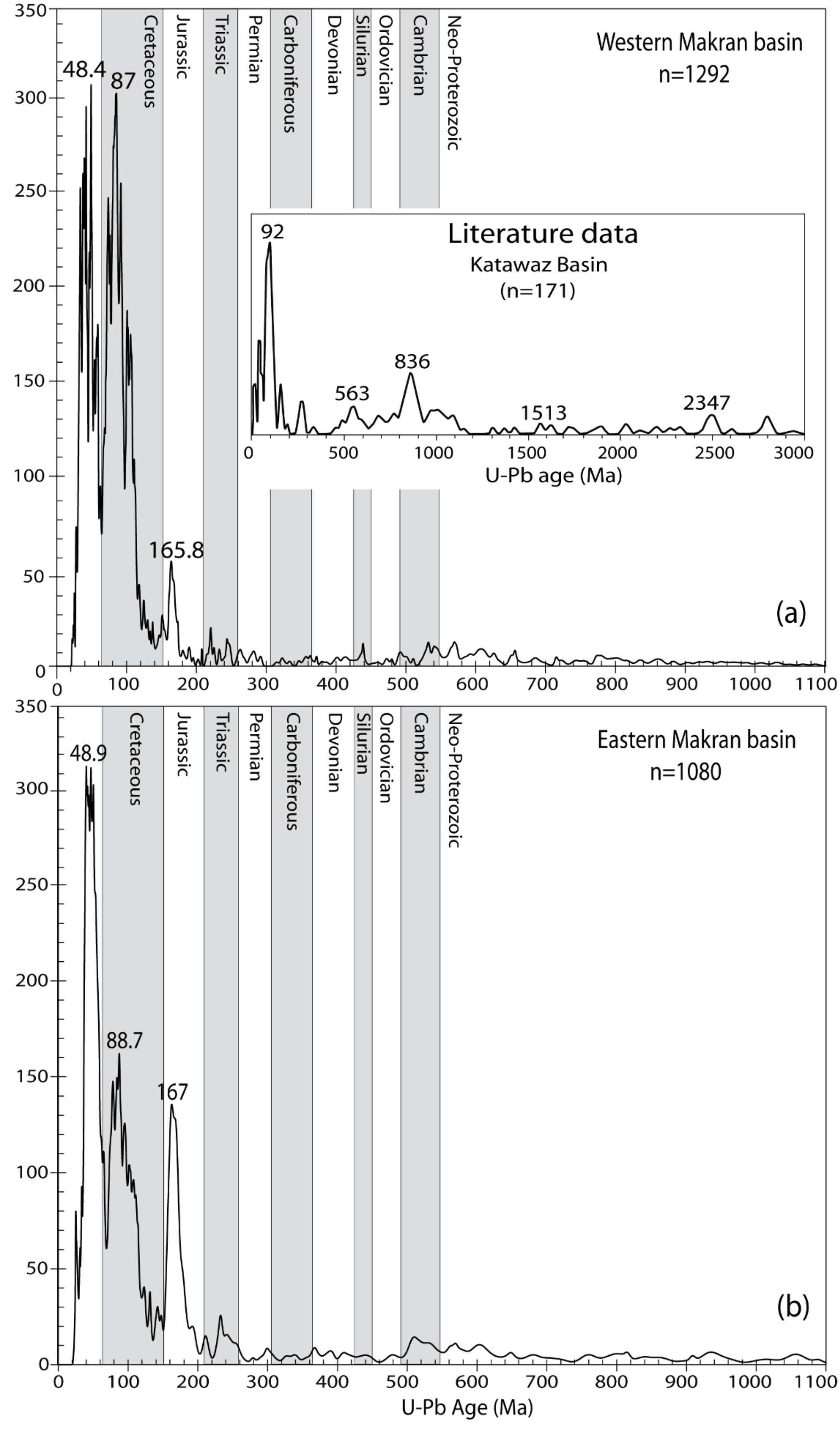

Figure 2.11: U-Pb age distribution pattern of all sandstone samples from the Makran Basin. (a) Western Makran Basin; (b) eastern Makran Basin. Literature data on Makran and Katawas Basins from Carter et al. (2010). Time scale after Gradstein et al. (2012).

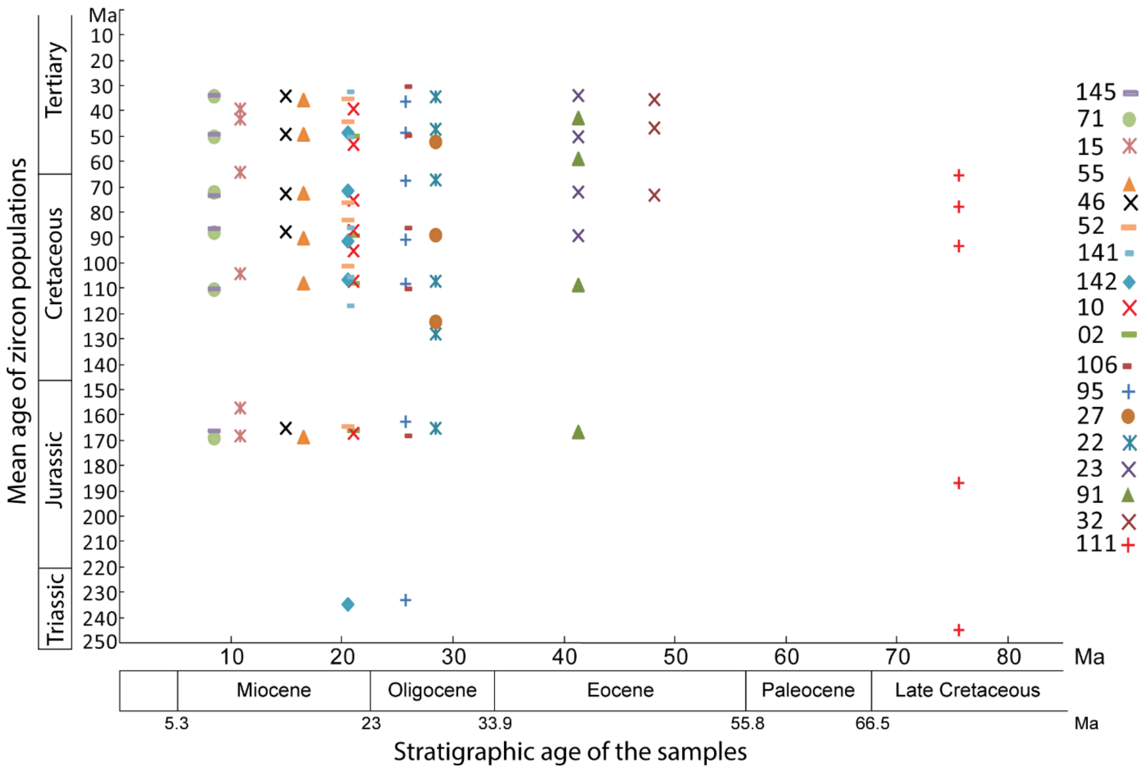

Figure 2.12: Zircon mean age populations versus stratigraphic age of the Makran sandstones. Time scale after Gradstein et al. (2012).

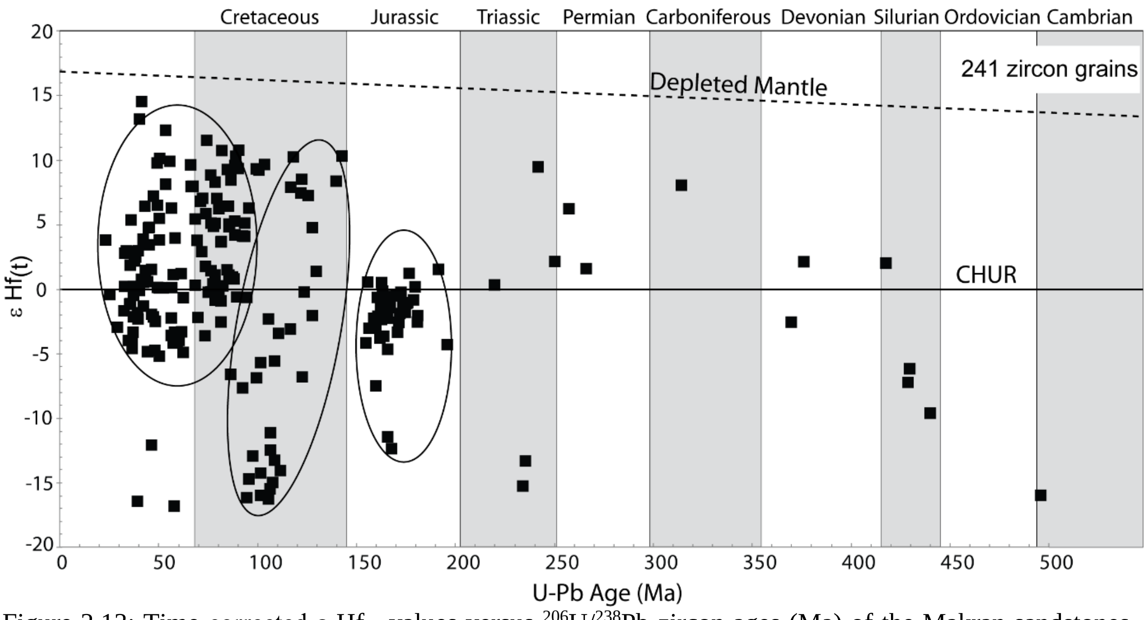

Figure 2.13: Time-corrected ε-$Hf_{(t)}$ values versus $^{206}U/^{238}Pb$ zircon ages (Ma) of the Makran sandstones. Age correction based on chondritic values (CHUR) from Blichert-Toft and Albarède (1997). Depleted Mantle evolution trend (dashed line) from Griffin et al. (2000). Time scale after Gradstein et al. (2012).

2.5 Discussion

Middle Jurassic (167 Ma), Late Cretaceous (68-89 Ma) and Eocene (33-49 Ma), major age populations characterize Makran detrital zircon grains. The Hf isotopic ratios and the provenance analysis authenticate separating three main magmatic pulses.

2.5.1 Upper Cretaceous sandstones

Upper Cretaceous sandstone from North Makran have two detrital zircon populations with main peaks at 166.5 Ma (Middle Jurassic) and 68-89 Ma (Late Cretaceous; Fig. 2.8). Considering the euhedral to anhedral shape (≥ 80%) and magmatic zoning, the Middle Jurassic peak is attributable to igneous rocks. Early Middle Jurassic (170-176 Ma) and Middle Jurassic (160-166.6 Ma) granitoids are actually known in North Makran and its probable northwestern continuation in the so-called Sanandaj-Sirjan magmatic belt (e.g. Hunziker et al., 2015). Petrology, geochemistry and Rb-Sr as well as Nd-Sm isotopes suggest that these granitoids originated during extension/thinning and subsequent partial melting of a continental crust (Hunziker et al., 2015). This interpretation fits the negative $\varepsilon\text{-Hf}_{(t)}$ values of the analyzed Middle Jurassic zircons, which support derivation from continental igneous rocks being eroded in the Late Cretaceous (Fig. 2.13). The Mid-Jurassic detrital zircons occur in the Upper Cretaceous to Oligocene sandstones of the eastern part of the studied Makran basin only, whereas Upper Cretaceous - Eocene zircons are ubiquitous in both the eastern and western part of the Makran Basin. This age distribution suggests that two sub marine fans supplied detritus in the western and eastern parts of the basin.The lack of Mid Jurassic detrital zircons in the western part suggests, along with paleocurrent directions, that Middle Jurassic source rocks were located to the northeast of North Makran.

Other sources can be considered for the Upper Cretaceous detrital zircons: (1) the western Himalayan thrust belt and the Cretaceous-Cenozoic Trans-Himalayan magmatic arc and (2) the Semail ophiolite in Oman. Garzanti and Hu (2014) suggested from the provenance study of Upper Cretaceous to Early Paleogene Himalayan sandstones (Zanskar Zone and South Tibet) that the source was the Indian shield, not the Trans-Himalayan arc. Geochemical analyses of Cr-spinel indicate that the Yarlung-Tsangpo ophiolites in South Tibet were not exposed and eroded before the end of Early Eocene (Hu et al., 2014). Therefore Cr-spinel in Upper Cretaceous Makran sandstones do not emanate from the Indus - Tsangpo suture zone. Himalayan regions can therefore be discarded. The Semail ophiolite is incompatible with the N-S directed paleocurrents. In addition, 1) Zircon U-Pb ages from the Semail ophiolite are 91-98 Ma (Chen and Pallister, 1981; Tilton et al., 1981; Warren et al., 2005; Rioux et al., 2012) while Makran sandstones reveal the coeval presence of 48.4-167 Ma zircon age populations. 2) The Oman ophiolites were directly produced from the mantle (Godard et al., 2000; Bosch et al., 2004; Hanghøj et al., 2010) but Makran detrital zircons formed in magmas with continental signatures; 3) Large amounts of quartz and feldspar (52-78%) in Eocene-Oligocene sandstones could not be supplied from an ophiolitic ultramafic source; 4) Heavy mineral assemblages, large quantities of ultra-stable heavy minerals (ZTR) and apatite in Makran sandstones also exclude purely ultramafic source rocks. The presence of Cr-spinel in Upper Cretaceous sandstones places other ophiolites to the north Makran as a secondary sediment source.

2.5.2 Eocene - Oligocene sandstones

The main hypothesis proposed for provenance of Makran sandstones is supply from the Himalayas in the Paleo-Indus delta-submarine fan (e.g. Qayyum et al., 2001; Ellouz-Zimmermann et al., 2007b; Carter et al., 2010; Kassi et al., 2015). Comparison of Makran and West-Himalaya Eocene-Oligocene sandstones (the Katawas Basin and the Sulaiman fold-and-thrust belt, both in Pakistan) rebuffs this hypothesis.

2.5.2.1 Evidence from sandstone framework analysis

The modal framework analysis shows that sandstones of the Iranian Makran are dominantly composed of sedimentary and volcanic lithic fragments with subordinate metamorphic lithics (Figs. 2.5c, d), which specify provenance from a magmatic arc. Qayyum et al. (1996) reported that the Upper Eocene to Early Miocene sandstones of the Katawas Basin are dominantly composed of sedimentary lithics with subordinate low-grade metamorphic clasts and few volcanic lithic fragments (Figs. 2.5c, d), from which detritus from the High Himalaya was inferred. Qayyum et al. (1996) further suggested that two parallel west-flowing rivers north and south of the Himalaya formed the Katawaz Delta at the western margin of the Katawaz Basin, an embayment of the Tethys Ocean during the Eocene-Oligocene. These authors identified the northern stream as the Palaeo-Indus. They additionally opined that the sediments of the Katawas Delta were transported westwards into the Khojak submarine fan, now in the south Pakistan and southeast Iran Makran. The arc sourcing of Makran sandstones does not compare the recycled orogeny character of the Katawas sandstones. Therefore, we cannot follow Qayyum et al. (1996) in their interpretation.

2.5.2.2 Evidence from heavy mineral assemblage

ZTR + apatite as dominant heavy minerals and Cr-spinel and blue amphibole as key heavy minerals are present in both the eastern and western Makran sandstones (Fig. 2.6). ZTR + apatite indicate continental magmatic rocks as dominant provenance, while Cr-spinel and blue amphibole suggest subordinate ophiolite and high pressure/low temperature metamorphic rock provenances. Such rocks are exposed in North Makran (McCall, 1983; Dolati, 2010; Hunziker, 2014). ZTR+apatite and Cr-spinel are heavy mineral assemblages in both Makran and Katawas basins but blue amphibole is not reported in the latter (Carter et al., 2010). Furthermore, zircon, apatite and epidote together constitute 30-40% of the total assemblages in Makran sandstones and are absent in the Early Oligocene sandstones of the Sulaiman fold-and-thrust belt, also in Pakistan (Roddaz et al., 2011). It is worth nothing that blue amphibole is also lacking in the entire Oligocene sequence of the Sulaiman fold-and-thrust belt. We conclude that the Makran and the Katawas basins had separate source regions.

2.5.2.3 Evidence from zircon U/Pd age and Hf data

Our zircon U-Pb data shows ages ranging between 167 and 33 Ma with peaks at 167, 87-88.7 and 48 Ma and few Proterozoic-Cambrian (563-836) zircons (Figs. 2.8; 2.11a, b). The detrital U-Pb ages from the Katawas Basin show a major peak at 92-93 Ma and a secondary peak at 563-868 Ma (Carter et al., 2010; Fig. 2.11a). Therefore, sediments of the Katawas Basin were not recycled in the studied Makran.

The ε-$Nd_{(t)}$ and Pb isotopic composition of detrital K-feldspar reported from the Makran deep sea turbidites are less negative than those reported from the Higher Himalaya (Clift et al., 2002) , thus contradicts the Himalayas as the source of detritus in the Makran Basin via the Paleo-Indus fan. The ε-$Hf_{(t)}$ values of Mid Jurassic zircons are same as those obtained from the Upper Cretaceous sandstones (Fig. 2.13). However, Upper Cretaceous - Eocene detrital zircons have ε-$Hf_{(t)}$ values typical of continental magmatic arcs (e.g. Patchett, 1983; Blichert-Toft and Albarède, 1997; Naing et al., 2014). The euhedral to anhedral shapes of the detrital zircons suppose short sediment transport distances between the source and the basin. In accordance with the north-south paleo-slope of the Makran Basin, we conclude that there was a Cretaceous-Eocene magmatic arc to the north, not far from North Makran. This fits tectonic reconstructions with the Makran subduction starting in the Late Cretaceous (e.g. Berberian and King, 1981).

2.5.3 Miocene sandstones

The composition of Makran Miocene sandstones is similar to that of the Eocene-Oligocene sandstones with a slightly larger amount of quartz grains and fewer feldspar and volcanic lithic grains. Subsequently, monocrystalline quartz/polycrystalline quartz ratio in Miocene sandstones is slightly larger than that in Eocene-Oligocene sandstones (Figs. 2.5b, c, d). The heavy mineral spectrum is also similar to that of Eocene-Oligocene sandstones with slightly more ZTR minerals and less amount metastable volcanic and metamorphic heavy minerals. Moreover Miocene deltaic sandstones (samples 11 AM 07 and 11 AM 08) are dominantly enriched in ZTR (≥70% of total heavy minerals assemblage; Fig. 2.6). Makran Miocene sandstones contain the same detrital zircon age populations (three main peaks at 167 Ma, 88.7 Ma and 48.9 Ma), as the Upper Cretaceous-Oligocene sandstones. Furthermore ε-$Hf_{(t)}$ data of Miocene detrital zircons is identical as that of the Upper Cretaceous-Oligocene sandstones (Fig. 2.13). These results suggest that the Eocene-Oligocene sedimentary rocks are first-cycle detritus, while Miocene sandstones are second-cycle presumably supplied from the erosional scree located to the north. All of these features point to due to reworking of Eocene-Oligocene sandstones (Fig. 2.7).

2.6 Conclusion

The present study evaluated the provenance of detrital material in Late Cretaceous to Miocene turbiditic and deltaic sandstones of the onshore Makran accretionary wedge in southeast Iran. Results yield protolith ages from Middle Jurassic to Eocene (167-48.4 Ma). The Middle Jurassic ε-$Hf_{(t)}$ values range from +2 to -13 and Upper Cretaceous-Eocene ε-$Hf_{(t)}$ values range between -17 and +14. The combined U-Pb ages and Hf isotope data indicate that the protolith rocks belonged to a Middle Jurassic intracontinental rift and a Late Cretaceous-Eocene continental arc. We cannot rule out contributions from sources within the Lut and Central Iran blocks for older zircons. Cr-spinel, blue amphibole and heavy minerals assemblages imply additional sediment sourcing from ophiolite and blueschists. Our analytical results refute opinions that the Makran detritus were supplied from Himalayan sources in a Palaeo-Indus submarine fan delta complex. Instead, the Upper Cretaceous-Oligocene erosional scree was presumably transported by two rivers and subsequent turbiditic flows in submarine fans from a nearby complex of continental arc and ophiolites to the north into the Makran Basin. Miocene detritus supplied from onshore Makran recycled Eocene-Oligocene sandstones.

2.7 Acknowledgements

This study was funded by the Swiss National Fond (grant no. 2-77644-09). The authors thank the Geological survey of Iran for efficient support during fieldwork. Thanks are due to Frowin Pirovino for his help on sandstone thin sections, Markus Wälle for his support on the Laser ablation ICP-MS, Karsten Kunze for his assistance for CL and BSC imaging. This work was financed by the grant no. 2-77644-09 from the Swiss National Fond.

Chapter III

Sistan Provenance

3. Detrital zircon and provenance analysis of Eocene-Oligocene strata in the South Sistan Suture Zone, SE Iran: implications on the tectonic setting

Ali Mohammadi, Jean-Pierre Burg, Wilfried Winkler

This chapter has been submitted to Earth and Planetary Science Letters

Abstract

The N-S-trending Sistan Suture Zone in east Iran results from the Paleogene collision of the Lut Block, to the west, with the Afghan Block, to the east, after subduction of a branch of the Tethys Ocean beneath the Afghan Block. This provenance study of Eocene-Oligocene deep marine turbiditic sandstones aims to document the tectonic context of the Sistan sedimentary basin and to provide critical constraints on the closure time of this part of Tethys. We report the analysis of the sandstone framework and a heavy mineral study including La-ICP-MS U-Pb ages and 415 Hf isotopic analyses of 3015 in-situ detrital zircons. Framework modes reveal magmatic arcs as main source of detritus. Heavy mineral assemblages and Cr-spinel disclose ophiolite as a subsidiary source. Two main detrital zircon ages are identified: 1) abundant Upper Cretaceous grains with Hf isotopic compositions of oceanic crust and depleted mantle, suggesting an intra-oceanic island arc provenance. 2) Eocene grains with Hf isotopic compositions of continental crust and non-depleted mantle, suggesting a transitional-continental magmatic arc provenance. This change in provenance is attributed to the Paleocene (65-55 Ma) collision between the Afghan plate and an intra-oceanic island arc not considered in previous tectonic reconstructions of this part of the Alpine-Himalayan orogenic system.

Key words: South Sistan, provenance analysis, detrital zircon, Hf isotopes, tectonic setting.

3.1 Introduction

The analysis of sandstone provenance contributes importantly to the understanding of past plate tectonics by providing valuable information on the compositions of source rocks and, consequently, the tectonic setting (e.g. Dickinson and Suczek, 1979; Dickinson, 1985; Zuffa, 1985). Sandstone framework analysis and heavy minerals studies are the main and classical tools of provenance analysis (e.g. Weltje and von Eynatten, 2004). Among heavy minerals, zircon plays an important role because it is mechanically and chemically resistant in depositional and weathering environments (DeCelles et al., 2007; Gehrels et al., 2011) and zircon U-Pb geochronology reliably determines ages of individual detrital grains (e.g. Košler et al., 2002;

Veiga-Pires et al., 2009). Measurement of the Hf isotope in dated zircon grains further enables characterizing the isotopic composition of the magma in which the zircons crystallized (e.g. Sláma et al., 2008).

It has been suggested that Paleogene sediments of Makran and adjacent basins were supplied from the Himalaya by the Paleo-Indus River and deposited in a delta-submarine fan complex, whereas Miocene to recent deposits were reworked from the growing accretionary wedge (e.g. Critelli et al., 1990; Qayyum et al., 2001; Kassi et al., 2013). Carter et al. (2010) reached the same conclusion from the provenance analysis of Eocene-Oligocene sandstones of the South Sistan basin.

The present work aims to contribute to the knowledge of the Mesozoic and Cenozoic geological history of the South Sistan basin, in eastern Iran (Fig. 3.1) by investigating the provenance of siliciclastic sandstones. We combine results from fieldwork, modal framework grain compositions and heavy mineral analysis to characterize the lithologies existing in the source areas and constrain the tectonic setting and evolution of the Sistan area. 3015 U-Pb ages of detrital zircon obtained by ICP-MS laser ablation are used to evaluate crystallization age ranges in the source area. Hf isotope ratios of 403 dated zircons grains are used to infer the origin of magmas in the source region. Our results firmly establish that the detrital materials in the South Sistan basin derive from a Late Cretaceous oceanic island arc and an Eocene-Oligocene transitional-continental arc. Ophiolites contributed to clastic heavy minerals. These sources are tentatively related to equivalents of the Rakosh-Chagai arcs and ophiolites in the neighbouring western Pakistan.

3.2 Geological Setting

The NNW-SSE-trending Sistan Suture Zone (SSZ) in east Iran separates the continental Lut sub-block of Central Iran, in the west, from the Afghan Block, to the east (e.g. Şengör, 1990b; Fig. 3.1). The Sistan Ocean was a branch of the Tethys Ocean that closed in the Late Eocene (Tirrul et al., 1983). The SSZ consists of three tectonostratigraphic complexes separated by thrust faults (Camp and Griffis, 1982; Tirrul et al., 1983; Fig. 3.1). The Ratuk Complex, to the east, was formed prior to Maastrichtian time. It comprises Cretaceous ophiolitic mélanges, metamorphic rocks including eclogites, blueschists and epidote amphibolites and sedimentary rocks including lower Cretaceous limestone, upper Cretaceous turbiditic sandstones, Eocene nummulitic limestones and Neogene conglomerates (e.g. Tirrul et al., 1983; Bröcker et al., 2013). The Neh Complex, to the west, consists of Upper Cretaceous shallow water limestone, Eocene-Oligocene deep marine turbiditic sandstones and Eocene-Oligocene intrusions (Camp and Griffis, 1982; Tirrul et al., 1983). The Sefidabeh forearc Complex, in between, unconformably covers both the Neh and Ratuk complexes. It comprises an 8 km thick, essentially clastic sequence of Cenomanian to

Eocene sedimentary rocks including both deep and shallow marine limestones and calc-alkaline volcanic intercalations on the eastern side (Tirrul et al., 1983).

The study area is located in the southern part of the SSZ, in the Neh Complex (Fig. 3.1). It is covered by the Narreh-Now, Saravan, Pishin, Khash, Iranshahr and Nikshahr 1:250,000 geological maps (Morgen et al., 1979; Samimi Namin et al., 1986; Eftekhar Nezhad and McCall, 1993; Samimi Namin et al., 1994; Eftekhar Nezhad et al., 1995; Sahandi et al., 1996). Some authors interpret the southern Neh Complex as a transitional zone between the Sistan and Makran basins (e.g. McCall, 2002; Carter et al., 2010). The area is principally comprised of Eocene and Oligocene deep marine turbidites (presence of e.g. Paleodictyon and Spirorhaphe involute ichnofossils (Crimes and McCall, 1995; Shabani Goraji, 2015; Fig. 3.3) and their very low grade equivalents Fig. 3.2).

These turbiditic sequences were subdivided into 9 lithostratigraphic units, which are typically several hundred meters thick and dominated by Bouma-type turbiditic sandstones and shales (Morgen et al., 1979; Samimi Namin et al., 1986; Eftekhar Nezhad and McCall, 1993; Samimi Namin et al., 1994; Eftekhar Nezhad et al., 1995; Sahandi et al., 1996; Fig. 3.4). Most sandstones are feldspathic litharenite and lithic arkose and contain assemblages of planktonic and benthic foraminifera and nannofossils (Table 3.1; McCall, 1985).

3.3 Methods

Twenty medium-grained turbiditic sandstones (with prefix 12 AM and 13 AM in the ETH collection) from five lithostratigraphic units of the Neh Complex have been investigated (Fig. 3.2; 3.4; Table. 3.2). Pelagic nannofossils confirmed the mapped stratigraphy, yielding sedimentation ages ranging from Eocene to Oligocene (Carla Müller, personal communication; Table. 3.1). We combined sandstone framework, heavy mineral study, detrital zircon U-Pb ages and Hf-isotopic ratios of dated zircons to reconstruct the composition of the source-rock and the tectonic evolution of the source area. Analytical methods including separation, identification and quantification techniques are described in Appendix B.

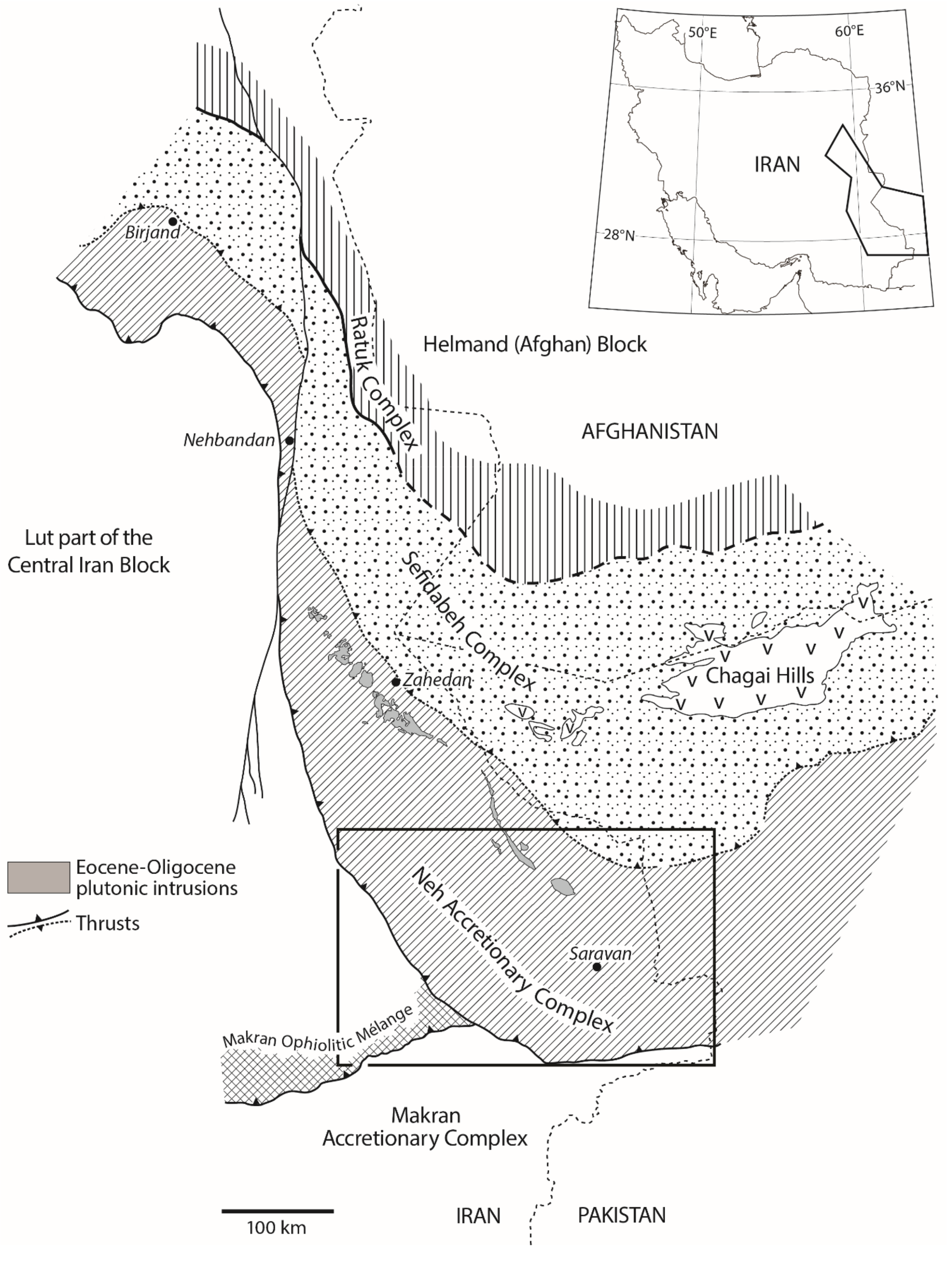

Figure 3.1: Major geological subdivisions of the Sistan Suture zone adapted from Tirrul et al. (1983). Framed: studied area.

Table 3.1. Geographical location (degree, minute, second), ages and characteristics of the analyzed samples of the Sistan sandstones.

Sample No:	**Latitude N deg min sec**	**Longitude E deg min sec**	**Stratigraphic age**	**Stratigraphic age**	**Lithology / inferred depositional environment**	**MFA**	**HM**	**DZA**
12 AM 94	27 04 05	61 21 12	Oligocene	Chattian	Fine grained turbidity sandstone with flute cast and load cast	MFA		
12 AM 97	26 55 02	61 36 02	Oligocene	Chattian	Medium grained turbidity sandstone with cross-bedding	MFA	HM	
12 AM105	27 04 21	61 22 48	Oligocene	Chattian	Fine grained turbidity sandstone alternation with shale, bioturbation	MFA	HM	
12 AM 123	27 31 00	62 22 35	Eocene	Ypresian - Bartonian	Fine grained sandstone in imbricate zone	MFA	HM	DZA
12 AM 124	27 25 19	62 10 23	Eocene	Lutetian - Bartonian	Medium grained turbidity sandstone with ripple mark	MFA	HM	DZA
12 AM 134	27 35 26	60 40 29	Oligocene	Rupelian	Fine grained turbidity sandstone with ripple mark	MFA	HM	DZA
12 AM 135	27 38 01	62 32 05	Eocene	Ypresian - Bartonian	Thick bedded, medium to coarse grained massive turbidity sandstone	MFA	HM	DZA
13 AM 157	27 59 32	61 17 23	Eocene	Ypresian - Rupelian	Coarse grained sandstone with through cross-bedding	MFA	HM	DZA
13 AM 166	27 49 31	61 15 44	Eocene	Ypresian - Rupelian	Medium grained turbidity sandstone with flute cast	MFA	HM	DZA
13 AM 186	28 10 34	61 27 18	Eocene	Ypresian - Priabonian	Medium to coarse grained sandstone with through cross-bedding, deltaic	MFA	HM	DZA
13 AM 206	28 12 48	61 35 52	Eocene	Ypresian - Bartonian	Coarse grained sandstone with through cross-bedding, deltaic	MFA	HM	DZA
13 AM 218	27 33 59	62 01 27	Eocene	Ypresian - Lutetian	Coarse grained sandstone with flute cast, bioturbation, deltaic	MFA	HM	DZA
13 AM 224	27 41 10	61 51 05	Eocene	Ypresian - Lutetian	Medium grained sandstone with cross-bedding, shelf environment	MFA	HM	DZA
13 AM 237	27 47 37	61 57 41	Eocene	Ypresian - Bartonian	Fine grained turbidity sandstone, alternated with bioturbated shale	MFA	HM	DZA
13 AM 246	27 17 36	62 32 25	Eocene	Ypresian - Bartonian	Medium grained turbidity sandstone with ripple mark and bioturbation	MFA	HM	DZA
13 AM 252	26 58 27	62 32 13	Eocene - Oligocene	Pirabonian - Rupelian	Medium grained turbidity sandstone with ripple mark	MFA	HM	DZA
13 AM 260	26 45 59	62 40 30	Eocene - Oligocene	Pirabonian - Rupelian	Fine grained turbidity sandstone with flute cast and load cast		HM	DZA
13 AM 263	27 16 21	62 28 51	Eocene	Pirabonian	Medium grained turbidity sandstone with cross-bedding	MFA	HM	DZA
13 AM 280	27 10 42	62 16 42	Eocene - Oligocene	Pirabonian - Rupelian	Fine grained turbidity sandstone	MFA	HM	DZA
13 AM 293	27 11 02	61 43 12	Eocene	Ypresian - Bartonian	Fine grained turbidity sandstone, alternated with bioturbated shale	MFA	HM	DZA

Analysis key: MFA: modal framework analysis, HM: heavy minerals, DZA: detrital zircon age and Hafnium isotopes.

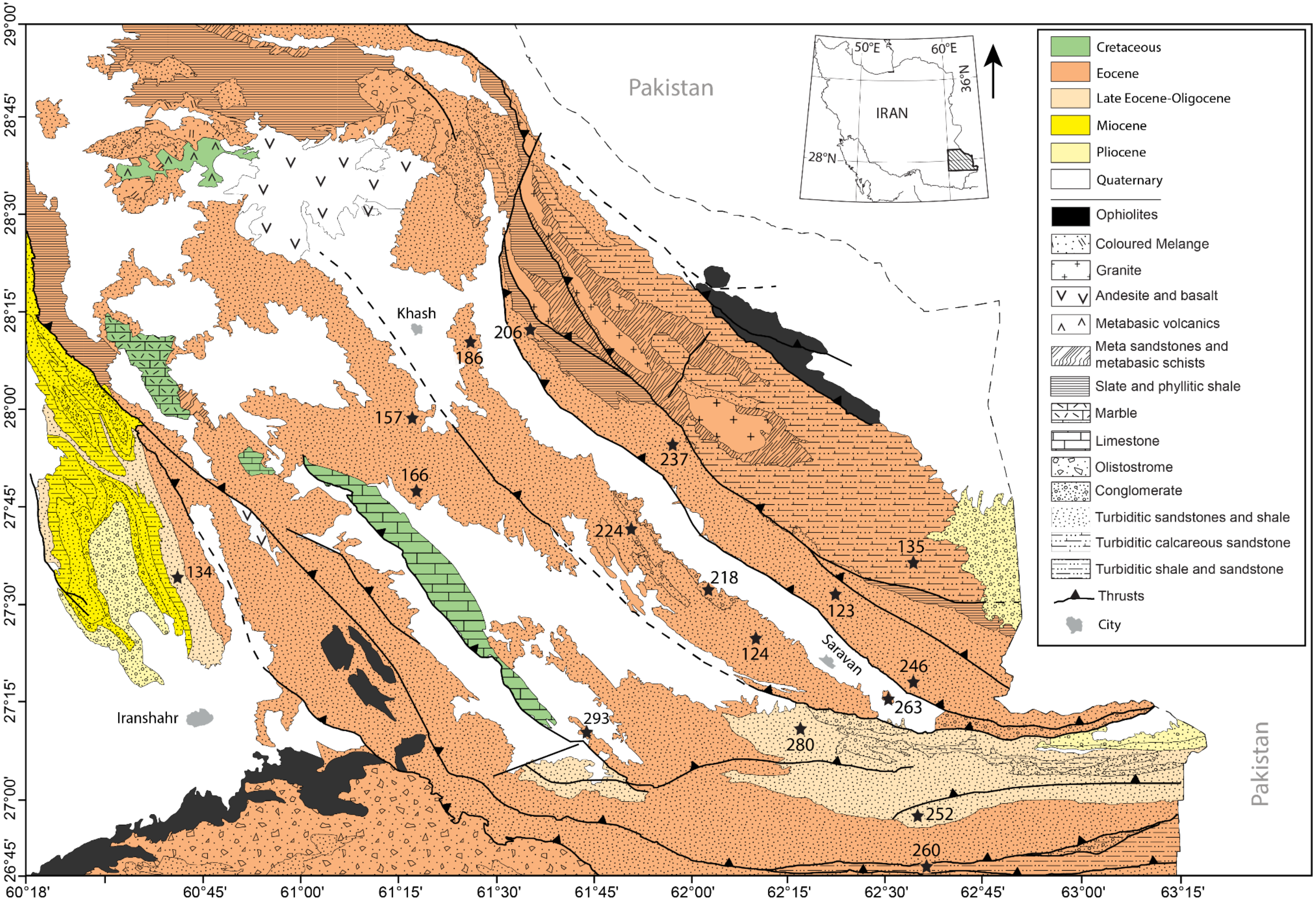

Figure 3.2: Simplified geologic map of the South Sistan Basin. Stratigraphic ages according to the 1:250,000 geological maps of Pishin, Narre-Now, Saravan, khash, Iranshahr and Makran (Samimi Namin et al., 1986; Eftekhar Nezhad and McCall, 1993; Samimi Namin et al., 1994; Eftekhar Nezhad et al., 1995; Sahandi et al., 1996; Dolati, 2010).

Table 3.2 Geographical location (degree, minute, second), lithology, nannofosils and ages of the analyzed samples of the Neh Complex in south Sistan. Nannofossils and ages were determined by Carla Müller.

Sample No:	Latitude deg: min: sec	Longitude deg: min: sec	Rock type	Nannofossils	Age
13 AM 182	27 54 39.3	61 31 53.3	shale	Coccolithus pelagicus, Coccolithus eopelagicus, Discoaster barbadiensis, Discoaster saipanensis, Cribosphaera reticulate, Reticulofenestra umbilica, Cyclococcolithus formosus, Sphenolithus moriformis	Upper Eocene
13 AM 223	27 40 40.7	61 50 26.0	shale	Coccolithus pelagicus, Reticulofenestra pseudoumbilica, Sphenolithus abies, Sphenolithus belemnos, Sphenolithus procerus, Helicosphaera carteri, Discoaster deflandrei, Cyclococcolithus leptoporus, cyclicargolithus floridanus	Lower Oligocene
13 AM 277	27 14 10.5	62 10 54.7	shale	Coccolithus pelagicus, Coccolithus eopelagicus, Discoaster barbadiensis, Discoaster saipanensis, Cribosphaera reticulate	Upper Eocene

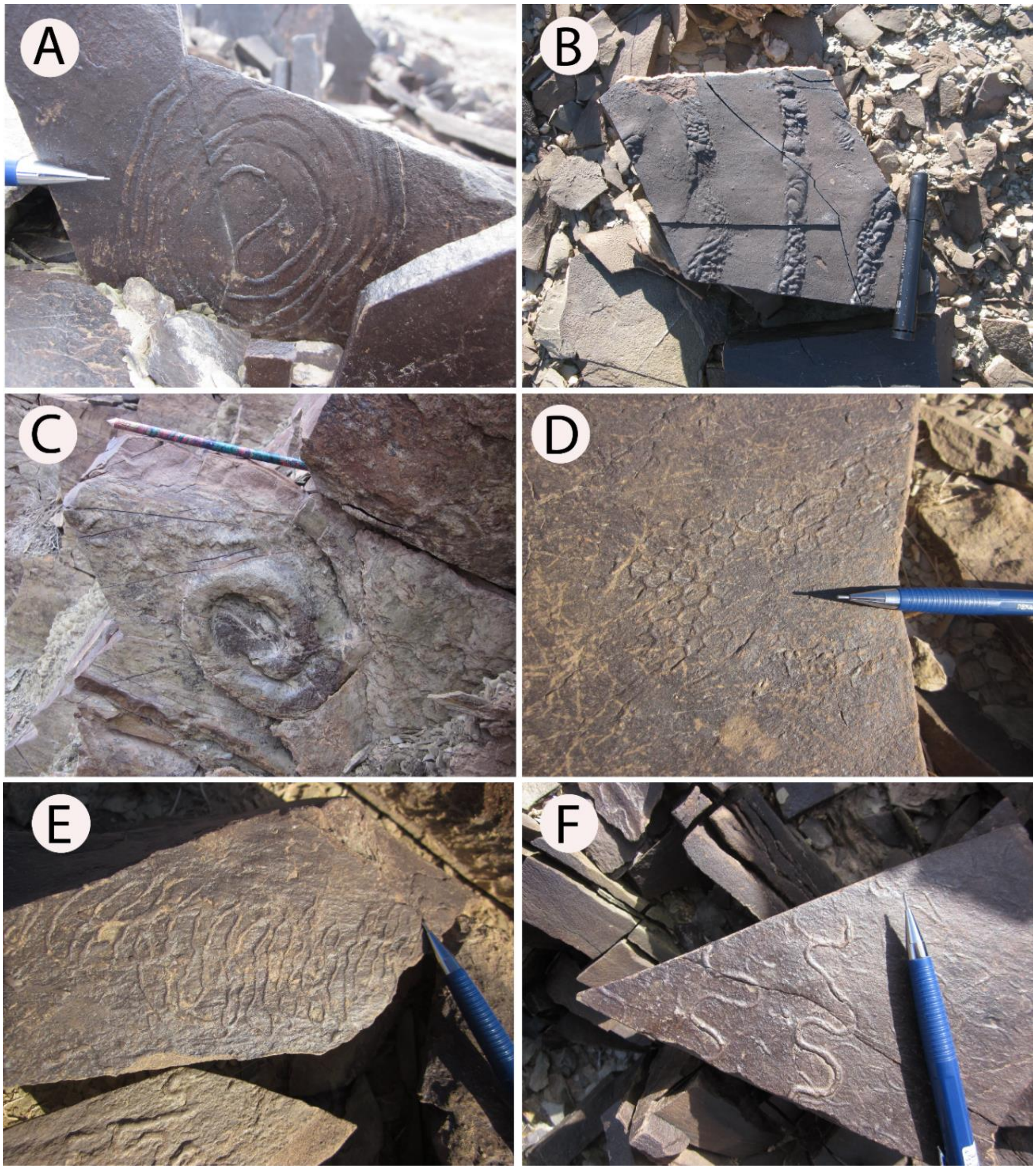

Figure 3.3: Trace fossils of Eocene deep marine turbidites of Neh complex: (A) Spirorhaphe involute, (B) Nereiles jacksoni, (C) Taphrhelmintopsis auricularis Sacco, (D) Paleodictyon carpathicum, (E) Helminthoida crassa, (F) Helminthoida ichnosp.

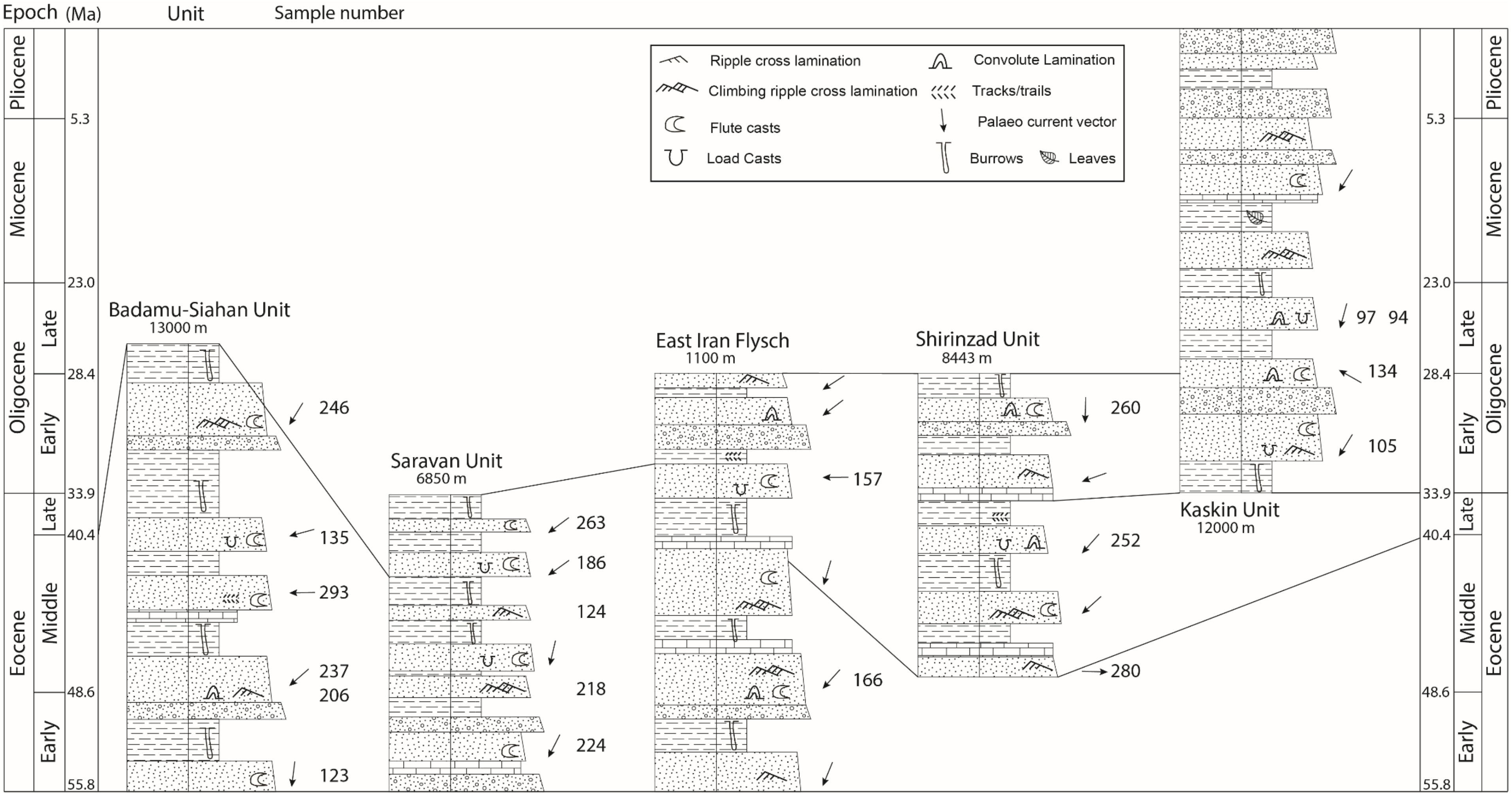

Figure 3.4: Composite stratigraphic section of the South Sistan Basin with paleocurrent directions and sampling points. Badamu-Siahan unit is equivalent to the Zaboli unit in the 1:250,000 geological map of Saravan and to the Kuh-e Badamo unit in the 1:250,000 geological map of Narreh-Now. The Saravan unit is equivalent to the East Iran Flysch unit in the 1:250,000 geological map of Khash. The Shirinzad unit is equivalent to the Mashkid unit in the 1:250,000 geological map of Saravan and the Kaskin unit is equivalent to the Rask unit in the 1:250,000 geological map of Pishin. All cited maps published by the geological Survey of Iran.

3.4 Results

3.4.1 Paleocurrents

Paleocurrent directions were measured from 53 flute casts and 3 asymmetric ripple marks. Readings were rotated to horizontal around the local strike direction of bedding. Measurements indicate a regional NE to SW paleoslope with a source area to the northeast of the basin (Fig. 3.5).

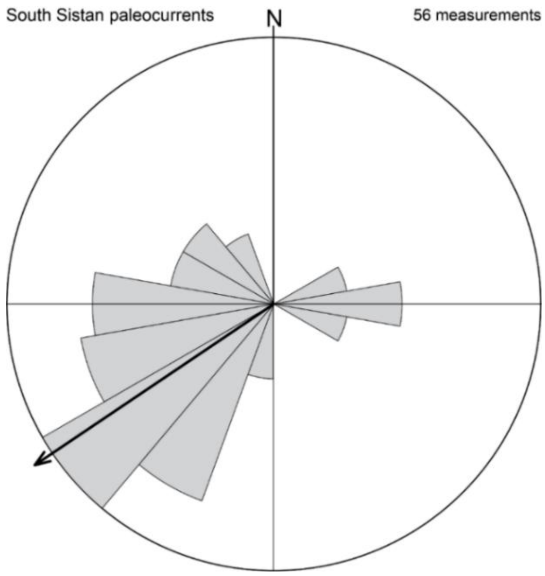

Figure 3.5: Rose diagram of paleocurrent measurements from 53 flute cast and 3 asymmetric ripple marks restored to horizontal around the local strike of bedding. Arrow: average direction.

3.4.2 Modal Framework

Thin sections were stained for feldspars and carbonates and tested with the Gazzi-Dickinson method for modal framework grain analysis (Norman, 1974). More than 300 detrital grains were counted in each thin section for statistical reliability (Folk, 1980). The Zuffa method has been applied to count lithic fragments (Zuffa, 1985). Minerals larger than 0.063 mm within rock fragments were counted as monomineralic grains. Results were converted to percentages for compositional comparison (Weltje and von Eynatten, 2004).

The studied sandstones classify mainly as lithic arkose and feldspathic litharenite (Fig. 3.6a). Quartz grains are mostly mono-crystalline (82%) and feldspar is dominantly plagioclase (> 91%) with minor amounts of K-feldspar (Fig. 3.6b). Lithic fragments are represented by sedimentary, volcanic and metamorphic grains (Figs. 3.6c, d). Volcanic rock fragments are mostly andesite and volcanic glass. Sedimentary lithic fragments include mainly siltstone and limestone. Metamorphic lithic grains generally consist of low-grade to medium-grade phyllites and schists. The sources plot mostly in the recycled orogenic field (Fig. 3.6e), more precisely in the field of dissected arcs (Fig. 3.6f).

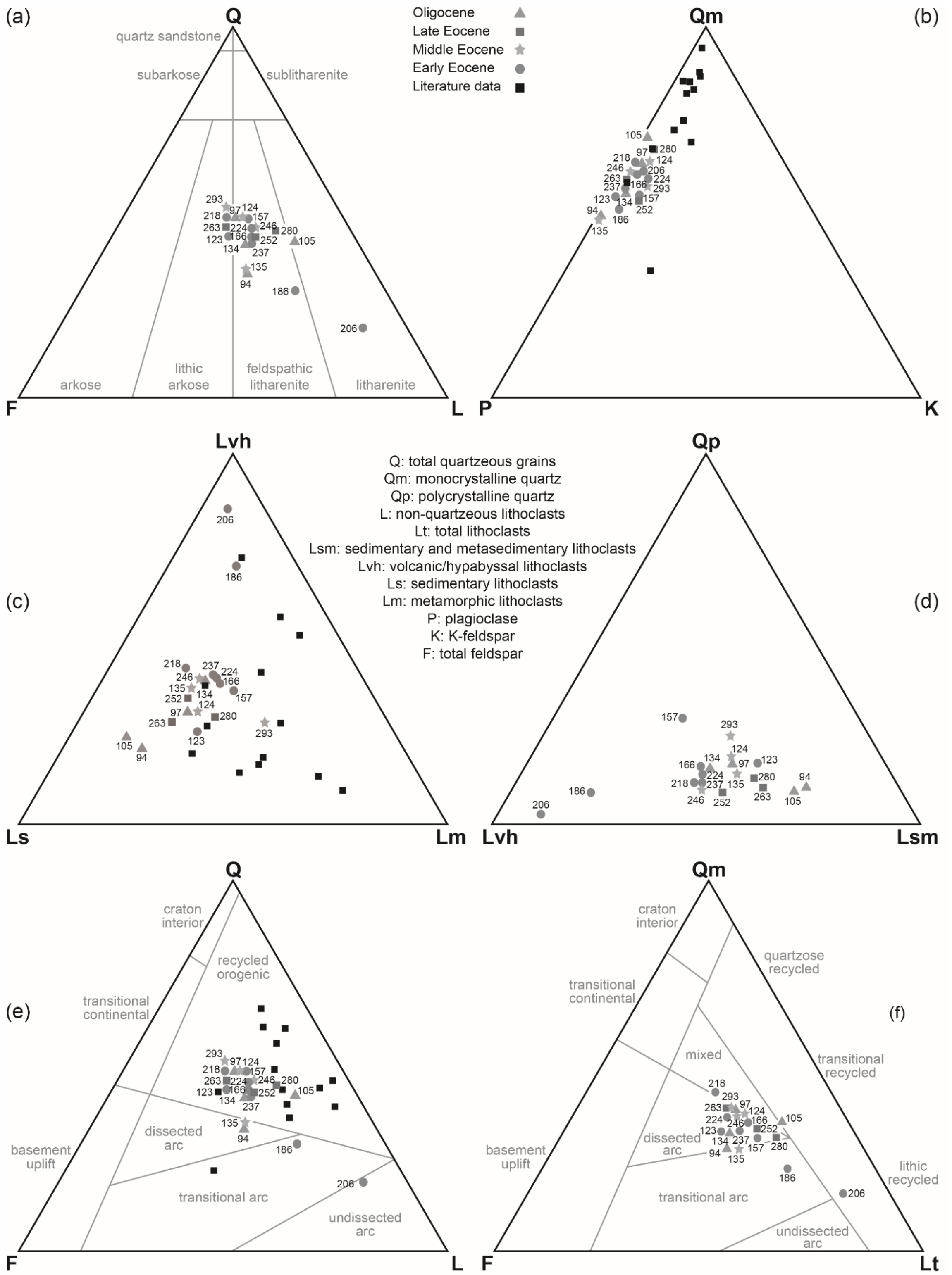

Figure 3.6: Detrital composition and classification of South Sistan sandstones in provenance discrimination diagrams: (a) sandstone classification diagram Folk (1980); (b) Qm-P-K diagram after Dickinson and Suczek (1979); (c) Lvh-Ls-Lm diagram after Dickinson (1985); (d) Qp-Lvh-Lsm diagram after Dickinson and Suczek (1979); (e) QFL Dickinson (1985) and (f) QmFLt Dickinson (1985). Literature data on Makran basin from Carter et al. (2010).

3.4.3 Heavy minerals

Heavy mineral suites show very variable compositions subdivided into four groups: (1) ultra-stable minerals (zircon, tourmaline, rutile, monazite, brookite, anatase and sphene; ZTR= 7-67%) and apatite derived from continental crust sources. (2) Variably abundant (4 to 70% of 200 counted grains) metastable minerals (epidotes, garnet, staurolite, chloritoid, kyanite, andalusite) pointing out different detrital sources of medium-grade metamorphic rocks and garnet-bearing granitoids. (3) Cr-spinel (up to 20% of total grain count) indicating locally important contribution from exhumed ophiolites. (4) Pyroxenes (diopside, enstatite, ferrosilite and hedenbergite) from basic to intermediate magmatic rocks (Fig. 3.7).

Early-Middle Eocene sandstones (samples 123, 157, 186 and 237) generally show large amounts (up to 80% of total grain count) of epidote and pyroxene groups. Oligocene sandstones (samples 97 and 105) yielded large amounts (up to 87% of total grain count) of garnet, epidote and pyroxene groups (Fig. 3.7). The negative trend of the garnet-zircon index (GZi) with sandstone age indicates that the proportion of metastable grains in the heavy mineral assemblage decreases with time. This implies that the heavy mineral content is partly controlled by burial diagenesis (Morton and Hallsworth, 1999; Fig. 3.8).

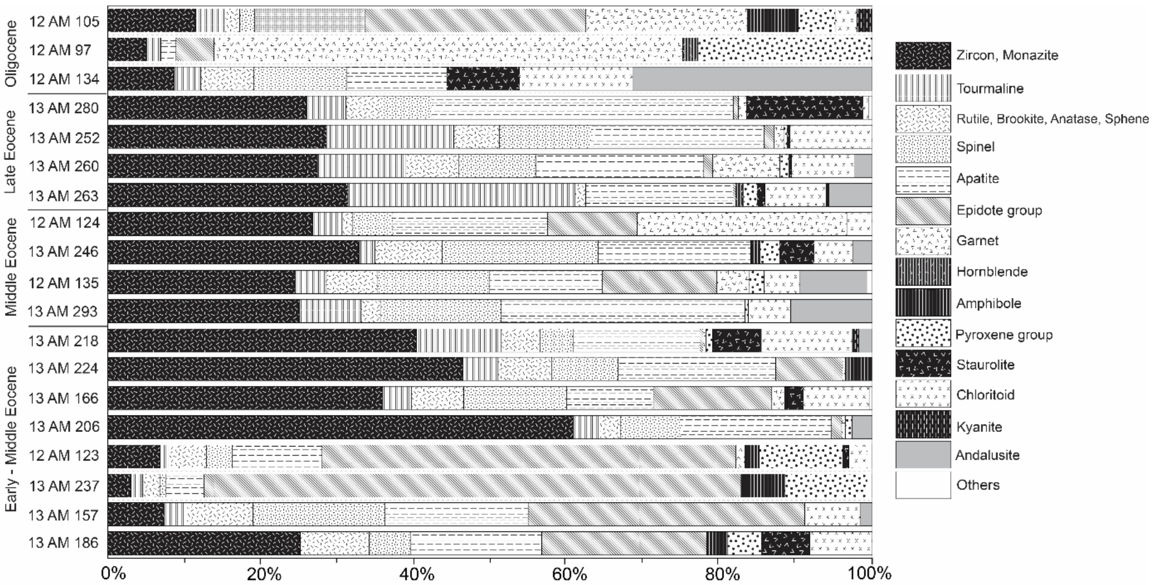

Figure 3.7: Heavy mineral assemblages of the South Sistan sandstones arranged in reconstructed stratigraphical order and showing the relative abundance of heavy mineral species.

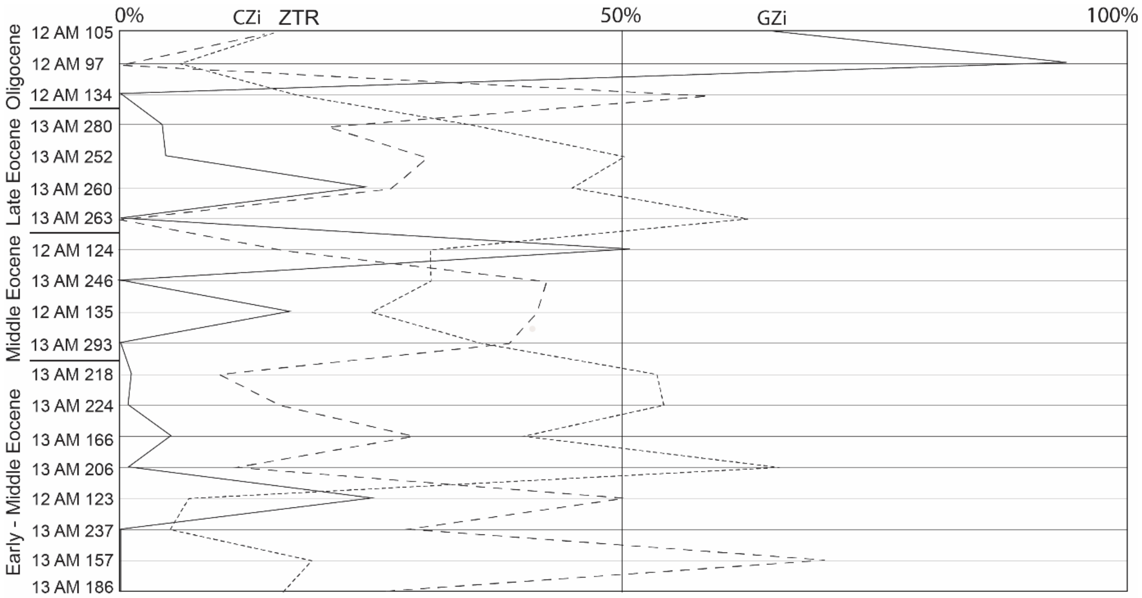

Figure 3.8: Provenance-sensitive heavy minerals index ratios (Morton and Hallsworth, 1999) calculated for the South Sistan sandstones. GZi = [garnet / (garnet + zircon)]×100; CZi = [chromian spinel / (chromian spinel + zircon)]×100; ZTR = zircon + tourmaline + rutile.

3.4.4 Detrital zircon dating and Hf isotope geochemistry

Most detrital zircon crystals (85%) are euhedral to anhedral, suggesting short transport distances from source to sink. U-Pb dating of detrital zircons was done on 17 Eocene-Oligocene sandstone samples (Figs. 3.9; 3.10; 3.11; 3.12). Only concordant ages were used. Zircon ages older than 1100 Ma were not plotted due to their rarity. Cretaceous and Eocene ages prevail with Cretaceous peaks at 106, 89, and 68 Ma and an Eocene peak at 49.5 Ma (Figs. 3.9; 3.10; 3.11; 3.12). The lack of lag time (Eocene zircons hosted in sandstone of similar stratigraphic age) indicates syn-sedimentary magmatism in the source area (Fig. 3.13).

Depending on the size of zircon grains and their texture (internal growth structure and inclusions imaged by cathodoluminescence and backscattered-electron imaging), Hf isotope ratios were measured on dated zircons (Woodhead et al., 2004). The evolved epsilon hafnium (ε-Hf$_{(t)}$) data from zircons older than 600 Ma are not shown in Figure 14. Upper Cretaceous ε-Hf$_{(t)}$ ranges from +33 to -17 (Fig. 3.14). Positive ε-Hf$_{(t)}$ suggest a mixed oceanic crust - depleted mantle origin as for oceanic island arc-related magmatism; negative ε-Hf$_{(t)}$ denote melting of subducted sediment (e.g. Salters and Hart, 1991; Hofmann, 1997). Zircons with Eocene ages have □-Hf$_{(t)}$ values between +26 and -15 , few above the depleted mantle line. Compared to the Upper Cretaceous zircons, Eocene zircons show more negative and less positive ε-Hf$_{(t)}$ between the (CHUR) and depleted mantle lines (Fig. 3.14). Negative ε-Hf$_{(t)}$ indicate magmatic zircons with continental crust signature whereas the positive ε-Hf$_{(t)}$ values indicate oceanic crust or non-depleted mantle signatures as for subduction-related magmatism in continental arcs (e.g. Patchett, 1983; Naing et al., 2014).

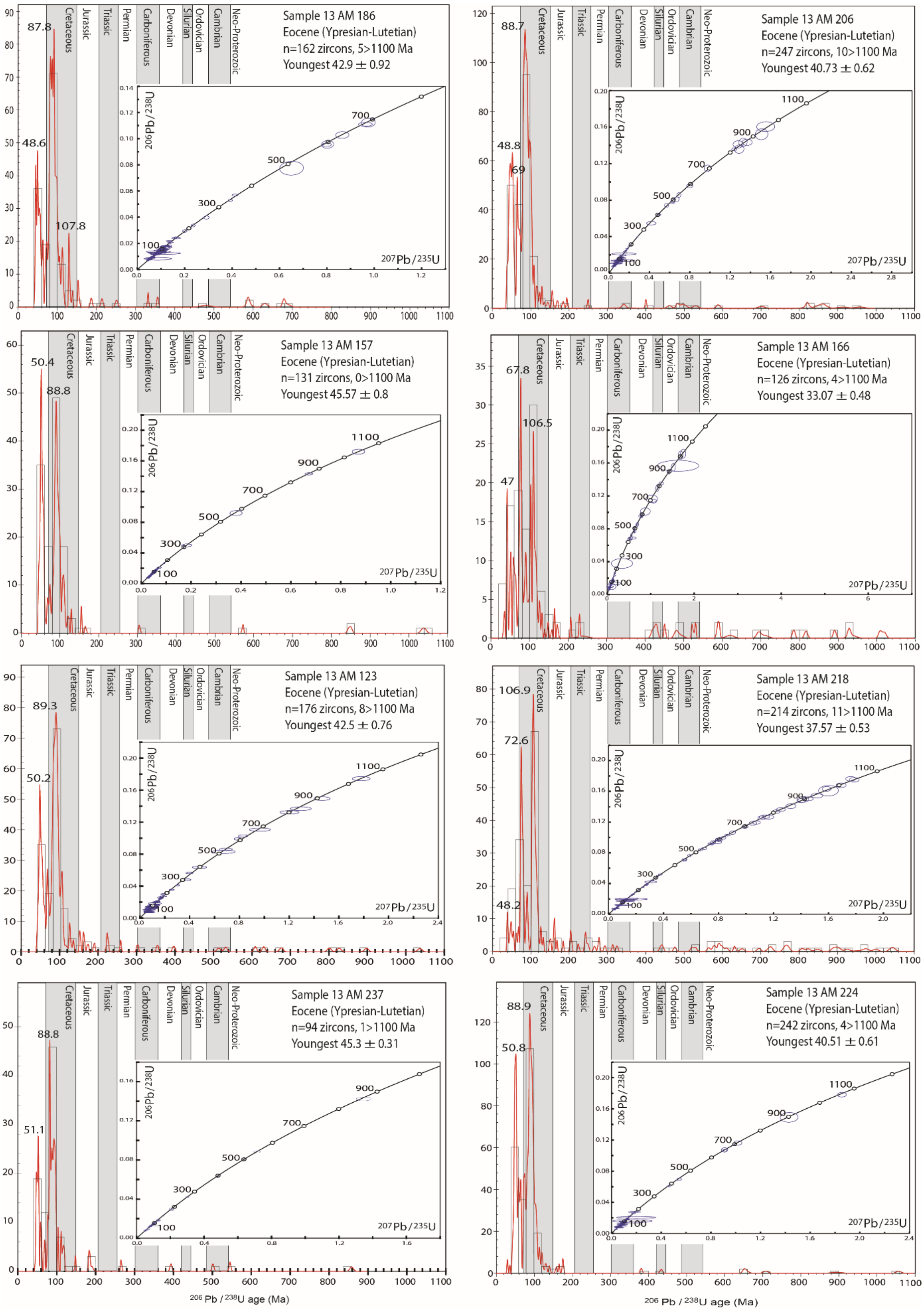

Figure 3.9: Probability density diagrams for detrital zircon $^{206}Pb/^{238}U$ age populations with corresponding Concordia plots of concordant detrital zircons of the samples 186, 206, 157, 166, 123, 218, 237 and 224 from South Sistan sandstones. Ages with discordance greater than 5% are not included. Time scale after Gradstein et al. (2012) .

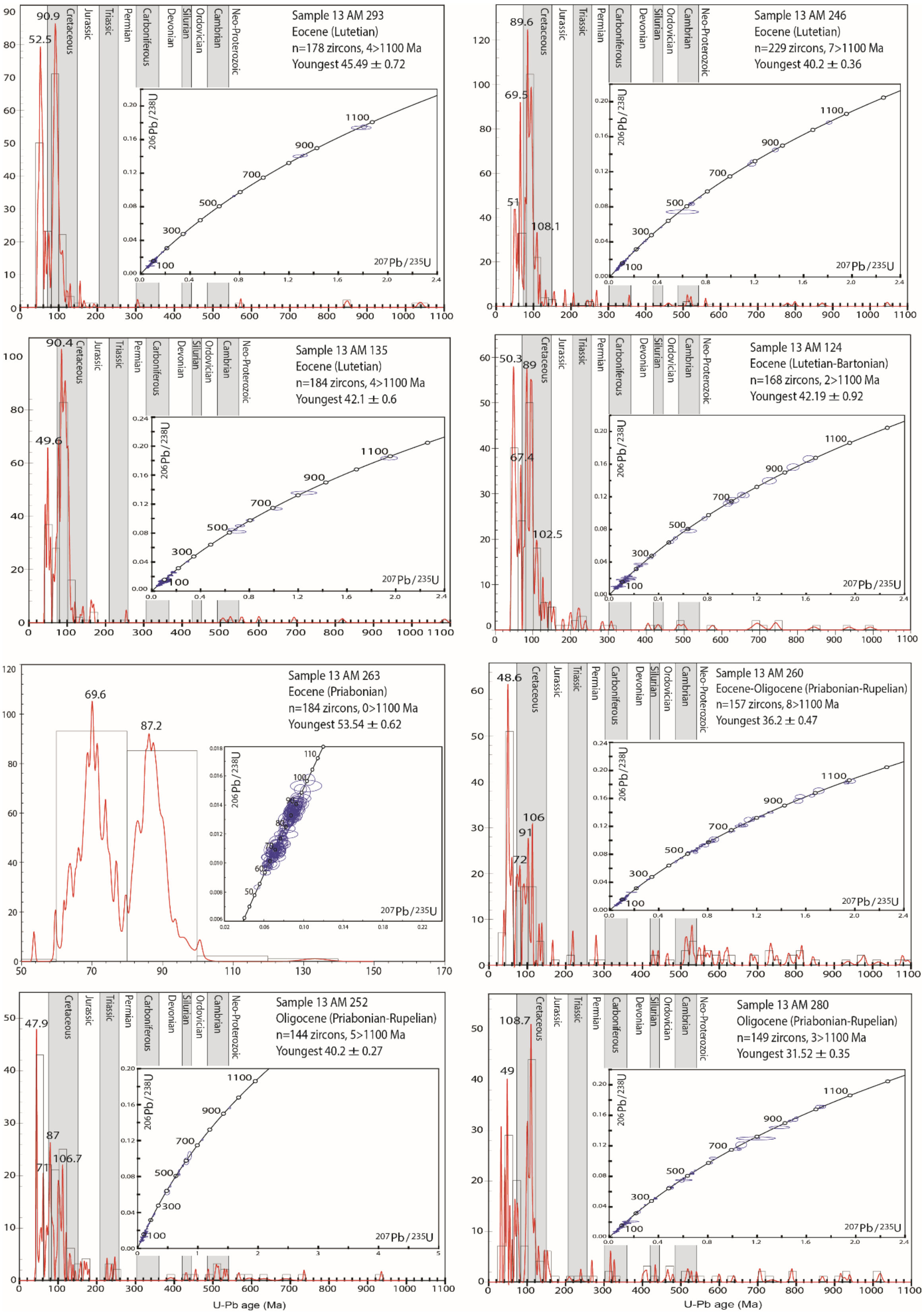

Figure 3.10: Probability density diagrams for detrital zircon $^{206}Pb/^{238}U$ age populations with corresponding Concordia plots of concordant detrital zircons of the samples 293, 246, 135, 124, 263, 260, 252 and 280 from South Sistan sandstones. Ages with discordance greater than 5% are not included. Time scale after Gradstein et al. (2012).

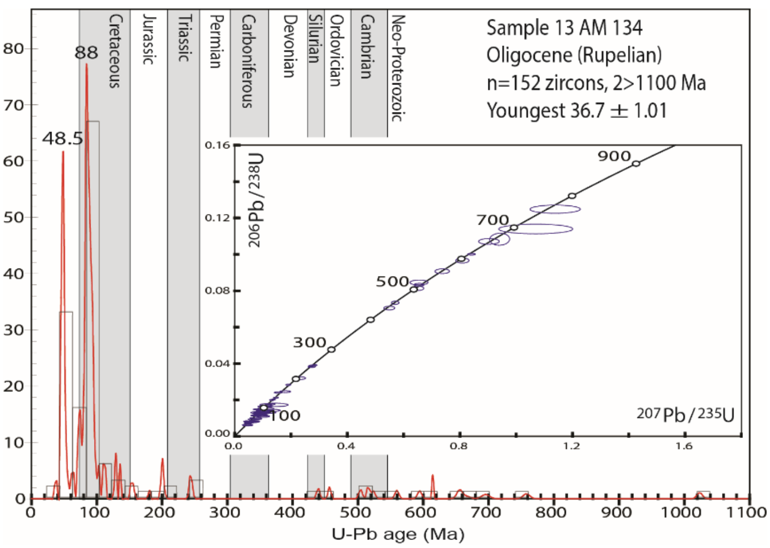

Figure 3.11: Probability density diagrams for detrital zircon $^{206}Pb/^{238}U$ age populations with corresponding Concordia plots of concordant detrital zircons of the sample 134 from South Sistan sandstones. Ages with discordance greater than 5% are not included. Time scale after Gradstein et al. (2012).

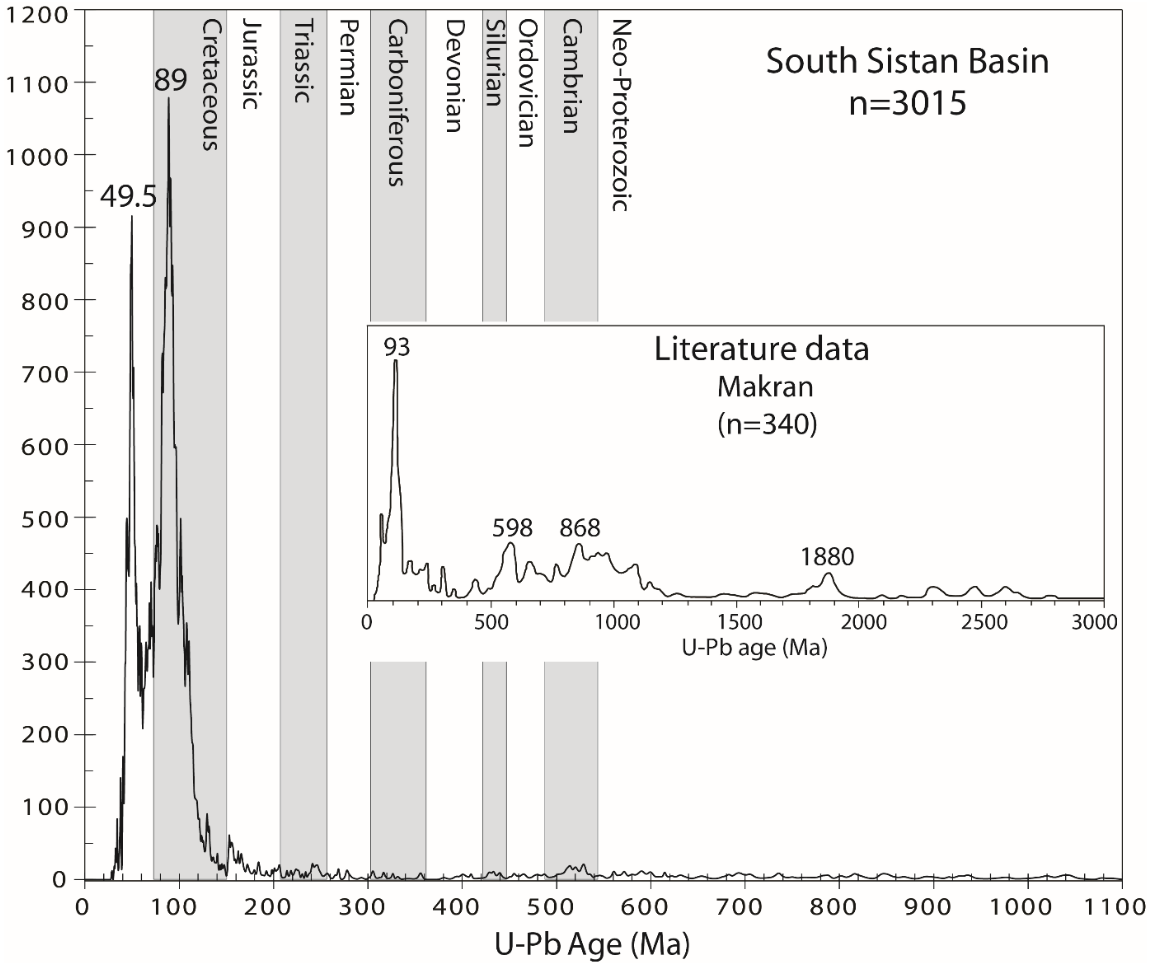

Figure 3.12: U-Pb age distribution pattern of all sandstone samples from the South Sistan Basin. Time scale after Gradstein et al. (2012). Literature data of Makran Basin from Carter et al. (2010).

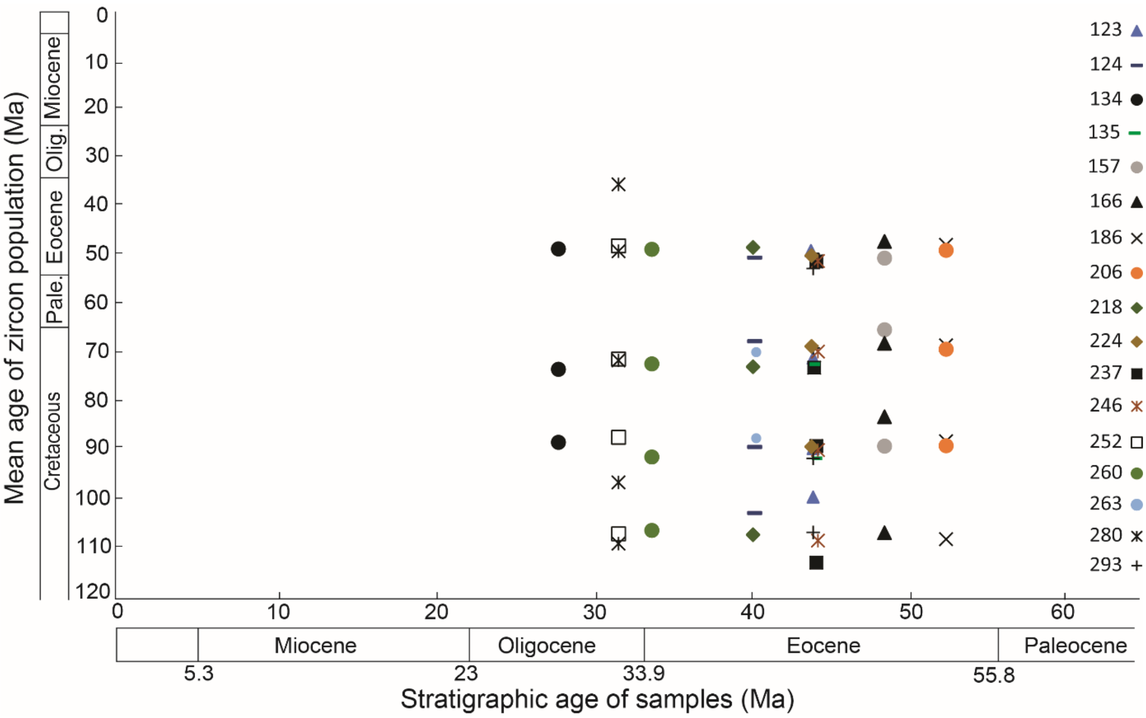

Figure 3.13: Zircon mean age populations versus stratigraphic age of sandstone samples. Time scale after Gradstein et al. (2012).

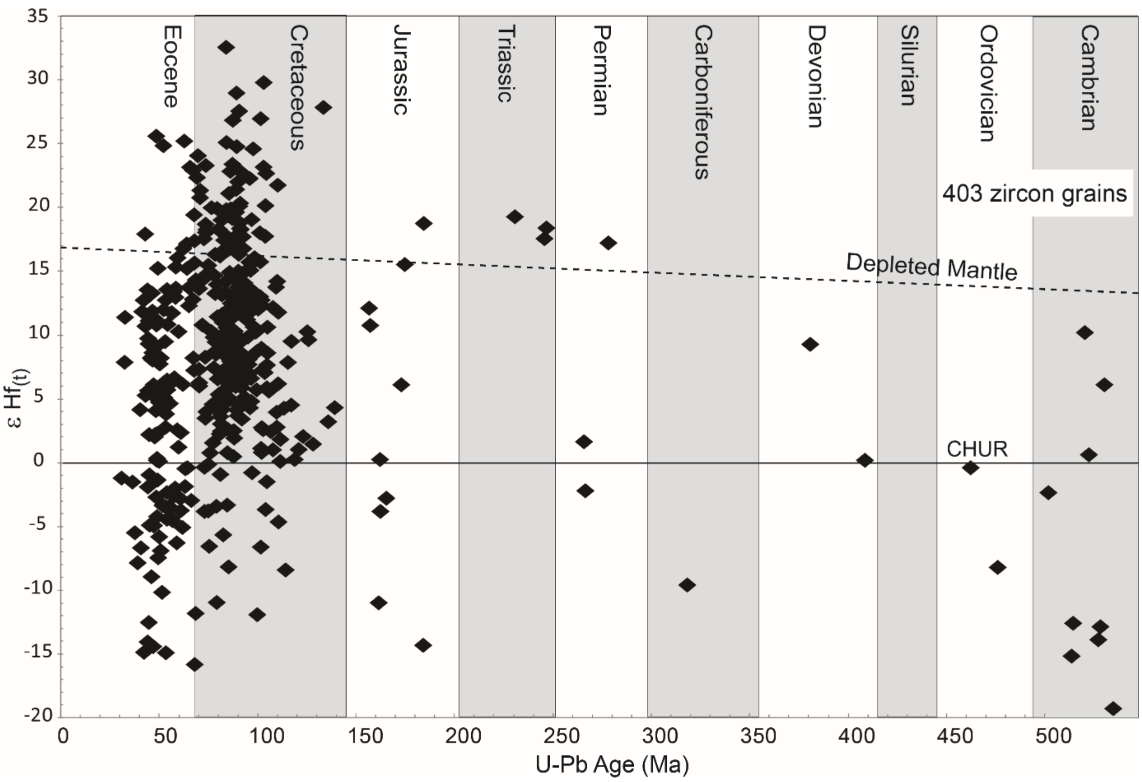

Figure 3.14: Time-corrected ε-Hf$_{(t)}$ values versus $^{206}U/^{238}Pb$ zircon ages (Ma) of the South Sistan sandstones. Age correction based on chondritic values (CHUR) from Blichert-Toft and Albarède (1997). Depleted Mantle evolution trend (dashed line) from Griffin et al. (2000). Time scale after Gradstein et al. (2012).

3.5 Discussion

This combined U-Pb geochronology and Hf isotope provenance study for Eocene-Oligocene sandstones of the South Sistan Suture Zone allows refining evolutionary models of this part of the Asian Tethyan sutures.

3.5.1 Provenance of the detrital zircons

The heavy mineral spectrum implies that the Eocene-Oligocene lithic-rich arkoses and feldspathic litharenites of South Sistan collected detritus from magmatic arcs and ophiolites. Metamorphic minerals such as andalusite, kyanite, staurolite and chloritoid in heavy minerals assemblages represent metamorphic sedimentary rocks as subsidiary sources (Deer et al., 1992).

The 3015 detrital zircon grains analyzed from the Eocene-Oligocene turbiditic sandstones yielded apparent ages ranging from ca. 30.9 Ma to ca. 3.3 Ga (Figs. 3.9; 3.10; 3.11; 3.12). Three U-Pb age populations broadly characterize the South Sistan detrital zircon grains.

The oldest population, represented by ≤ 5% of studied grains, dates from Jurassic (200 Ma) to Archean (3.3 Ga). The rounded and anhedral shape of these grains without internal texture (growth zoning) suggests that they are fragments of old zircons reworked from continental crystalline rocks. The origin of these rare old grains is debatable. Possible igneous/metamorphic source areas could be anywhere after repeated reworking through several tectonic cycles since the Archean. Restricting conjecture to the closest blocks, in agreement with other euhedral grains indicating proximal source regions, leaves the Lut and the Afghan Blocks in the northwestern and northeastern margin of the South Sistan Basin, respectively. The southwestward paleocurrent directions favour derivation from the Afghan Blocks.

The second population includes detrital zircons of Late Early Cretaceous - Late Cretaceous age (115-70 Ma with main peak at 89 Ma). The euhedral shape and magmatic zoning of most grains (>85%) suggest that they were derived from not far-distant Upper Early Cretaceous - Late Cretaceous magmatic/volcanic rocks. ε-$Hf_{(t)}$ in this group point to mixed oceanic crust and mantle magma source rocks, likely in an intra-oceanic island arc. This information and southwestward paleocurrent directions would fit the Kohistan-Ladakh arcs but also the closer Chaghai-Raskoh arc (e.g. Perelló et al., 2008; Burg, 2011; Richards et al., 2012), on the Pakistan-Afghanistan border (Fig. 3.1)

The third and youngest detrital zircon age population (49.5 - 36 Ma with peak at 49.5 Ma) also displays euhedral shapes (>85%) and magmatic zoning and Hf isotopic ratios of mixed mantle and continental crust compositions, likely in a transitional-continental magmatic arc. A similar evolution at the same time is reported for the Chagai-Raskoh arc (Richards et al., 2012), where K-Ar and Ar-Ar ages show peaks at 87 Ma (Late Cretaceous), 55 Ma, 49 Ma and 45 Ma (Perelló et al., 2008). Therefore, we suggest that this arc and its westward continuation, along with the associated Late-Middle Jurassic (197-161 Ma) ophiolites (Siddiqui, 2004), was source of South Sistan Eocene-Oligocene detritus. Note that Jurassic ages from population 1 may derive from these ophiolites.

The good preservation of zircon crystal shapes suggests a proximal source to the east-northeast of South Sistan, according to paleocurrent directions, but literature discussions impel that we also consider distant sources such as the Kohistan-Ladakh arcs and the Himalayas. Detrital zircon ages covering the Himalayas and regions further north span from 2.8 Ga to 95 Ma, while Eocene detrital zircons are absent in sandstones of Lesser Himalaya, Tethyan Himalaya and Greater Himalaya (e.g. DeCelles et al., 2000; Gehrels et al., 2011; Fig. 3.15). South Sistan sandstones have few Archean (up to 3.3 Ga) detrital zircons older than those of the Himalayan regions and the main age populations are Late Cretaceous and Eocene, younger than Himalayan populations. These misfits exclude the Himalayas and Asian regions as source areas for Eocene-Oligocene detritus of the South Sistan basin. Therefore, equivalents of the Chagai-Raskoh magmatic arc remain the most plausible source.

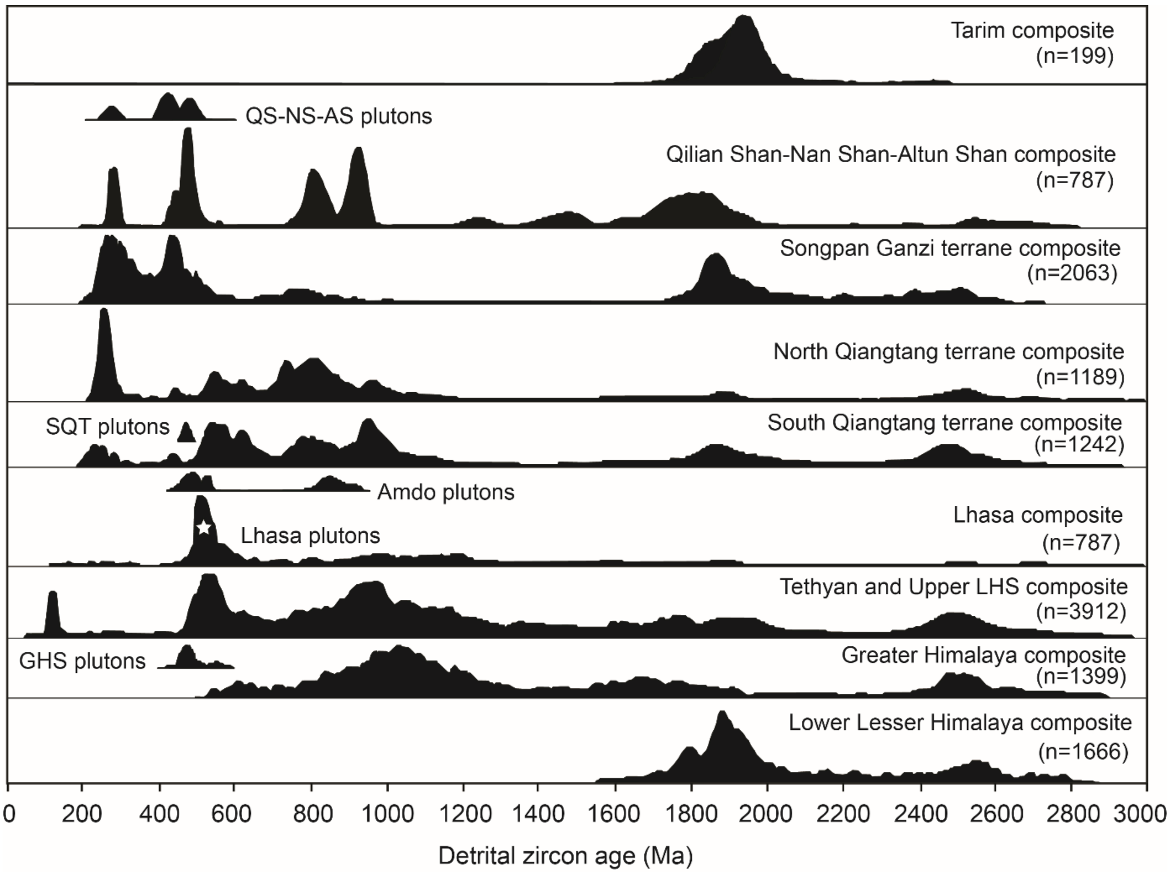

Figure 3.15: Normalized probability plots of: lower Lesser Himalayan strata (e.g. DeCelles et al., 2000; Gehrels et al., 2011), Greater Himalayan strata (e.g. DeCelles et al., 2000; Gehrels et al., 2011), Tethyan and upper Lesser Himalayan strata (e.g. Gehrels et al., 2011), Lhasa terrane (e.g. Leier et al., 2007), southern Qiangtang terrane (e.g. Gehrels et al., 2011), northern Qiangtang terrane (Gehrels et al., 2011), Songpan Ganzi terrane (Weislogel et al., 2006), Nan Shan-Qilian Shan-Altun Shan terrane and Tarim craton (Gehrels et al., 2011). LHS: Lesser Himalayan strata, GHS: Greater Himalayan strata, SQT: South Qiangtang terrane,

QS-NS-AS: Qilian Shan-Nan Shan-Altun Shan terrane. Figure and caption adapted from Gehrels et al. (2011).

Carter et al. (2010) studied provenance of Eocene-Oligocene strata of the south eastern basins in Iran, including the Neh Complex and few samples from the northern onshore Makran accretionary wedge. They reported abundant Neoproterozoic zircons (500-1000 Ma), which instead are infrequent in our measurements. This statistic difference may reflect the comparatively small amount of zircons (340) analyzed by Carter et al. (2010). Another difference is the absence, in their results, of detrital zircons of about 50 Ma. Results converge for a similarly late Cretaceous peak at 92 Ma for Carter et al. (2010) and at 89 Ma, in this work Fig. 3.12). Carter et al. (2010) attributed detrital zircons of Sistan and Makran sandstones to the Kohistan-Ladakh arcs, which have magmatic ages between 154 Ma and 29 Ma (e.g. Burg, 2011). Slightly different zircon age distribution patterns, euhedral shapes of 85% of the detrital zircons, the lack of blue amphiboles as glaucophane at the base of Kohistan (e.g. Burg, 2011) and the low abundance of amphiboles and hornblende (maximum 6% of heavy minerals) that dominate the Kohistan spectrum (Cerveny et al., 1989), are additional arguments against the Kohistan arc as source for the South Sistan sandstones.

3.5.2 Regional tectonic implications

The large quantity of detrital material in the South Sistan Basin derived from rocks from the Chaghai-Raskoh arc system, which is interpreted with a two-stage evolution. The Late Early Cretaceous-Late Cretaceous (120-65 Ma) intra-oceanic island arc collided with the Eurasian margin (Afghan Block) in Latest Cretaceous-Paleocene times; the collided arc then evolved during the Eocene to an Oligocene, mature Andean-type continental margin and continued as such to the present day (Siddiqui, 2004; Perelló et al., 2008; Nicholson et al., 2010; Richards et al., 2012). Extending this information to South Sistan, the first appearance of Cretaceous zircons with positive epsilon-$Hf_{(t)}$ and detrital Cr-spinel in sandstones records accretion of an intra-oceanic subduction system to the Afghan continental margin at 65-55Ma (Siddiqui et al., 1988). The newly accreted arc became a transitional-continental arc during the Eocene, as recorded in the detrital zircons pattern, and a mature Andean-type continental margin in Oligocene. This places full closure of the Sistan Suture Zone in the late Oligocene, in more recent times than previously accepted.

3.6 Conclusions

The present work assessed the provenance of detrital material in Eocene to Oligocene turbiditic sandstones of the Neh Complex of the South Sistan Suture Zone. Results yield protolith ages from Late Cretaceous to Eocene (115 - 49.5 Ma). The Upper Early Cretaceous ε-$Hf_{(t)}$ values range from -17 to +33 and Eocene ε-$Hf_{(t)}$ values range between -15 and +26. The combined U-

Pb ages and Hf isotope data suggest that the protolith rocks belonged to a Late Cretaceous intra-oceanic island arc transformed into Eocene transitional-continental arc, likely the Sistan (westward) extension of the Chagha-Raskoh Arc in Pakistan-Afghanistan. These results refute opinions that the Sistan detritus were supplied from Himalayan sources in a Palaeo-Indus submarine fan delta complex. Instead, the Eocene to Oligocene erosional scree was presumably transported by rivers and subsequent turbiditic flows from the Afghan active margin, to the Sistan Basin.

3.7 Acknowledgements

The authors thank the Geological Survey of Iran for efficient support during fieldwork. We gratefully acknowledge Jonas Ruh for his help in the field and Carla Müller for nannofossil determination. We also acknowledge Frowin Pirovino for his help on sandstone thin sections, Albrecht von Quadt and Markus Wälle for their support on the Laser ablation ICP-MS, Karsten Kunze for his assistance for CL and BSC imaging. This work was financed by the grant no. 2-77644-09 from the Swiss National Fond.

Chapter IV

Zahedan-Shah Kuh Plutonic Belt

4. U-Pb geochronology and geochemistry of Zahedan and Shah Kuh plutons, southeast Iran: Implication for closure of the South Sistan Suture Zone

Ali Mohammadi, Jean-Pierre Burg, Pierre Bouilhol, Jonas Ruh

This chapter has been submitted to Lithos

Abstract

The N-S trending Sistan Suture Zone in eastern Iran is attributed to eastward subduction beneath the Afghan continental block of an inlet of the Mesozoic Tethys Ocean. We present U-Pb zircon crystallization ages combined with major and trace element analyses, Sr-Nd isotopes and Hf isotope analyses of intermediate to granitic intrusions stretched along the southern segment of the SSZ. The Zahedan and Shah-Kuh Eocene plutons consist in a series of granite-granodiorite-rhyolite dated at ca 40.5-44.3 Ma and ca 28.9-30.9 Ma. Eocene plutons represent mantle magmas contaminated by ca 50% of melt derived from the turbidites of the accretionary wedge in which they have intruded. Interaction of mantle magmas with crustal turbiditic melts is responsible for the wide range of compositions. In Oligocene time, most of the magmas were generated from mantle melting, with assimilation of the surrounding turbidites. The rare setting of within-wedge intrusions is attributed to mantle upwelling reaching wedge sediments at the inception of delamination processes, which sign the end of subduction-related deformational and thermal events in the Sistan Suture Zone.

Key words: U-Pb geochronology, geochemistry, turbidites, Zahedan and Shah Kuh granites, Sistan Suture Zone.

4.1 Introduction

The tectonic construction of Iran is interpreted as the amalgamation of several continental, Gondwana-derived blocks after closure of Paleo- and Neo-Tethys-related oceanic basins (e.g. Stocklin, 1968; Berberian and King, 1981; Şengör, 1990a; Ricou, 1994). Continental collision between Arabia and Eurasia produced major faults that added to the complexity of the tectonic framework by subdividing continental blocks and reworking former suture zones. Ongoing deformation causes intense and active seismicity concentrated along these faults (Walker and Jackson, 2004; Jenkins et al., 2013). For the longer-term tectonic history, enduring debates concern the life span and closure age of the consumed oceanic basins. Indecision largely reflects the scarcity of modern data where paleontology and stratigraphic correlations remain ambiguous, in particular along the Sistan Suture Zone (Tirrul et al., 1983), in the Iran - Afghanistan - Pakistan border region (Fig. 4.1). This study presents new petrographic, geochemical and age information on igneous rocks of the southern SSZ, for which no such information existed. This project was carried out to determine the origin of these granitoids, to identify their tectonic affiliation and to specify their temporal relation with neighbouring Tethyan suture zones. Petrological and geochemical characterization points to calc-alkaline magmatism. New U-Pb measurements on zircons yield Eocene and Oligocene (ca. 44 and ca. 30 Ma) crystallization ages. The results provide new arguments for assessing models of tectonic and magmatic events during plate interaction and lithospheric behaviours in East Iran.

4.2 Geological setting

The N-S trending Sistan Suture Zone represents a Tethys-related oceanic basin reportedly closed during late Cretaceous to mid-Eocene times and overprinted by subsequent dextral strike-slip faulting between the Central Iranian Block to the west and the Afghan block to the east (Fig. 4.1; Freund, 1970; Walker and Jackson, 2004). Biostratigraphy of sedimentary rocks indicates that this oceanic basin existed already in Aptian times (Babazadeh and De Wever, 2004). This statement is strengthened by the 113 ± 1 and 107 ± 1 Ma U-Pb ages of leucogabbros in the related ophiolites near Birjand, in Northwest Sistan (Fig. 4.1; Zarrinkoub et al., 2012). The bulk eastward dip direction of the related subduction is inferred from paleogeographic, petrographic and structural considerations (e.g. Camp and Griffis, 1982; Tirrul et al., 1983; Angiboust et al., 2013). The suture zone includes three major ″complexes″ with their own litho-tectonic characteristics (Fig. 4.1): the external, southwestern ″Neh Accretionary Complex″ is a fold-and-thrust belt representing a Paleogene accretionary wedge (Tirrul et al., 1983). It is now an imbrication of late Cretaceous, allochthonous ophiolites, low-grade metamorphic rocks and Upper Cretaceous to Oligocene deep sea turbidites (Carter et al., 2010). The intermediate, ″Sefidabeh Complex″ includes the internal part of the accretionary wedge covered by clastic and volcanoclastic sedimentary rocks with interlayered carbonates and calc-alkaline lavas; this association represents the piggy-back forearc basin that formed on the wedge during convergence / subduction until pre-Oligo-Miocene deformation (Tirrul et al., 1980). Thrusting and strike-slip faulting has generally overprinted the stratigraphic, basal onlap on the underlying wedge turbidites (Tirrul et al., 1983). The Sefidabeh Complex also includes a Mid Jurassic-Paleocene intra-oceanic arc / backarc system mostly exposed in the Chagai Hills, in Pakistan and Afghanistan (Fig. 4.1; e.g. Perelló et al., 2008) and tectonically dismembered as "Nehbandan ophiolitic complex" in Iran (Fig. 4.1; Saccani et al., 2010). The internal, northwestern ″Ratuk Complex″ was described as another older (pre-Maastrichtian) accretionary wedge. It is a narrow, dense tectonic imbrication of variably metamorphosed sedimentary rocks, lavas, and meta-ophiolites (including eclogites and blueschists; e.g. Fotoohi Rad et al., 2005; Angiboust et al., 2013) separated by strongly sheared, occasionally serpentine-coated tectonic contacts that combine superposed thrusting and dextral stike-slip faulting . ^{40}Ar-^{39}Ar ages of white mica and amphibole between 139 and 116 Ma suggested that syn-convergence metamorphism was already active in the Early Cretaceous (Fotoohi Rad et al., 2009). However, these ages may be erroneous; multimethod dating (Rb-Sr, ^{40}Ar- ^{39}Ar and U-Pb) on similar lithologies from the same outcrop area yielded ages between 81 and 87 Ma (Bröcker et al., 2013), which indicates tectono-thermal activity during the Late Cretaceous. In the northern part of the SSZ, the Bibi-Maryam pluton is reported to have intruded in an intra-oceanic subduction system, prior to continental collision at 58.6 Ma (U-Pb zircon age; Delavari et al., 2014). This result implies that suturing in the Sistan area is younger than Paleocene.

The Sistan Suture could be placed at the boundary between the subducting plate and the overriding accretionary wedge, hence along the frontal, basal thrust of the Neh accretionary wedge. We prefer placing the main Sistan Suture fault at the tectonic contact (often backthrust, overprinted by dextral strike slip) between the Ratuk high-grade rocks and sediments attributed to the Helmand (Afghan) Block because the highly imbricated Ratuk Complex displays all petro-structural characteristics of an orogenic backstop interface, such as very fast exhumation of high-pressure rocks against the old and strong continental Afghan Block and intense shear strain concentration in multiple sharp contacts between various lithologies of a tectonic ″mélange″ (e.g. Angiboust et al., 2013). The abundance of ophiolitic slivers and tectonic lenses within the three ″complexes″ and geochemical signatures of ultramafic and mafic cumulates suggest intra-oceanic subduction, with an ophiolitic supra-subduction basement of the forearc and the development of the intra-oceanic arc / backarc system (Saccani et al., 2010) that continues eastward into the Chagai Hills (Fig. 4.1). Several magmatic events accompanied the tectonic history. This work is concerned with a belt of calc-alkaline and alkaline plutonic rocks previously dated mid-Oligocene and attributed to final suturing in the northern Sistan Suture Zone (Camp and Griffis, 1982; Walker et al., 2009; Pang et al., 2012; Zarrinkoub et al., 2012). The new U-Pb ages and geochemical analyses concern remote outcrops of the southern, Zahedan-Saravan segment of the SSZ, and therefore complement previous studies that mostly produced K-Ar and ^{40}Ar/^{39}Ar ages on rocks of the northern segment, to the north of Zahedan (Camp and Griffis, 1982; Pang et al., 2013; Fig. 4.1). Younger, ca. 15 to 1.5 Ma alkaline magmatism is volumetrically minor and intruded locally tensional zones along N-S dextral strike slip faults (Fig. 4.1; Pang et al., 2012). These late events are not part of this work.

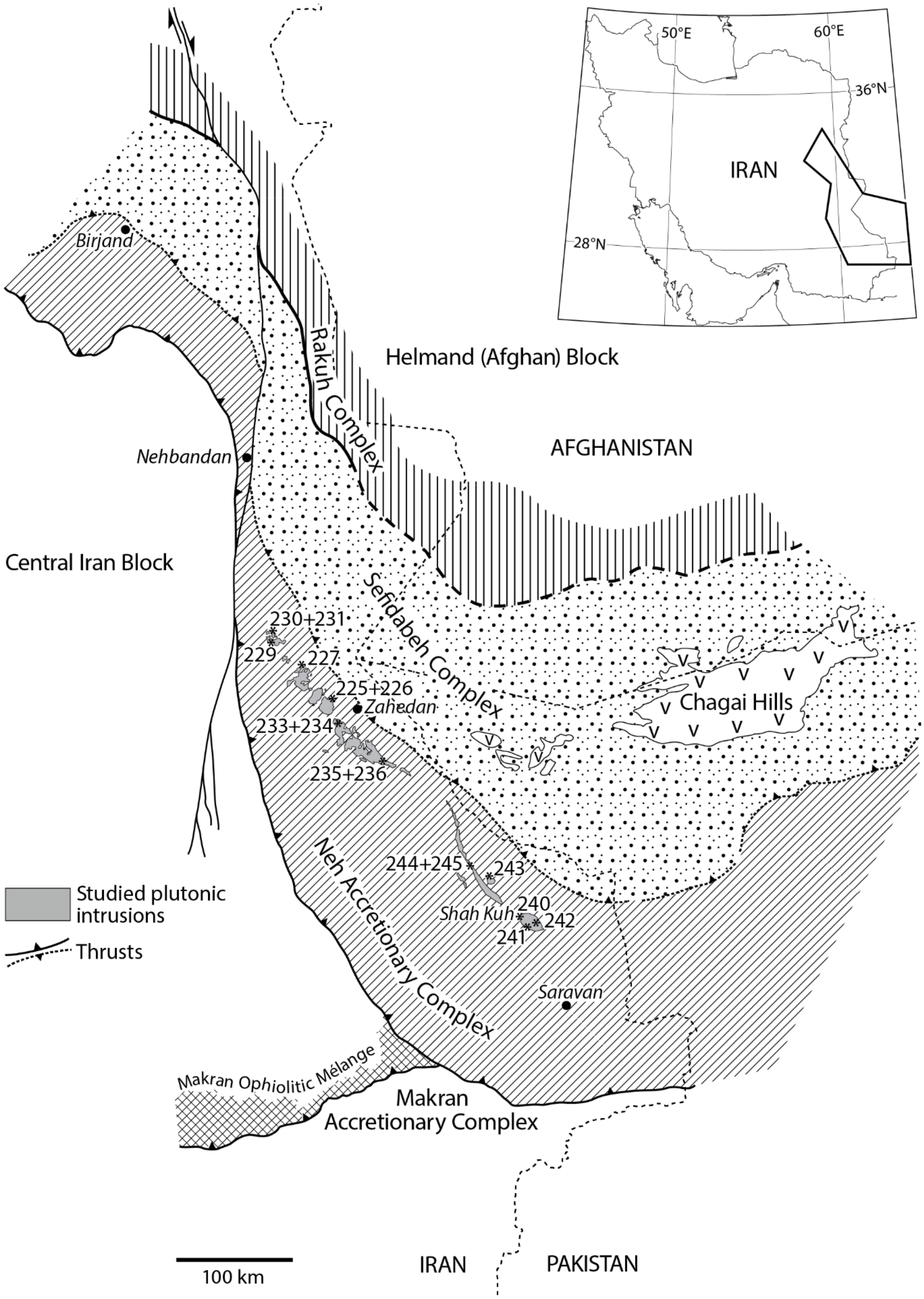

Figure 4.1: Sketch map of the Sistan Suture Zone and neighbouring regions with sample location (numbered stars). GPS points in Table 1.

4.3 Samples: Field and petrographic descriptions

Sixteen plutonic rocks (location on Fig. 4.1; Table 4.1) were selected for geochronological analysis. The sampled plutons and dykes outcrop in two clusters aligned in a WNW-ESE direction, parallel to the regional structural trends. Both clusters (informally called Zahedan, to the northwest, and Shah Kuh, to the southeast; Fig. 4.1) intruded into mostly Eocene turbidites with rare limestones and cherts (Geological Survey of Iran, 1983, 1994, 1995). Accordingly, these plutonic bodies were tentatively assigned an Eocene and Oligocene age. Sampling aimed at specifying and identifying the actual timing and composition of successive magma batches.

Table 4.1: Lithology, Location and age of Zahedan and Shah Kuh plutonic rocks and Kuh Sephid phyllite and sandstone

Sample No:	Lithology	Latitude	Longitude	location	Age (Ma)
		Degree minute second			
13 AM 225	Rhyolite (dyke)	29 38 22.9	60 45 43.5	Zahedan	28.89 ± 0.63 Ma
13 AM 226	Granite	29 38 22.9	60 45 43.5	Zahedan	28.91 ± 0.16 Ma
13 AM 227	Granodiorite	29 48 13.5	60 24 15.7	Zahedan	42.74 ± 0.28 Ma
13 AM 229	Granite	29 55 20.8	60 15 54.7	Zahedan	43.34 ± 0.19 Ma
13 AM 230	Andesite	30 00 00.3	60 16 37.1	Zahedan	44.31 ± 0.20 Ma
13 AM 231	Granite	30 00 00.3	60 16 37.1	Zahedan	43.26 ± 0.26 Ma
13 AM 233	Granite	29 24 58.3	60 41 50.0	Zahedan	29.71 ± 0.26 Ma
13 AM 234	Dacite (dyke)	29 25 20.6	60 43 58.8	Zahedan	30.46 ± 0.10 Ma
13 AM 235	Granite	29 10 40.6	60 59 55.4	Zahedan	30.93 ± 0.12 Ma
13 AM 236	Granite	29 09 01.9	61 00 16.4	Zahedan	30.76 ± 0.12 Ma
13 AM 240	Rhyolite (dyke)	27 58 33.4	62 00 50.9	Shah kuh	30.8 ± 0.27 Ma
13 AM 241	Granite	27 54 20.0	62 05 36.3	Shah kuh	43.84 ± 0.13 Ma
13 AM 242	Granite	27 54 47.9	62 08 16.0	Shah kuh	42.84 ± 0.25 Ma
13 AM 243	Granite	28 18 19.4	61 47 31.4	Shah kuh	40.54 ± 0.22 Ma
13 AM 244	Granite	28 17 07.9	61 44 38.4	Shah kuh	43.63 ± 0.32 Ma
13 AM 245	Granite	28 16 37.6	61 44 30.6	Shah kuh	43.34 ± 0.17 Ma
13 AM 237	Sandstone	27 47 37.1	61 57 41.1	Kuh Sephid	Middle Eocene
13 AM 271	Phyllite	27 58 32.7	62 00 51.5	Kuh Sephid	Middle Eocene

4.3.1 Zahedan plutonic rocks

Samples 225 to 236 (with prefix 13AM in the ETH collection) were taken from separated outcrops of the Zahedan cluster (Fig. 4.1; Table 4.1). These outcrops have been attributed to a single, ca. 75 km long pluton intruded into low-grade turbidites, with contacts often subparallel to bedding of country rocks. Variable amounts of quartz, feldspars, biotite and amphibole typify a series of granite-granodiorite-monzonite and tonalite. Magmatic fabrics suggest northwestward expansion of a granodioritic laccolith whose dioritic feeder zone stands in the southeastern outcrops (Sadeghian et al., 2005). Early magma was granitic and now envelopes the laccolith. N-S to NNE-

SSW striking andesitic to dacitic, occasionally basaltic dykes were attributed to the waning intrusion stage. Contact metamorphism developed andalusite-cordierite-sillimanite-bearing hornfels in a few tens of meters wide aureole. Grossular-wollastonite-bearing marbles are part of this metamorphic aureole (Sadeghian et al., 2005). Earlier studies yielded consistent biotite K-Ar ages of 31.4 ± 1.6 to 33.6 ± 1.7 Ma for the Zahedan pluton (Camp and Griffis, 1982).

Sample 225 is from one of the many NE-SW striking, subvertical dikes that intruded with sharp contacts the main plutonic rock (Fig. 4.2a). Despite its dark weathering colour, this sample is rhyolitic with a typical holocrystalline texture, partly resorbed phenocrysts of quartz, alkali feldspar, sanidine and anorthite grains (Fig. 4.3a). Some plagioclase grains contain glass inclusions. Accessory minerals are clinopyroxene, hornblende, apatite and zircon.

Sample 226 represents the medium- to coarse-grained (1-2 mm) main granite into which dyke 225 has intruded (Fig. 4.2a). The rock is mostly granular, with a locally faint magmatic fabric. In thin-section, it is constituted of quartz (30-35%), K-feldspar (25-30%), plagioclase (An_{10-30}; 30%) and biotite (X_{Mg} = 0.35-0.45; >5%). Ilmenite, hornblende, apatite, allanite, zircon and monazite are accessory phases. Plagioclase shows regular zoning.

Sample 227 is the granodiorite that cores the Zahedan Pluton. This medium- to coarse-grained (1-3 mm) rock characteristically contains fine-grained, mafic xenoliths with elliptic and globular shapes aligned within the NW-SE-trending magmatic fabric (Fig. 4.2b). The rock contains quartz, plagioclase (An_{25-45}), poekilitic perthitic orthoclase, hornblende and biotite locally replacing hornblende (Fig. 4.3b). Titanite, apatite, allanite, zircon, and magnetite are accessory minerals. Calcite, chlorite, epidote and sericite are common, secondary alteration phases. Most crystals are anhedral and display consertal intergrowth textures. An emplacement pressure of 170-320 MPa has been calculated from the composition of amphibole rims (Sadeghian et al., 2005).

Samples 229 and 231 are leucocratic, medium-grained, sugary textured and altered periphery granites as sample 227. Zircon, apatite, hornblende, cordierite, allanite and titanite are common accessory minerals. Ca-rich cores of subhedral plagioclase grains are strongly altered to epidote. Biotite is partly altered to chlorite. Sample 231 is less altered than sample 229.

Sample 230, is a fine- to medium-grained quartz diorite with granular and corona texture. Main minerals are plagioclase (30-35%), quartz (20-25%), clino- and orthopyroxene (10-15%), biotite (10-15%), hornblende (5-10%) and epidote (5%). Opaque minerals, zircon and apatite are accessory minerals. Biotite rims hornblende, which suggests incomplete reaction of hornblende with melt or fluid (MacKenzie et al., 1982). Plagioclase cores are strongly altered into sericite and epidote, and biotite is partly altered to chlorite.

Sample 233 is a light to grey coloured, porphyric granite with a coarse magmatic fabric primarily defined by long axes of euhedral to subhedral K-feldspar phanerocrysts and biotite (Fig. 4.2c) contained in a medium-grained (1-2 mm) matrix of quartz, feldspar and biotite. K-Feldspar often contains braided lamellae with perthitic texture. Intergrown quartz and feldspar display a granophyric and micrographic texture, which is typical for eutectic crystallization at low temperatures of high silica systems. Accessories are mostly ilmenite, hematite, hornblende, zircon and apatite.

Sample 234 is a SE-NW-striking dacite dyke with sharp boundaries with the country rock (Fig. 4.2d). This dacite includes phenocrysts of strongly zoned plagioclase, quartz and biotite embedded within a fine-grained matrix dominated by quartz, feldspar and biotite. Some few millimeter long plagioclase phenocrysts display a sieve texture and corroded, partially resorbed plagioclase cores (Fig. 4.3c).

Samples 235 and 236 are in petrographic composition similar to granites 229 and 231, yet with different degrees of alteration (236 is freshest). These samples were taken to verify that alteration difference was not reflecting composition difference.

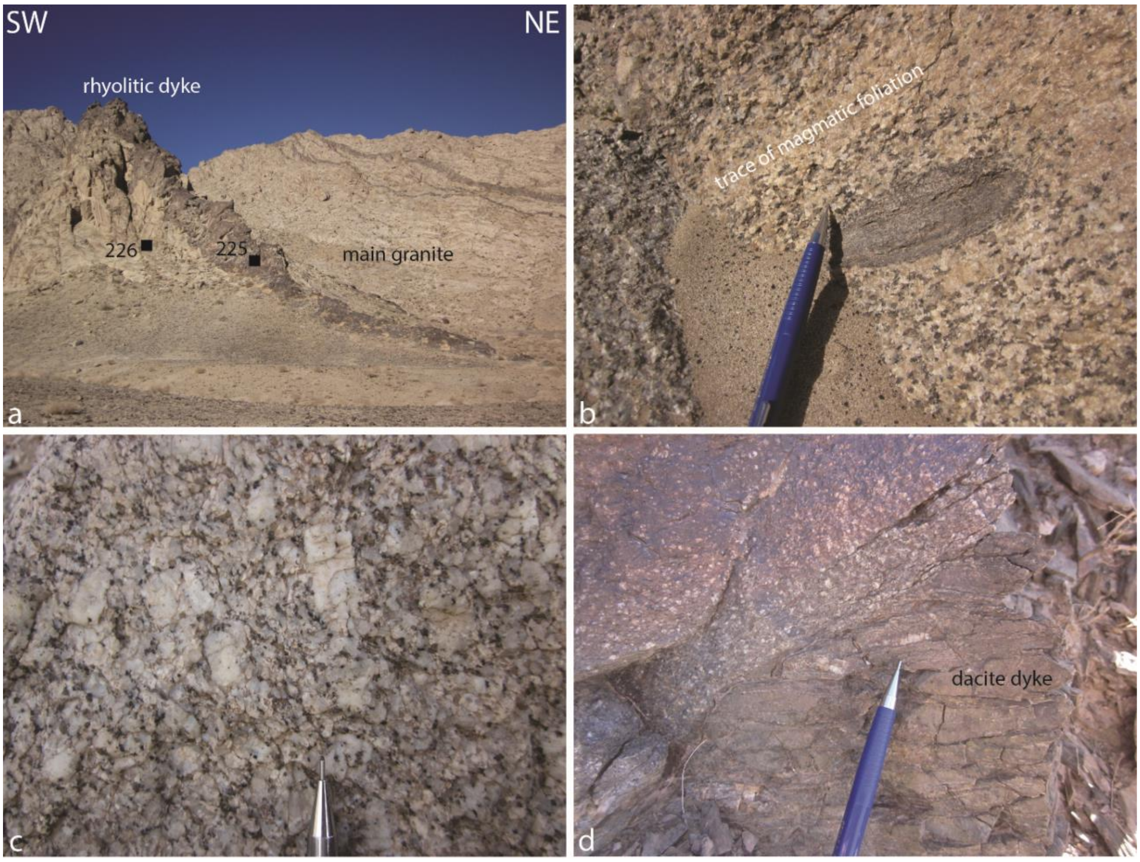

Figure 4.2: a) View of sampled outcrop with sampled place (numbered squares of granite 226 and rhyolite 225); b) Field aspect of granodiorite 227 with magmatic foliation containing basic xenolith; c) Mesocopic field photo of porphyric granite 233 with K-feldpar long axes defining the magmatic fabric; d) contact of the dacite dyke 234 into a porphyric diorite.

4.3.2 Shah Kuh plutonic rocks

Samples 240 to 245 were taken from the Shah Kuh cluster (Fig. 4.1; Table 4.1). Like for the Zahedan pluton, the dominant rock is granodiorite-tonalite with a monzonitic to granitic envelope. The rock is generally granular, with a weak magmatic fabric. The generally flat-lying foliation and the contact dominantly concordant with surrounding Eocene turbidites suggest a laccolithic intrusion. Aplitic and pegmatitic dikes are common. Dykes in the margin are mostly porphyritic microdiorite and quartz diorite. The metamorphic aureole includes chlorite- and garnet- spotted-schists, with very narrow higher grade rocks close to the contact. This suggests low temperature, shallow intrusion, which is consistent with abundant roof pendants within the pluton margins. Boulders of plutonic rocks in stratigraphically dated conglomerates were taken as evidence for a post-mid-Oligocene intrusion age (Geological Survey of Iran, 1994).

Sample 240 is one of the few meters thick peripheral dykes emanating from the main body and intrusive into the country sedimentary rocks. It is a leucocratic, fine- to medium-grained, tourmaline-bearing rhyolite. Cordierite, biotite, titanite, apatite and zircon are accessory minerals (Fig. 4.3d).

Samples 241, 242, 243 and 244 are the dominant, light- to grey-coloured and coarse-grained granite from separate outcrops. The rocks consist of quartz (35%), orthoclase and microcline (30%), plagioclase and anorthoclase (30%), hornblende (<5%) and biotite (<5%). Accessories are rutile, zircon, sphene, apatite and titanite. Epidote, zoisite, chlorite and sericite are secondary minerals. Plagioclases are subhedral with regular zoning around saussuritised cores (Fig. 4.3e). Some orthoclase grains have zircon and apatite inclusion. Biotite is locally chloritised. Sample 245 is the same granite at a site characterized by clots of biotite and titanite (Fig. 4.3f).

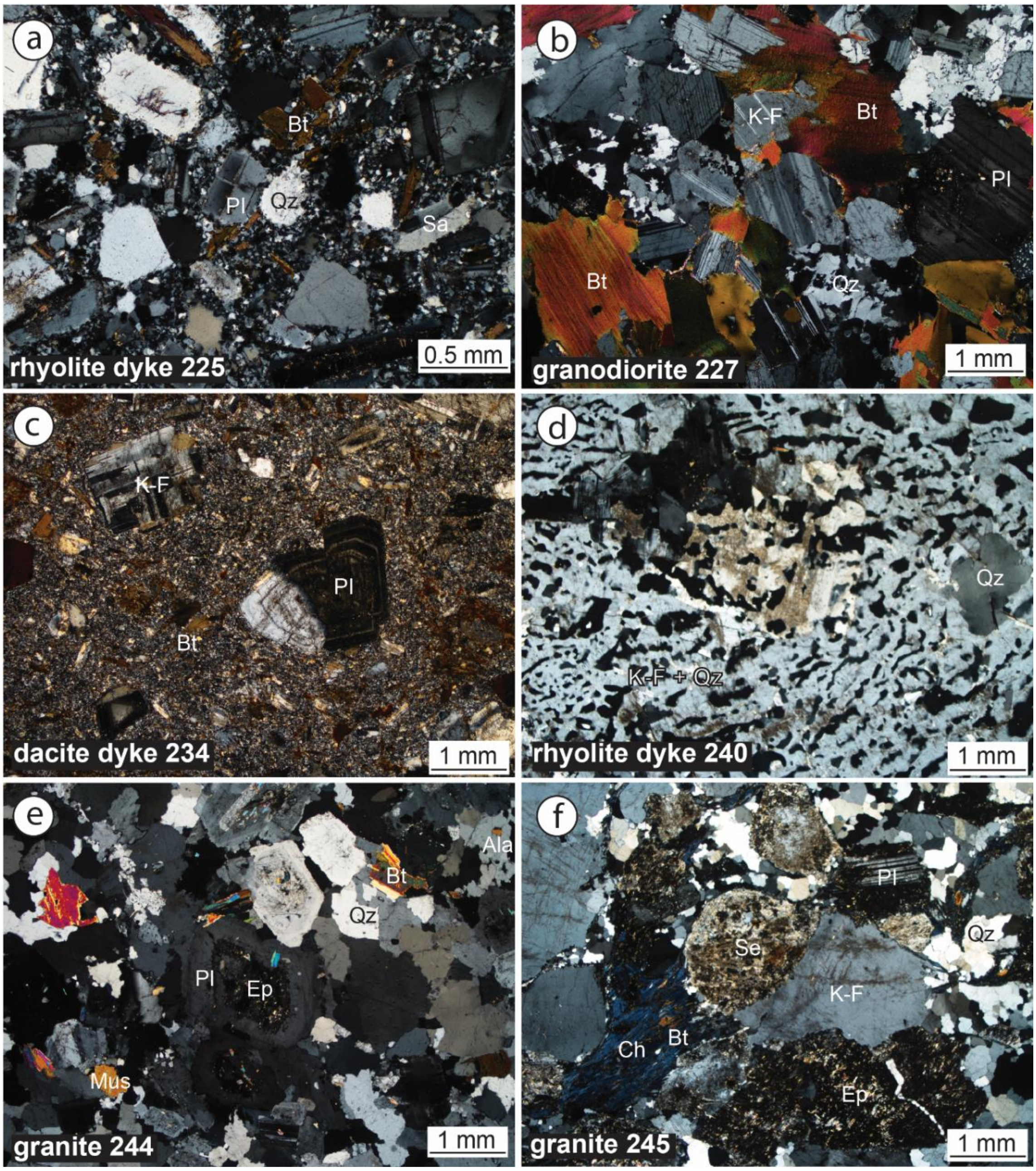

Figure 4.3: Microphotographs of representative samples (crossed polarized light): a) 225-rhyolite dyke; b) 227-granodiorite; c) 234-dacite dyke; d) 240-rhyolite dyke; e) 244-granite f) 245-granite. Ala: allanite, Bt: biotite, Ch: chlorite, Ep: epidote, K-F: alkali feldspar, Mus: muscovite, Pl: plagioclase, Qz: quartz, Sa: Sanidine, Se: sericite.

4.4 U-Pb Geochronology

U-Pb age of zircon grains (rim and core) were analysed on a La-ICP-MS at ETH Zurich (Table C.1; methodological details in Appendix C). Only data with $^{206}Pb/^{238}U$ and $^{207}Pb/^{235}U$ ages within the same 5% error range were considered to avoid data with lead loss. Crystallization ages are therefore calculated from the youngest cluster of concordant zircon grains using Isoplot3 (Ludwig, 2003). Concentric oscillatory zoning was interpreted as magmatic growth independent of position in the zircon (core or rim). Overall, our data show two magmatic events, with two clearly separated clusters of concordant ages. The first cluster is ca. 40.5 to ca. 44.3 Ma and the second age cluster spans from ca. 28.9 to ca. 30.9 Ma.

4.4.1 Eocene plutonic rocks

The presence of inherited zircon cores and grains with Cretaceous and Paleozoic ages demonstrate inheritance in all Eocene samples.

4.4.1.1 Zahedan plutonic rocks

Plutonic rocks with Eocene crystallization ages (42.74±0.28 to 44.31±0.20 Ma; Fig. 4.4) are located in the northwestern part of the Zahedan intrusions (Fig. 4.1). The analyses were done on 100-300 μm long, prismatic, colourless and euhedral zircon grains showing magmatic zoning. These zircons often show two stages of growth, with a rounded core darker or brighter in CL image than the light grey surrounding zoning (Fig. 4.5a). The occasionally composite cores consistently yield slightly older concordant ages than the rims, generally within the range of error. Some grains of granite 229 (43.34±0.19 Ma) display resorbed cores surrounded by oscillatory zoning interrupted by several resorption surfaces, the whole surrounded by zoned growth. The resorbed cores are much older than the growth zone ($^{206}Pb/^{238}U$ age of 85.7 Ma versus 44.9 Ma, respectively, Fig. 4.5b; Table C.1). One zircon core from granite 231 has a Paleozoic $^{206}Pb/^{238}U$ age of 368.0±5.5 Ma (Table C.1).

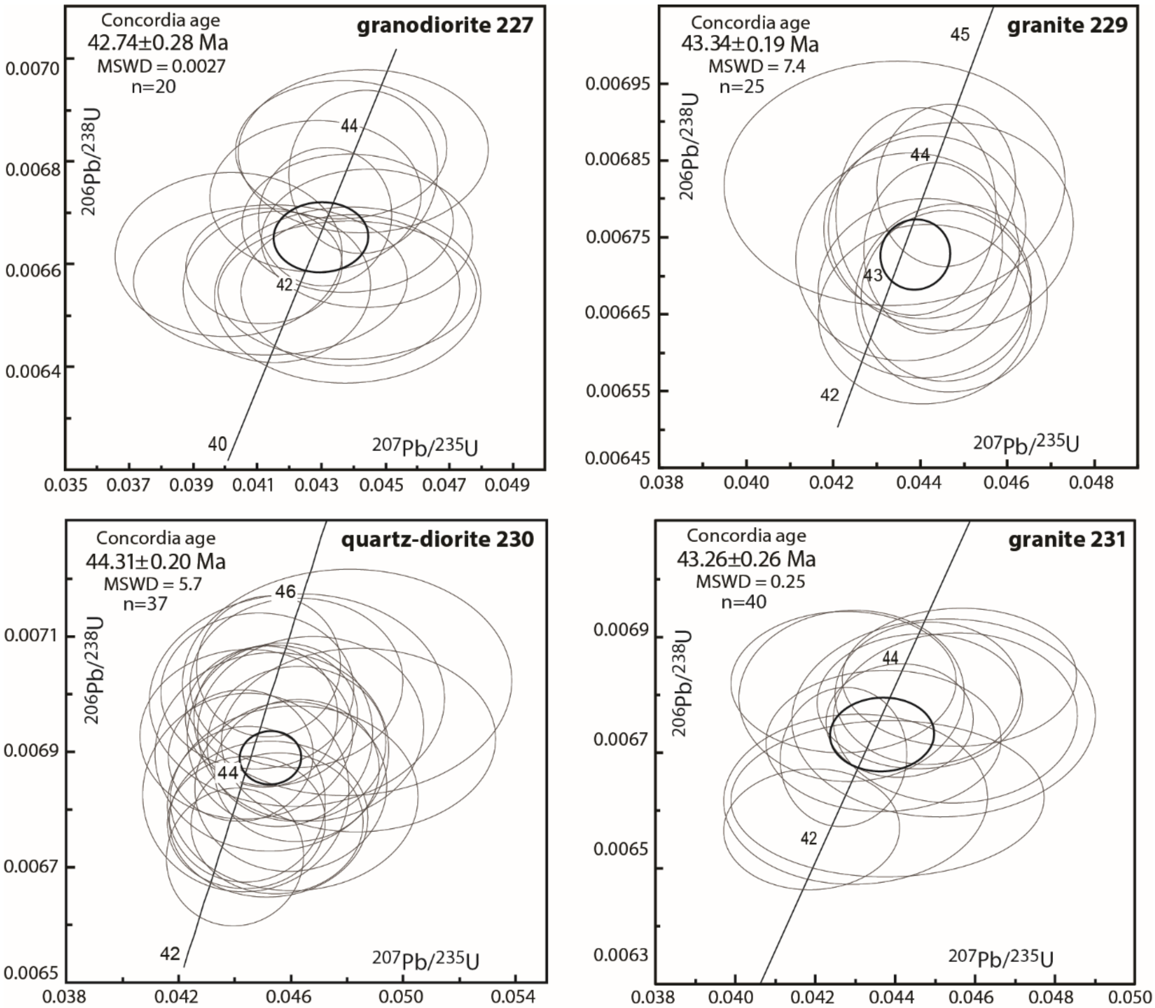

Figure 4.4: Conventional U-Pb concordia diagrams for Zahedan magmatic rocks dated Eocene by LA-ICP-MS. Mean values denote mean $^{206}Pb/^{238}U$ ages with 2σ errors. MSWD = mean square weighted deviation. n= number of analyses.

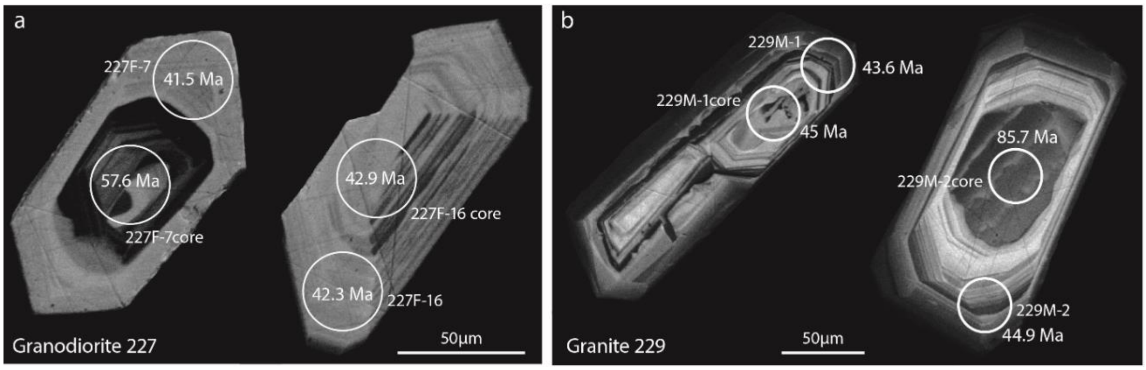

Figure 4.5: Cathodoluminescence images of typical Eocene zircons from Zahedan magmatic rocks. 30 µm diameter spot ablated with laser on rim and core of each zircon with corresponding ages (circled in CL images). Numbers next to each spot refer to analyses given in Table C.1.

4.4.1.2 Shah Kuh plutonic rocks

The Shah Kuh granites yield ages between 40.54±0.13 and 43.84±0.13 Ma (Fig. 4.6). They contain two types of zircon; prismatic and >200µm long with occasional homogeneous, prismatic cores and thin small grains (<50 width, <200µm long). Both types display partly resorbed cores

(Fig. 4.7a, b). Cores and growth zones yielded consistent ages within error. However, one zircon grain in granite 242 has a 504.8 Ma core encased in a 40.6 Ma Rim. (Fig. 4.7b).

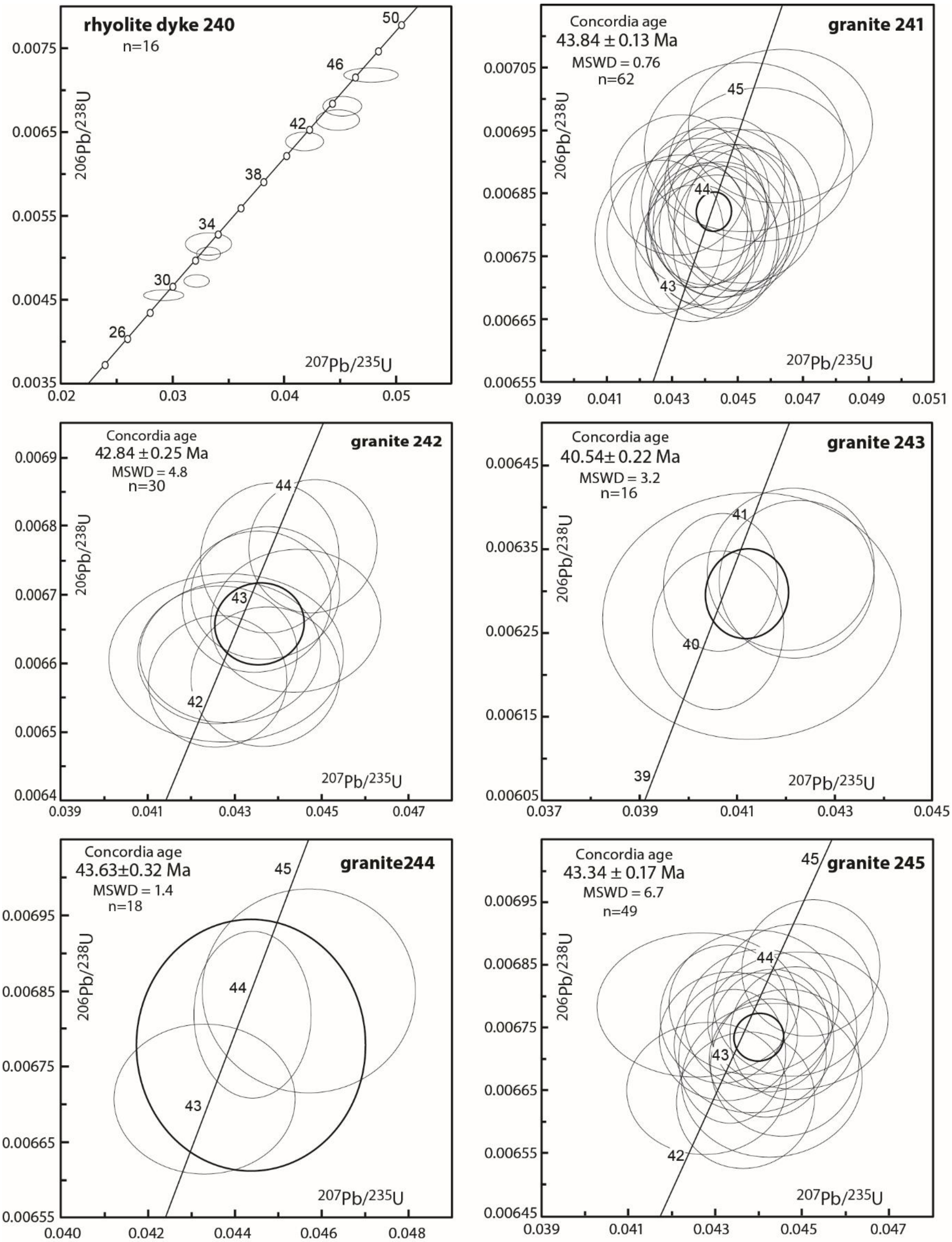

Figure 4.6: Conventional U-Pb concordia diagrams for Zahedan magmatic rocks dated Oligocene by LA-ICP-MS. Same legend as Fig. 4.4.

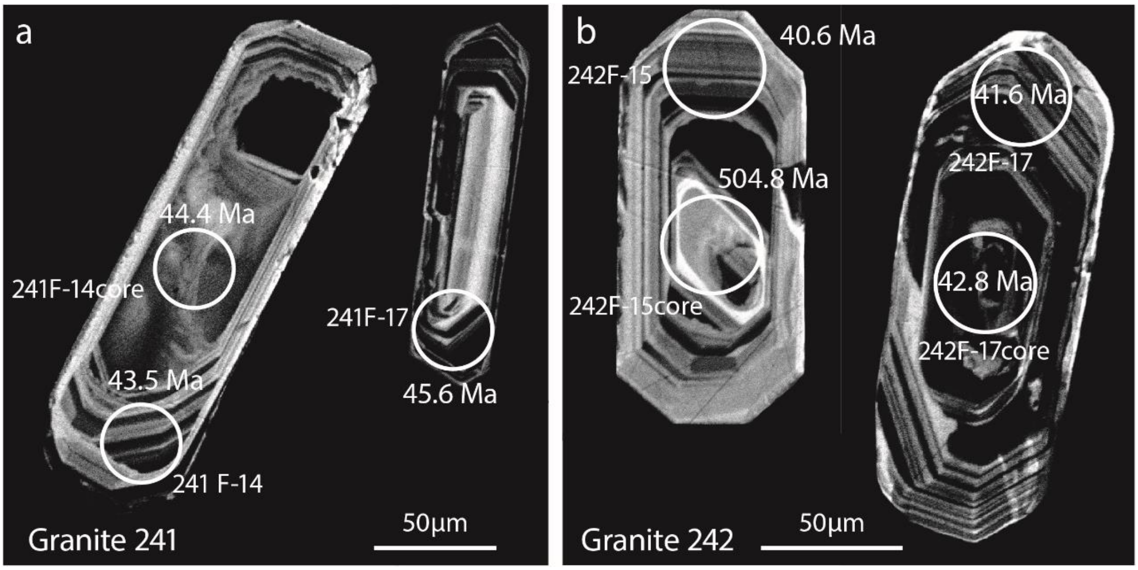

Figure 4.7: Cathodoluminscence images of typical Oligocene zircons from Zahedan magmatic rocks. Same legend as Fig. 4.5.

4.4.2 Oligocene plutonic rocks

Oligocene samples contrast drastically from Eocene ones by their overall simple zircon grain population and the absence of inherited grains (except sample 240 discussed below).

4.4.2.1 Zahedan plutonic rocks

Granitoids of Oligocene age have been found in the southern part of the Zahedan intrusions. Crystallization ages range from 28.89±0.63 to 30.93±0.12 Ma. These ages were obtained for plutons and dykes, the latter being consistently slightly younger but still within the narrow range of ages (Fig. 4.8). Granitoids yielded a population of 120 - 250 μm long euhedral zircons showing two stages of growth, with a prismatic core darker or brighter, in CL images, than the surrounding magmatic zoning. There is a small age difference within analytical error between cores and rims of each individual grain (Fig. 4.9a, b). Some zircons of leuco-granite 236 (30.76±0.12 Ma) display punctuated resorption, yet with nearly no difference between core and rim ages. The rhyolite 225 (28.89±0.63 Ma) and dacite 234 (30.46±0.10 Ma) dykes contain single populations of 120 - 150 μm long, euhedral prismatic zircons with euhedral cores overgrown by clear oscillatory, magmatic growth patterns; few grains display punctuated resorption and recrystallization (Fig. 4.9c, d). No detectable age difference exists between core and zoned rim (Fig.4. 9d; Table C.1).

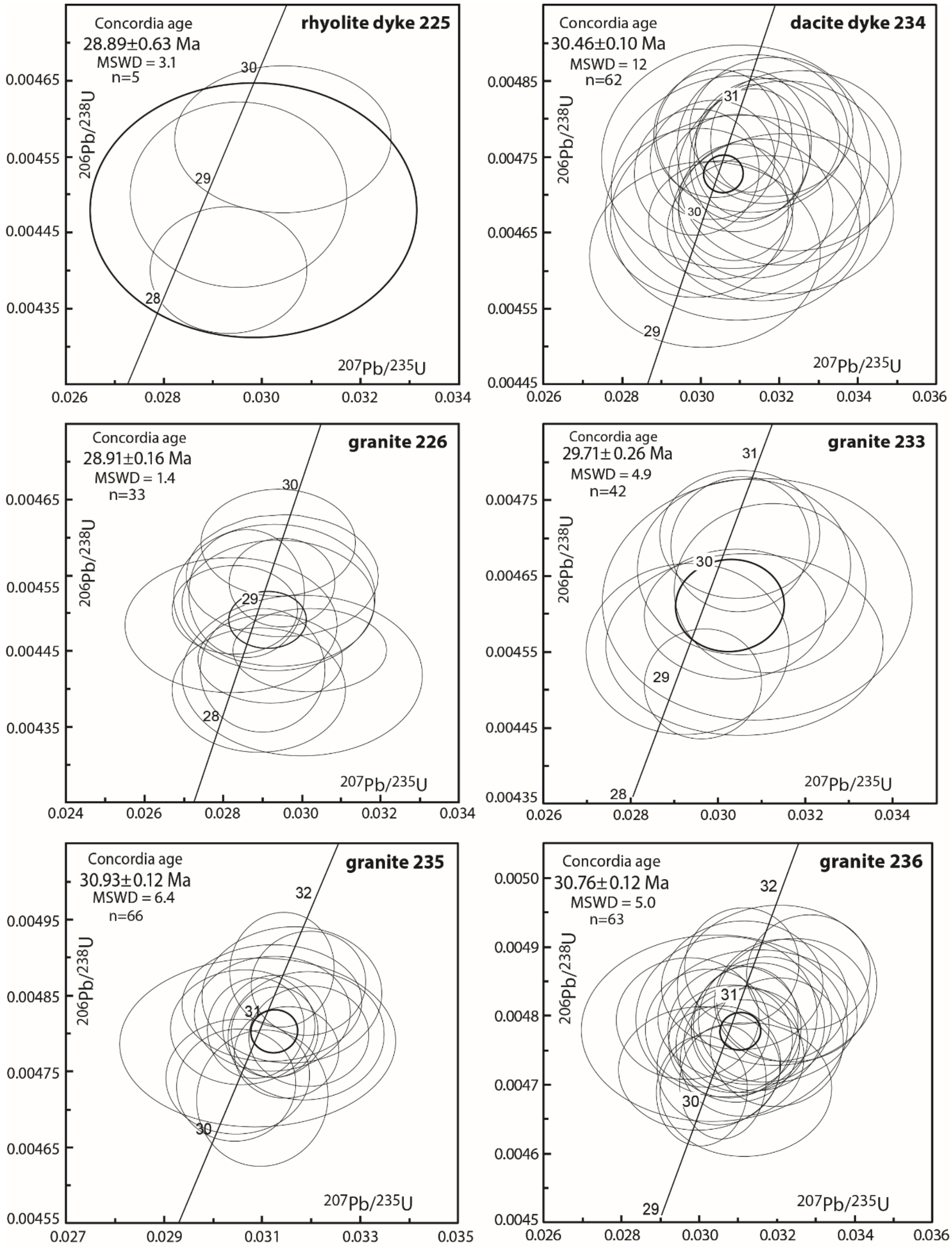

Figure 4.8: Conventional U-Pb concordia diagrams for Shah Kuh magmatic rocks dated Eocene by LA-ICP-MS. Same legend as Fig. 4.4.

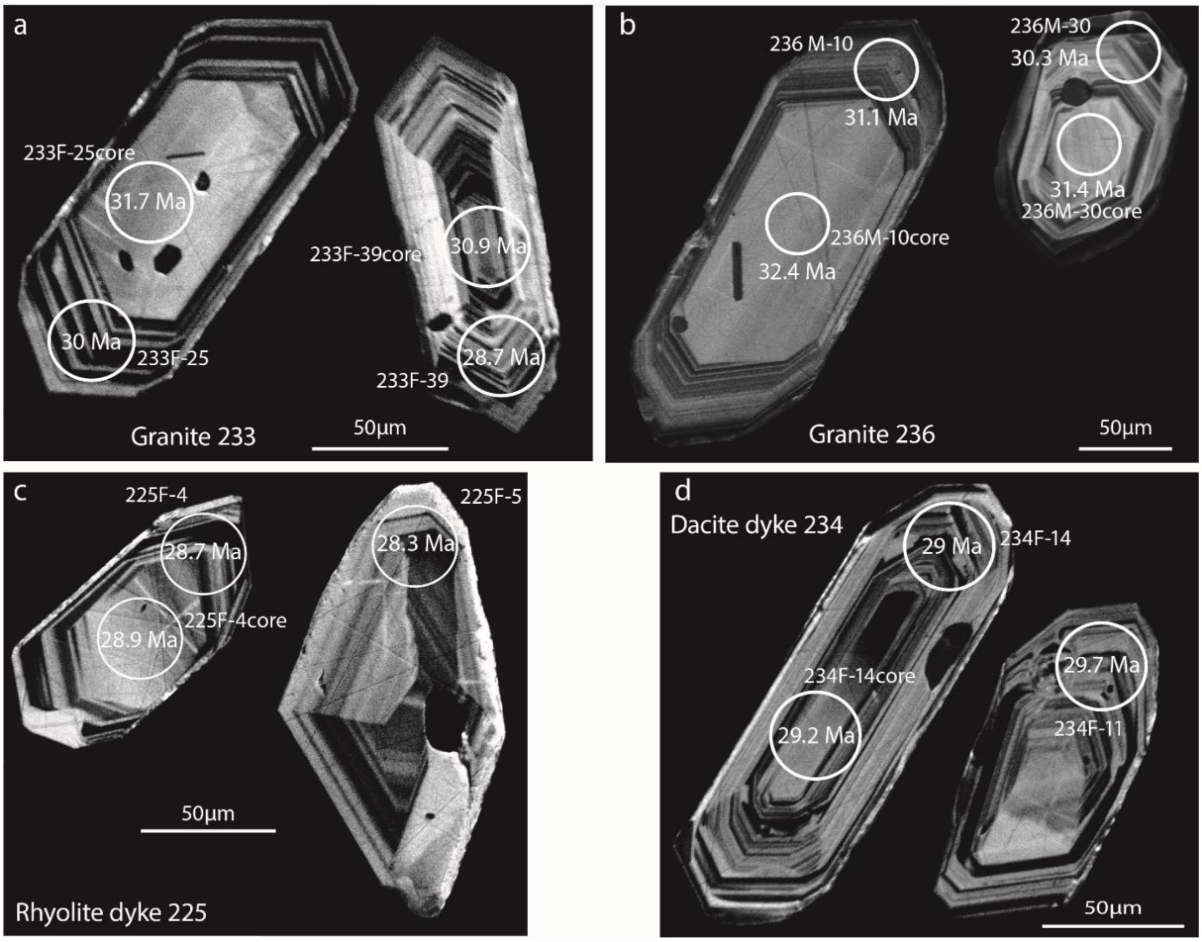

Figure 4.9: Cathodoluminescence images of typical Eocene zircons from Shah Kuh magmatic rocks. Same legend as Fig. 4.5.

4.4.2.2 Shah Kuh plutonic rocks

From the Shah Kuh intrusions, only the leucocratic, tourmaline-bearing dyke 240 has an Oligocene age. This sample is rather peculiar because of the abundance of inherited grains. The euhedral, 100-180 μm long and oscillatory zoned zircon grains with prismatic cores shows concordant dates that have $^{206}Pb/^{238}U$ age spreading from 29.34 to 46.15Ma (Fig. 4.6; Table C.1). In this sample, 4 grains out of 16 have Oligocene age, the others are Eocene. We therefore used the weighted mean $^{206}Pb/^{238}U$ dates of the four Oligocene zircons to calculate a crystallization age of 30.8±2.7 Ma. The Eocene crystallized rocks of the area have most likely sourced the inherited zircons grains during intrusion of this Oligocene dyke.

4.5 Lu-Hf isotopic composition

Hafnium isotopic ratios of the dated zircon grains were analysed on a Nu plasma MC-ICP-MS at ETH Zurich (Table C.2; technical details in Appendix C). Both Eocene and Oligocene zircons have scattered $\varepsilon Hf_{(t)}$ values straddling the Chondrite Uniform Reservoir (CHUR) boundary (Fig. 4.10).

4.5.1 Eocene plutonic rocks

The initial $\varepsilon Hf_{(t)}$ values of the dated Eocene zircons within one sample and across samples varies significantly over a range between -7.13 and 8.54, roughly distributed evenly on both sides of the CHUR line (Fig. 4.10; Table C.2). This wide scattering reflects a heterogeneous source that involves both a mantle and a crustal component (Patchett and Tatsumoto, 1980; Patchett, 1983). The evolved crustal signature suggests that the surrounding sandstones and phyllites were involved in the production of the granitic melts. This idea is comforted by the presence in the granitoids of inherited zircons with Paleozoic and Mesozoic ages similar to ages of clastic zircons in the intruded turbidites. This hypothesis will be further corroborated by the bulk rock geochemistry (Chapter 6).

4.5.2 Oligocene plutonic rocks

Oligocene zircons also show a scattered range of $\varepsilon Hf_{(t)}$ values, from -3.3 to 11.65, within and across samples. Also negative values indicate the participation of crustal components, high values indicate qualitatively that mantle components dominated the source of Oligocene melts more than for Eocene rocks (Fig. 4.10; Table C.2). The lack of inherited zircons and the simple population of zircon grains observed in Oligocene samples may reflect the mantle dominance (Bouilhol et al., 2013). This consideration is strengthened by Eocene inherited zircon grains with lower $\varepsilon Hf_{(t)}$ values than Oligocene zircons in sample 240. It is worth noting that Oligocene zircons evolve from ca. 31 to ca. 26 Ma toward mantle values (depleted mantle εHf at 30 Ma ≈ 15). The stronger mantle component of Oligocene rocks will now be further corroborated by the bulk rock geochemistry.

4.6 Bulk rock geochemistry

4.6.1 Methods

Whole-rock powders were prepared by grinding in an agate mill at the ETH Zurich. Major and minor element concentrations were obtained on fused glass beads by X-ray fluorescence analysis using a Panalytical Axios wavelength dispersive spectrometer (WDXRF, 2.4KV) at ETH Zurich. Analytical methods, accuracy and detection limits can be found in Bouilhol et al. (2011). Trace elements were determined with Laser ablation ICP-MS on the fused glass pills at ETH Zurich. Bulk rock Nd and Sr isotopic compositions were determined with thermal ionization mass spectrometry (TIMS) at ETH Zurich. Detailed analytical methods, standard composition and detection limits are described in Appendix C.

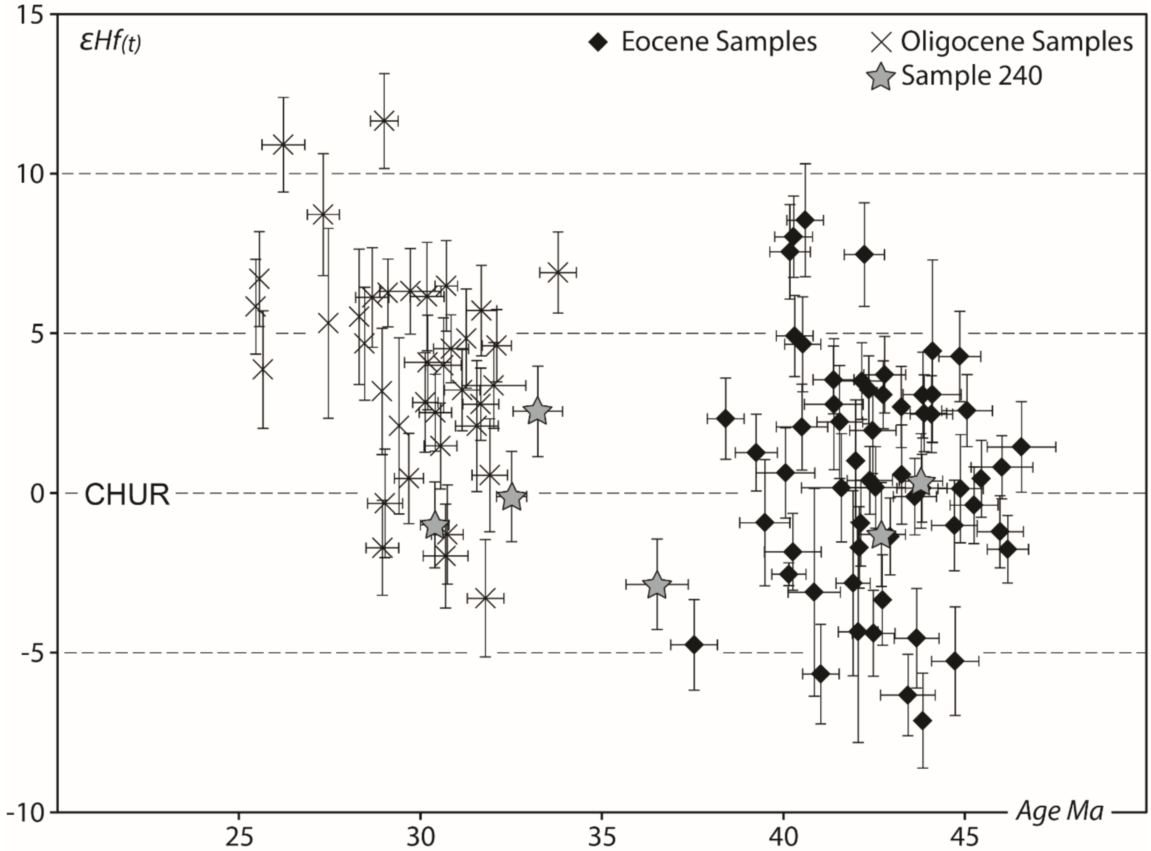

Figure 4.10: Initial Hf isotopic composition ($\varepsilon Hf_{(t)}$) of analysed zircons versus their $^{206}Pb/^{238}U$ age (Ma) for Zahedan and Shah Kuh granitoids and dykes. Oligocene sample 240 is individualized to highlight the composition of the inherited grains.

4.6.2 Results

All analysed rocks are derived from highly evolved melts, with SiO_2 content up to 75 wt %, clustered Al_2O_3 between 12.5 and 15.5 wt% and a calc-alkaline signature with element co-variation indicative of fractionation and/or crystal accumulation (Fig. 4.11; Table 4.2). However, geochemical differences in major, trace elements and isotopic compositions show that the Eocene and Oligocene rocks stem from different sources (Figs. 4.11; 4.12).

4.6.2.1 Eocene rocks

All Eocene samples have similar geochemical characteristics, except sample 245, which is described separately. Eocene rocks are characterized by Na_2O/K_2O ratio between 0.48 and 1.14 (Fig. 4.11b). Normalized to the primitive mantle (Fig. 4.12a), negative Ba, and Sr and even stronger Ti anomalies further hint to the involvement of plagioclase and Ti-oxides during the melt formation and/or evolution.

The chondrite normalized patterns (Fig. 4.12b) show a rather flat Heavy-REE (HREE) segment ($0.80 < Er_N/Lu_N < 1.18$), a slightly fractionated Middle-REE segment (MREE; $1.05 < Gd_N/Ho_N$

Table 4.2: Whole rock major and trace element XRF and LA-ICP-MS analyses of Zahedan and Shah Kuh granites and country sedimentary rocks.

Sample No:	225	226	233	234	235	236	240	227	229	230	231	241	242	243	244	245	237	271
Major oxides (wt%)																		
SiO_2	70.74	69.99	70.68	66.6	70.43	68.68	76.44	64.27	68.6	62.3	68.8	70.07	69.86	69.71	74.96	69.17	68.45	61.26
TiO_2	0.3	0.41	0.36	0.52	0.29	0.46	0.03	0.56	0.51	0.8	0.51	0.49	0.39	0.47	0.05	0.41	0.43	0.74
Al_2O_3	15.48	15.33	15.21	15.61	15.23	15.66	12.66	15.61	14.86	15.23	14.47	14.81	14.8	15.59	14.42	14.2	9.71	15.89
Fe_2O_3	2.08	2.58	2.19	3.55	1.91	2.81	0.43	4.83	3.36	6.57	3.01	2.91	2.52	2.26	0.87	3.01	3.39	6.98
MnO	0.04	0.05	0.04	0.06	0.04	0.05	0.01	0.08	0.05	0.11	0.05	0.05	0.04	0.04	0.07	0.05	0.08	0.12
MgO	0.71	0.95	1.01	2.36	0.72	1.17	0.02	2.79	1.64	3.58	1.36	1.35	1.21	0.92	0.28	1.54	2.87	4.72
CaO	2.39	2.77	2.53	3.64	2.39	2.76	0.68	3.84	2.84	4.08	2.44	2.692	2.87	2.94	1.03	2.53	5.11	4.54
Na_2O	4.45	4.21	4.09	3.7	4.29	4.16	3.66	2.26	2.96	2	2.92	3.13	3.26	3.87	3.34	2.22	3.65	1.63
K_2O	3.12	2.93	3.38	3.03	3.57	3.57	4.88	3.31	4.04	3.34	4.24	3.99	3.84	3.39	4.39	4.65	1.30	2.50
P_2O_5	0.1	0.15	0.11	0.13	0.09	0.15	0.01	0.18	0.1	0.14	0.08	0.1	0.08	0.12	0.07	0.09	0.09	0.15
LOI	0.46	0.66	0.47	1.08	0.87	0.49	0.41	1.42	0.81	1.09	0.62	0.52	0.39	0.65	0.87	1.26	5.26	1.88
Total	99.94	100.07	100.12	100.34	99.87	100.01	99.29	99.24	99.86	99.31	98.59	100.15	99.33	100	100.43	99.2	100.38	100.45
Trace elements (ppm)																		
Ga	23	24	23	24	24	24	17	22	21	24	20	22	21	21	20	20	6	17
Zn	50	50	44	56	48	53	9	67	47	90	45	45	38	33	25	44	27	91
Cu	13	3	8	24	3	9	1	36	21	35	23	10	8	10	0	6	16	31
Ni	33	27	13	45	3	18	36	84	43	99	53	18	40	30	7	29	101	170
Co	16	18	16	22	14	21	14	21	19	26	14	19	12	14	18	17	8	25
Cr	11	10	21	90	10	18	12	103	54	121	46	26	33	16	2	32	186	210
Sc	3	4	4	12	5	7	3.9	13	7	15	8	5	4	8	1	6	6	17
Cs	2.17	3.46	11.92	9.29	5.17	10.8	12.18	9.38	11.64	13.87	14.19	14.98	11.3	6.34	75.03	7.78	1.27	10.60
Rb	95.3	105.5	137.6	121.3	90.5	124	507.2	141.2	165.6	152.4	200.1	217.1	194.7	155.7	265.9	153.9	26.7	118.7
Ba	861	738	606	506	393	606	45	394	422	345	641	608	657	753	288	905	350	245

Table 4.2: Whole rock major and trace element XRF and LA-ICP-MS analyses of Zahedan and Shah Kuh granites and country sedimentary rocks.

Th	13	16.1	14.9	14.2	9.9	15.4	47.8	14.6	16.6	13.8	27.6	25.7	19.5	35.3	19.3	2.4	4.8	13.1
U	2.5	2.3	2.2	3.1	1.2	3.5	12.9	1.4	2	1.7	3.5	3.9	3.6	3.4	6.7	1.5	1.0	2.5
Nb	8.1	11.6	10.9	9.4	6.4	13.2	24.6	11.1	12.4	14.3	17.8	21.3	15.6	15.6	8.3	10.3	4.2	11.5
Ta	0.7	1	1.5	0.8	0.6	1.2	4.3	0.8	1	1	1.4	2.3	1.5	1.4	2.6	1.2	0.2	0.9
La	23.3	33.6	25.5	26.3	17.2	30.3	27.1	30.6	35.9	34	53.9	40.5	35	48.5	18	5.2	11.7	31.0
Ce	40.1	61.5	48.4	49.1	30.7	57.5	57.5	66.5	76.7	70.8	113.5	82.8	70.3	86.6	40.1	9.2	22.3	65.7
Pb	13.88	15.51	19.74	17.33	16.15	18.82	103.74	16.16	18.08	15.31	23.45	24.71	21.68	22.82	87.54	34.45	7.08	20.72
Pr	4.17	5.87	4.89	5.37	3.19	5.72	6.35	7.55	8.2	7.76	11.62	8.62	7.54	8.62	4.53	1.04	2.86	7.69
Sr	348.5	393.6	364.9	379.8	248.2	397.5	37.9	211	190.7	203.2	194.6	248	296.5	373	119.8	286.5	254.2	227.9
Nd	14.9	21	17.6	19.1	11.4	20.8	26.4	28.5	29	29.5	41.4	30.8	28.1	30.8	16.2	3.7	10.8	29.2
Sm	2.75	3.64	3.08	3.6	1.96	3.65	9.58	5.92	6.1	5.84	7.8	6.83	6.2	5.52	5.6	1.03	2.16	6.06
Zr	143.6	146.7	127.4	147.5	83.5	163.2	75.7	152.4	201	187.9	240.1	232.6	188.1	214.9	59.7	261.5	94.0	166.3
Hf	3.9	3.9	3.8	4.1	2.4	4.2	3.8	4.2	5.3	5.2	6.3	6.1	5.4	5.9	2.3	6.4	2.7	4.7
Eu	0.59	0.64	0.67	0.87	0.44	0.82	0.42	0.95	0.7	0.88	0.73	0.79	0.77	0.9	0.54	1.08	0.70	1.18
Gd	2.33	2.55	2.22	2.67	1.62	2.82	7.85	4.67	4.57	5.18	6.49	5.57	5.67	5.94	6.56	1.97	2.10	5.57
Tb	0.33	0.26	0.23	0.35	0.19	0.37	1.57	0.67	0.76	0.75	0.8	0.87	0.7	0.89	1.3	0.38	0.32	0.91
Dy	1.71	2.06	1.75	2.19	1.02	2.33	8.17	4.4	4.35	4.76	5.3	6.05	5.36	5.4	7.58	2.72	2.01	4.63
Y	8.7	9.2	9.3	11.3	5.4	11.9	60.4	24.1	24.7	26	29.7	36.9	30	27.2	49.7	18.8	10.74	28.10
Ho	0.3	0.37	0.25	0.35	0.17	0.41	1.83	0.87	0.9	0.92	0.95	1.18	0.97	0.91	1.72	0.62	0.37	1.04
Er	0.78	1.43	0.94	1.02	0.5	0.99	5.97	2.46	2.6	2.72	3.1	3.65	2.67	2.3	4.43	1.89	1.10	3.33
Ti	1785	2413	2133	3134	1375	2727	438	3363	3102	4696	3677	3498	2843	3308	425	2913	4000	7400
Tm	0.13	0.13	0.14	0.16	0.15	0.2	0.78	0.35	0.33	0.39	0.31	0.51	0.33	0.31	0.7	0.25	0.16	0.41
Yb	0.98	1.57	1.04	1.13	0.53	1.07	5.37	2.16	2.66	2.66	2.55	3.48	3.07	2.49	5.43	1.6	1.19	2.68
Lu	0.11	0.19	0.13	0.13	0.07	0.17	0.76	0.32	0.38	0.4	0.41	0.5	0.51	0.3	0.64	0.27	0.16	0.42

< 1.88), a negative Eu anomaly (0.27 < Eu* = $2Eu_N/Sm_N+Gd_N$ < 0.53) implying the role of plagioclase during their petrogenesis and a fractionated LREE segment (2.07 < LaN/SmN < 5.67) typical of granitoids. These characteristics, along with the zircon-saturated nature of the crystallizing melt witnessed by the positive Zr and Hf anomalies, indicate that Eocene rocks have crystallized from a segregated melt that left a discernible amount of fractionated phases. Initial Sr isotopic compositions ($^{87}Sr/^{86}Sr_{(i)}$) range from 0.70508 to 0.70785, correlated with initial Nd isotopic compositions ($^{143}Nd/^{144}Nd_{(i)}$) from 0.51230 to 0.51248 (-5.46 < $\varepsilon Nd_{(i)}$) < -2.10). These values cover the range of those measured in the surrounding turbiditic rocks (0.706869 < $^{87}Sr/^{86}Sr_{(i)}$ < 0.708011; 0.512323 <$^{143}Nd/^{144}Nd_{(i)}$ < 0.512416; Table 4.3), which suggests that country sedimentary rocks may have partly sourced the granitoids.

Sample 245 differs in its high Na_2O content (Na_2O/K_2O = 2.09; Fig. 4.11b) and its trace element pattern, showing a rather flat pattern from Sm to Yb, with a positive Eu anomaly (Eu* = 2.28) and a slightly fractionated LREE segment (Fig. 4.12a, b). Granite 245 contains more plagioclase and is more altered than other Eocene samples; accumulated plagioclase and late fluid alteration may well explain the lower LREE concentrations and the positive Eu anomaly.

4.6.2.2 Oligocene rocks

Among the Oligocene samples, the rhyolite dyke 240 is atypical. It is the only rock that contains a large proportion of inherited grains with Eocene age, disclosing assimilation of Eocene material. Furthermore, its REE pattern coincides with those of the Eocene granitoids, suggesting a common petrogenesis (Fig. 4.12a, b). Sample 240 also shows the highest $^{87}Sr/^{86}Sr_{(i)}$ (0.71258) of all studied rocks (Table 4.3), indicating assimilation of a crustal component that has likely affected its isotopic composition. The anomalously high Th and Pb concentrations in this sample (Fig. 4.12; Table 4.2) authenticate the continental origin of the assimilated material. All other Oligocene rocks have a higher Na_2O content than the Eocene rocks, as shown by their lower Na_2O/K_2O ratios ranging from 1.16 to 1.44 (Fig. 4.11b). M-HREE concentrations are also systematically lower than in Eocene samples. Normalized to the primitive mantle, Oligocene rocks have a HFSE negative anomaly (except for Zr and Hf, indicating zircon saturation) and overall LILLE enrichment, with a Pb positive anomaly (Fig. 4.12a). As such, these rocks display characteristics of subduction related magmas. The chondrite normalized patterns (Fig. 4.12b) show a rather flat HREE segment (0.89 < Er_N/Lu_N < 1.20), a slightly fractionated MREE segment (1.89 < Gd_N/Ho_N < 2.62), no Eu anomaly, and a fractionated LREE segment (4.71 < LaN/SmN < 5.95). The evolution of the REE with respect to major elements indicates amphibole fractionation (Fig. 4.11c, d). The isotopic compositions $^{87}Sr/^{86}Sr_{(i)}$ between 0.70488 and 0.70564; $^{143}Nd/^{144}Nd_{(i)}$ from 0.51249to 0.51260; (-2.2 < $\varepsilon Nd_{(i)}$) < 0) give evidence for less crustal contribution than for the Eocene rocks, in accordance with the Hf isotopic composition of zircon grains (Tables 4.3, C.2; Fig. 4.10).

Table 4.3: Rb-Sr and Sm-Nd isotopic data from Zahedan and Shah Kuh plutonic rocks.

Sample	225	226	233	234	235	236	240	227	229	230	231	241	242	243	244	245	237	271
Isotopic composition																		
Rb (ppm)	95	106	138	121	90	124	507	141	166	152	200	217	195	156	266	154	26	118
Sr (ppm)	348	394	365	380	248	397	38	211	191	203	195	248	296	373	120	287	254	227
$^{87}Rb/^{86}Sr$	0.774	0.759	1.067	0.904	1.032	1.067	37.856	1.895	2.458	2.124	2.911	2.479	1.859	1.181	6.283	1.521	0.297	1.471
$^{87}Sr/^{86}Sr$	0.70582	0.70595	0.70587	0.70589	0.70609	0.70535	0.72871	0.709	0.70781	0.70904	0.709	0.70703	0.70621	0.70585	0.71174	0.70773	0.70706	0.70895
2σ	0.00009	0.00012	0.00005	0.00022	0.00015	0.00023	0.00013	0.00013	0.00008	0.00012	0.00015	0.00022	0.00015	0.00022	0.00012	0.00008	0.00002	0.00001
$^{87}Sr/^{86}Sr$ i	0.70550	0.70564	0.70542	0.70550	0.70564	0.70488	0.71258	0.70785	0.70630	0.70770	0.70721	0.70549	0.70508	0.70517	0.70785	0.70679	0.70687	0.70801
Sm (ppm)	2.76	3.65	3.08	3.60	1.96	3.65	9.59	5.93	6.11	5.85	7.81	6.84	6.21	5.52	5.61	1.03	2.16	6.06
Nd (ppm)	14.94	21.05	17.58	19.06	11.40	20.83	26.44	28.49	28.96	29.48	41.42	30.81	28.05	30.76	16.21	3.66	10.87	29.24
$^{147}Sm/^{144}Nd$	0.116	0.109	0.11	0.119	0.108	0.11	0.228	0.131	0.133	0.125	0.119	0.14	0.139	0.113	0.218	0.177	0.125	0.131
$^{143}Nd/^{144}Nd$	0.512622	0.512588	0.512561	0.512543	0.512507	0.512602	0.512499	0.512369	0.512401	0.512342	0.512434	0.512414	0.512437	0.512508	0.512364	0.512401	0.512453	0.512361
2σ	0.00013	0.00003	0.00004	0.00004	0.00008	0.00004	0.00025	0.00004	0.00008	0.00004	0.00007	0.00004	0.00005	0.00008	0.00006	0.00004	0.00001	0.00001
$^{143}Nd/^{144}Nd$ i	0.51260	0.51257	0.51254	0.51252	0.51249	0.51258	0.51245	0.51233	0.51236	0.51231	0.51240	0.51237	0.51240	0.51248	0.51230	0.51235	0.51242	0.51232
εNd-i	-0.01	-0.65	-1.17	-1.55	-2.21	-0.36	-2.83	-4.89	-4.27	-5.37	-3.55	-4.05	-3.61	-2.10	-5.46	-4.51	-3.20	-5.02

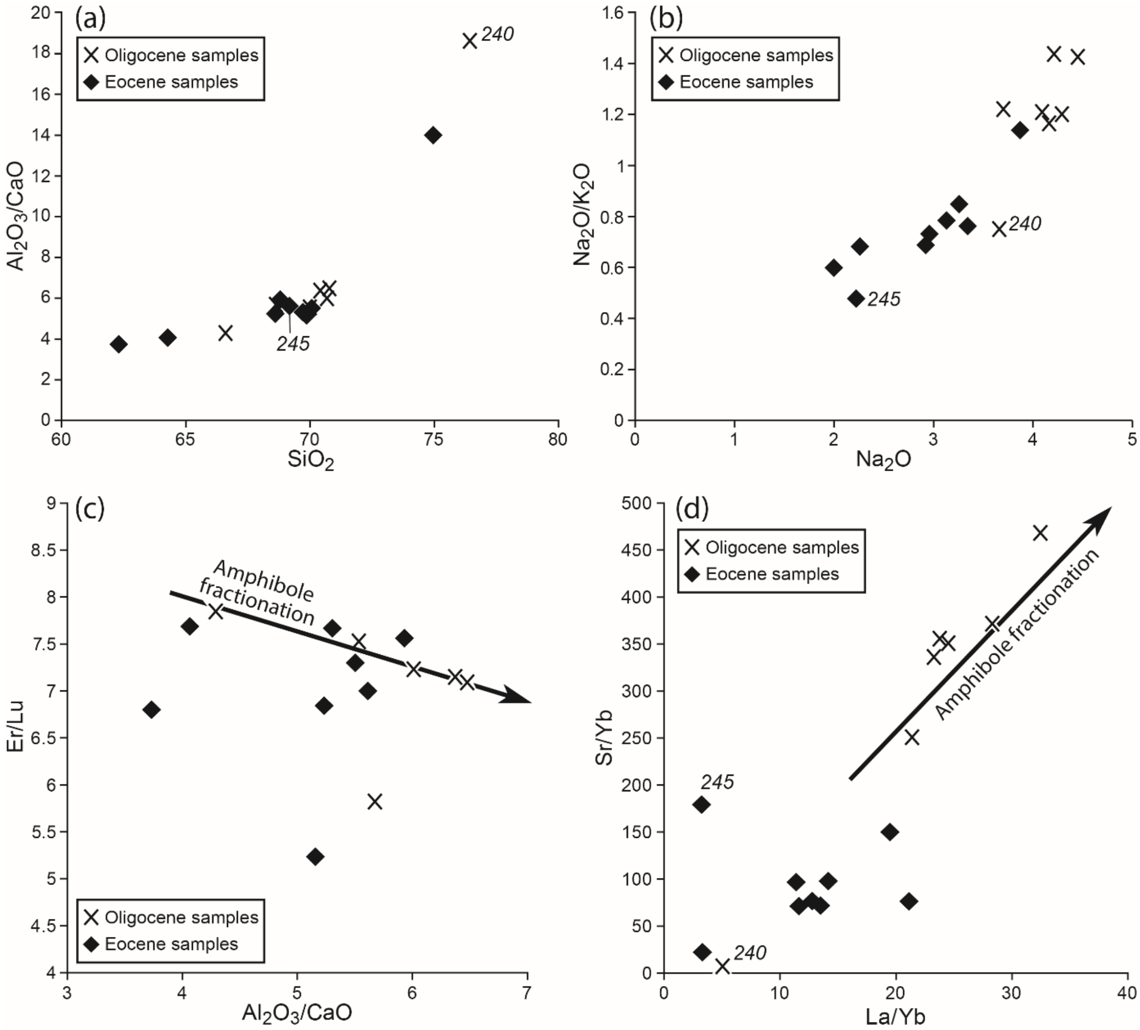

Figure 4.11: elemental variations of major (in wt%) and trace elements (ppm). a) Plots of Al_2O_3/CaO vs. SiO_2 b) Na_2O/K_2O vs. Na_2O c) Er/Lu vs. Al_2O_3/CaO and d) Sr/Yb vs. La/Yb showing the expected effect of amphibole fractionation. Sample 240 and 245 are shown, except in c) where they are largely off scale.

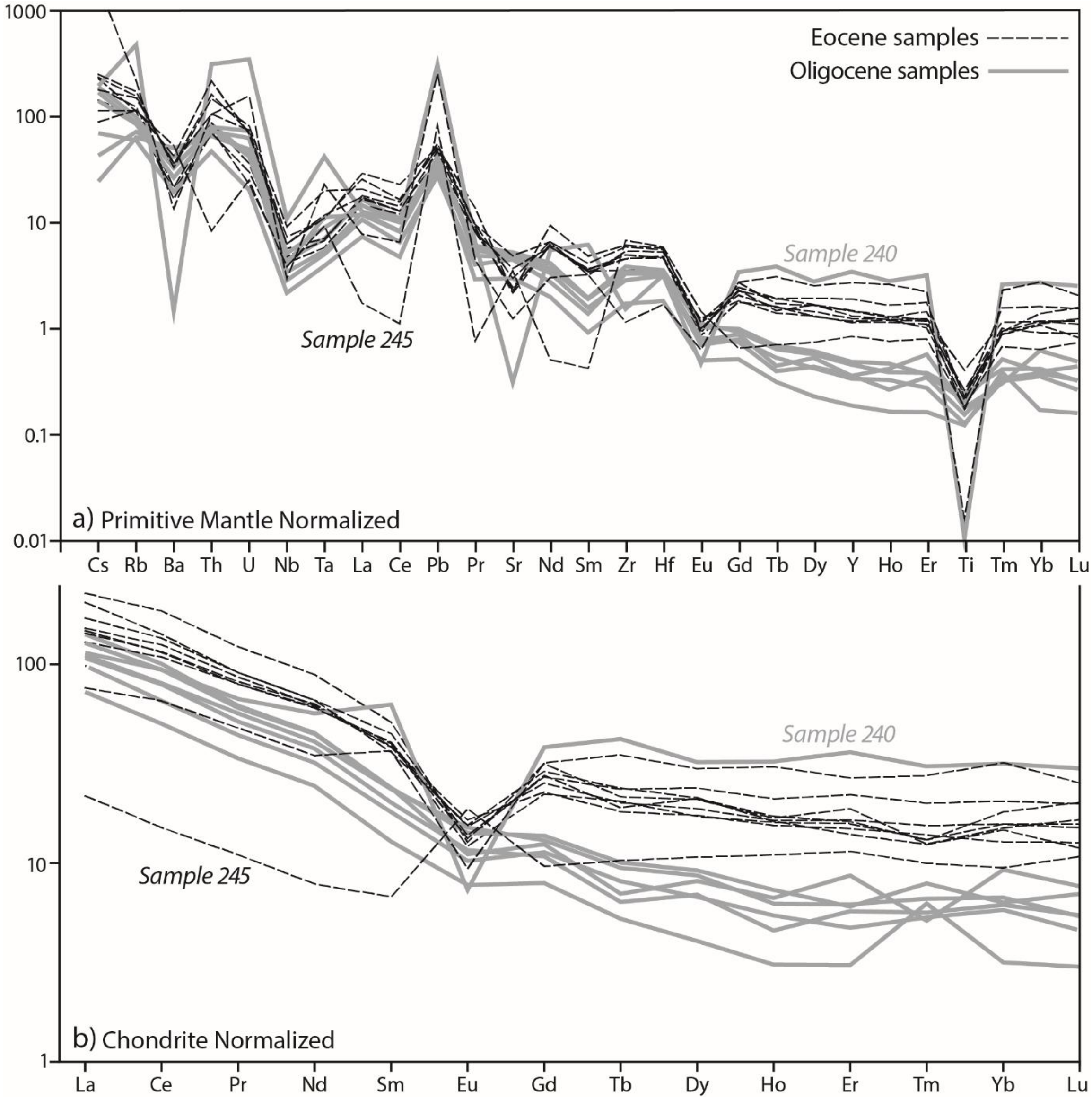

Figure 4.12: Normalized trace element diagrams for the south-Sistan magmatic rocks. a) Primitive mantle normalized spider diagram (Hofmann, 1997) b) Chondrite normalized Rare-Earth element concentrations (Sun and McDonough, 1989).

4.7 Discussion

Geochronological and geochemical results corroborate mapping data inferring that the Zahedan and Shah Kuh granitoids have intruded turbiditic rocks in Eocene and Oligocene times. They further document marked differences in magma petrogenesis.

4.7.1 Eocene melting of accretionary wedge sedimentary rocks

The Eocene granitoids have trace element compositions that denote the role of plagioclase and Ti-oxides during their genesis. These granitoids contain Paleozoic and Mesozoic inherited zircons with a manifest continental isotopic affinity similar to that of the surrounding turbidites. These observations are reconciled if the source of Eocene magmas has a similar composition as the intruded Eocene turbidites, as hypothesized by Camp and Griffis (1982). Melting the interbedded sandstones and phyllites of turbidite sequences like those exposed in South Sisitan would produce a granitic melt in equilibrium with a plagioclase and Ti-oxide-rich residue and the measured Eu and Ti negative anomalies (Figs. 4.12a; 4.13d). To test this idea, melting of sampled phyllite and sandstone out of the aureole of the studied plutonic rocks has been modelled using a Gibbs free energy minimization strategy (perplex; Connolly, 2005, 2009) to compute melting conditions and phase proportions based on the bulk rock major element concentrations. The conditions at which melting took place can only be approximated at pressure below the garnet stability (< ~ 7kbar, since there is no evidence for garnet being present at the source or during crystallization) and temperatures > 750 °C, assuming a H_2O-saturated system. Nevertheless, for reasonable conditions (770°C, 5 kbar), results (Table 4.4) show that molten turbidites may generate granitic melts both from sandstone (60% melt) and phyllites (12% melt) with different residual phases (Table 4.4) but overall with similar REE patterns as the Eocene granitoids (Fig. 4.13d). Trace element and isotopic modelling (Table 4.4; Fig. 4.13 a-c) constrain the granitic melt to be a ~ 50/50 mixture of phyllite and sandstone melts, a proportion that fits qualitative field estimates. An anomalous heat source is required to melt turbiditic sequences under such metamorphic conditions. This plausibly could be mafic intrusions. Widespread Eocene magmatism with lavas having a primitive character was recognized in the region (Pang et al., 2013). The Eocene plutonic rocks studied here identified mantle-derived melts from the anomalously high Ni (up to 100 ppm), Cr (> 100 ppm), MgO and CaO contents of the least silicic rocks. Geochemical modelling supportively shows that adding up to 50% of mantle component to the turbidite-derived granitic melt can explained the Eocene compositions (Fig. 4.13). The presence of inherited Meso- and Paleozoic zircon grains strengthens the Eocene granitoids as being generated by melting of the surrounding turbidites under garnet-out conditions. Therefore, we infer that mantle magmas intruding the wedge turbidites were responsible for melting of the sedimentary rocks at 15-20 km depth.

Table 4.4: Model parameters for turbidite melting.

	Protolith	Residual proportions and Kd			Melt	Protolith	Residual proportions and Kd				Melt
770 C 5kbar	Sandstone	orthopyroxene	clinopyroxene	plagioclase		Phyllite	orthopyroxene	plagioclase	biotite	cordierite	
		0.1	0.37	0.53	0.6		0.06	0.56	0.32	0.06	0.12
La	11.79	0.02 *	0.7 *	0.4	14.9	31.05	0.02*	0.4	0.01	0.06	44.9
Ce	22.31	0.02	0.646	0.3	29.4	65.76	0.02	0.3	0.01	0.07	98.3
Nd	10.87	0.049	1.28	0.2	13.0	29.24	0.049	0.2	0.01	0.09	45.2
Sm	2.16	0.1	1.81	0.1	2.4	6.06	0.1	0.1	0.01	0.10	9.7
Eu	0.70	0.068	2.01	3.1	0.4	1.18	0.068	3.1	0.3	0.01	0.9
Gd	2.10	0.155	1.41	0.1*	2.5	5.57	0.155	0.08	0.2	0.29	8.6
Dy	2.01	0.225	1.22	0.02	2.5	4.63	0.225	0.02	0.01	0.99	7.6
Er	1.10	0.318	1.14	0.008	1.4	3.33	0.318	0.008	0.02	3.03	5.4
Yb	1.19	0.4	1.14	0.01	1.5	2.68	0.4	0.01	0.03	1.77	4.4
Lu	0.16	0.453	1.28	0.008	0.2	0.42	0.453	0.008	0.03	4.43	0.7
Rb	26.77	0.01	0.5	0.3	36.3	118.8	0.01	0.3	2	0.08	128.6
Sr	254.3	0.01	0.50	3.40	182.3	227.9	0.01	3.40	0.1	0.12	165.4

Kd's: pyroxene from Schnetzler and Philpotts (1970); plagioclase and biotite from Bachmann et al. (2005); exept for Rb and Sr from Bacon and Druitt (1988). Cordierite from Bea et al. (1994). Phase proportions are derived from thermodynamic modelling using the thermodynamic data of (Holland and Powell, 1998; White et al., 2007). * estimated.

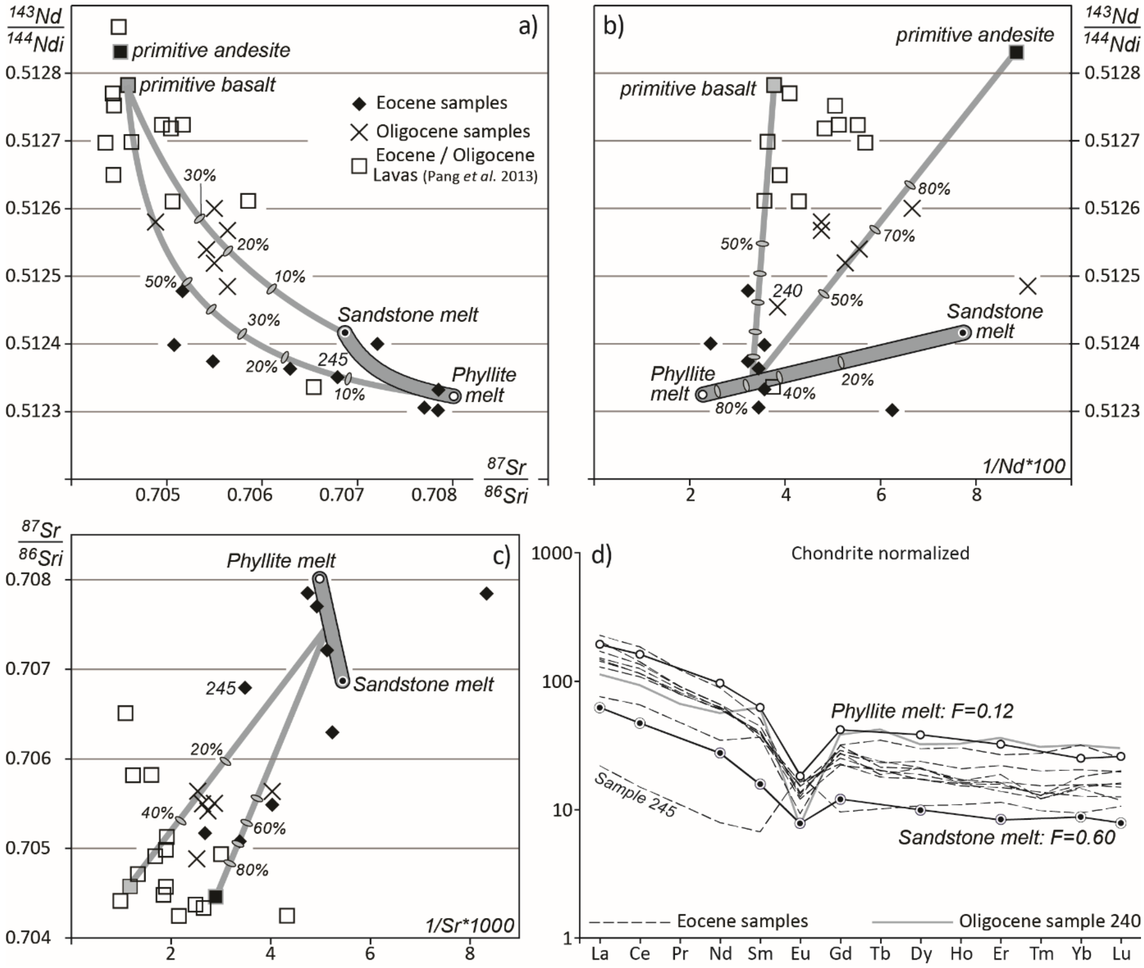

Figure 4.13: Geochemical models showing isotopic and elemental mixing between different melts. a) Initial Nd and Sr isotopic ratios (recalculated at 40 Ma) showing the Eocene and Oligocene rocks of this study compared with Eocene and Oligocene lavas of Pang et al. (2013). Two mixing lines are shown, trending between a primitive basalt and the sandstone and phyllite melts. b) Nd initial isotopic composition vs 1/Nd × 100. The Eocene compositions are best represented by a ~ 50/50 mix between the sandstone and the phyllite melts. From this mixed composition, two mixing lines are shown trending towards a primitive basalt and a primitive andesite. c) Sr initial isotopic composition vs 1/Sr × 1000, with same mixing lines as in b). Most of Eocene rocks are well represented as a mix between a granitic melt (made of ~ 50/50 sandstone-phyllite melt) and the primitive basaltic melt. Oligocene rocks can be interpreted as being an already evolved mantle magma (andesite) contaminated by this granitic melt. d) Chondrite normalized REE diagram showing the composition of the Eocene samples and Oligocene sample 240 compared to the modelled turbiditic melts (circled points linked by solid line). Eocene samples and sample 240 plot as a mix of these two melt end-members. F corresponds to melt proportion (Table 4.4).

4.7.2 Mantle-derived Oligocene magmatism

The studied Oligocene samples show contrasting geochemical aspects, with an enriched light to middle REE element pattern, no Eu anomaly and a slightly to flat HREE segment (Fig. 4.12a, b). These rocks do not have inherited zircon grains, and have a more prominent mantle component than the Eocene granitoids. The Oligocene plutonic rocks have the characteristic LILE enrichment and HFSE depletion of arc magmas, implying that there source has likely been metasomatised by a slab agent. Moreover, the isotopic compositions approach those of the most primitive lavas (Fig. 4.13 a-c) that erupted in Oligocene, further north (Pang et al., 2013), and the Hf isotopic composition of the zircon grains reaches mantle values. Following these lines of evidence, we interpret these evolved melts to have formed mainly via crystal fractionation of primitive melts extracted from a previously metasomatised mantle, as also suggested for lavas by (Pang et al., 2013). The high Sr/Yb, low Er/Lu and the slightly convex M- to HREE segments are symptomatic of amphibole fractionation (Figs. 4.11c, d; 4.12). A significant amount of crustal assimilation is required to account for the isotopic composition of the Oligocene granitoids. Our mixing model (Fig. 4.13) shows that the measured isotopic compositions with crustal values can be explained by adding ~ 50% of turbidite-derived melt to the primitive magma. The atypical composition of sample 240, which has the same chemical characteristics as the other Oligocene rocks but contains inherited zircons, is consistent with the contribution of turbidite melts during Oligocene magmatism. Ensuing melts probably participated to the fractionating melt as contaminant. We conclude that the mantle contribution increased from Eocene to Oligocene, and during the Oligocene, while suffering crustal contamination during emplacement within the turbidites.

4.7.3 Tectonic interpretation

Eocene-Oligocene magmatism is reputedly widespread throughout Iran (Berberian and Berberian, 1981; Camp and Griffis, 1982; Karimpour, 2011; Verdel et al., 2011). Pang et al. (2013) noted that mantle-derived Eocene magmatism has a wide distribution over the western Central Iran Block, the footwall plate of the Sistan Suture Zone, whereas "Oligocene magmatism was restricted to within the suture zone". The studied Zahedan and Shah Kuh rocks fit in this picture. However, rather than active magmatism from the Mid-Eocene to the Late Oligocene as inferred for the northern SSZ (Pang et al., 2013), we found two compositionally distinct events ca. 15 Ma apart. We actually noticed that previously published ages are also statistically distributed into two events.

The fact that Eocene and Oligocene granitoids occur together in a narrow belt parallel to the SSZ (Fig. 4.1) suggests that they are related to some suture-related event. In the SSZ, the 40.5-44.3 Ma (Eocene) Zahedan and Shah Kuh magmatic rocks intruded the accretionary wedge that had already begun to form in Late Cretaceous times (Fig. 4.14a), nearly 50 Ma earlier (Bröcker et al., 2013). The wedge was therefore mature, hence thick when the Eocene intrusions came in place at 5-10 km depth, equivalent to the metamorphic pressure of contact aureoles. Partial melting in the deep parts of the thick, turbiditic accretionary wedge has been previously inferred to source the subalkaline to calc-alkaline Zahedan pluton (Berberian and Berberian, 1981), thus making this pluton equivalent to similar granitoids described in the accretionary wedge of the Gulf of Alaska (e.g. Hudson et al., 1979). The same conclusion can be extended to the Eocene Shah Kuh plutonic rocks since isotopic compositions also bear evidence for mantle and crust magma mixing. Therefore, Eocene granitoids represent anatectic melts generated at depth and emplaced at higher crustal levels within the wedge itself. From the geochemical and isotopic data, we concluded that mantle-derived intrusions were the heat source for melting of wedge turbidites. Following numerical modeling of subduction/delamination processes in collision zones (Ueda et al., 2012), high temperatures at the base of the wedge are possible when delamination begins; metastability of the crust-mantle boundary unseals the plate interface (the suture) and triggers thermal advection with inflowing asthenosphere and decompression melting (Fig. 4.14b). Cooling and crystallization of the shallow intrusions within the wedge was rapid, letting latest magmas to intrude in form of dykes nearly perpendicular to the WNW-ESE regional extension direction. These dykes were tapped from the same magma chambers as the granitoids. These chambers were undergoing fractional crystallization, which explains the wide compositional range between dacite and rhyolite of the dykes. Numerical modelling also predicts that deep mantle intrusions would force a topographic high between two depressions. This offers a new interpretation of the location and geological histories of the Neh and Sefidabeh Basin (Fig. 4.14b).

The 28.9-30.9 Ma (Pang et al., 2013) magmatic rocks have a more pronounced primitive origin. They are evolved products of pervasive mantle melt interactions and crystal fractionation of basalt-andesite-dacite-rhyolite series magmas (e.g. Richards and Kerrich, 2007). Pursuing the delamination concept, the increased mantle contribution in the wedge, coeval with the magmatic flare-up in the foreland (Pang et al., 2013), track retreat of the delaminating mantle lithosphere and establishment of a wide asthenospheric window (Fig. 4.14c). We conjecture that the lithospheric differences between the Lut Block and the more western Central Iran (Tabas Block) are largely inherited from this Tertiary event, with the prominent Nayband Fault branching from the delamination tip (Fig. 4.14c).

Whether there was an Oligocene melting episode separated from the Eocene melting phase is a matter of conjecture. Alternatively, deeper Oligocene magma may have needed more time to reach their emplacement level next to Eocene intrusions. We tend to accept two different episodes, because the nearly 15 Ma difference in crystallization age seems too long to justify a depth difference of few tens of kilometres. Such results raise the questions on how intensive melting conditions are reached and how magmatism remains channelled within the accretionary wedge.

This discussion leaves open the question of linking cessation of convergence / subduction and full closure of the oceanic basin along the collision zone of the Sistan arc with Central Iran.

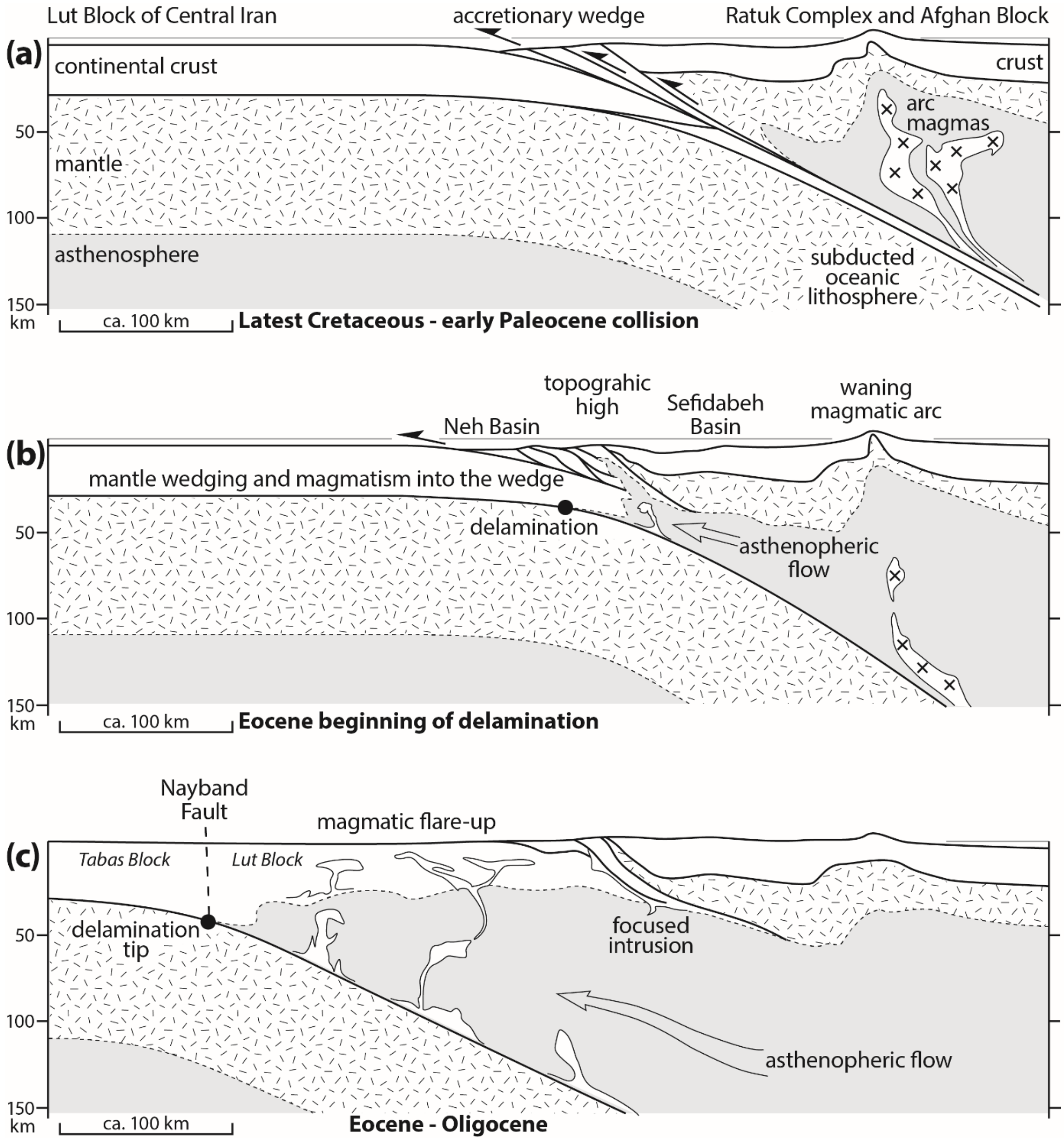

Figure 4.14: Geotectonic interpretation of the Eocene and Oligocene magmatism in the frame of the Sistan Suture Zone and its footwall Central Iran plate. Details and explanation in text.

4.8 Summary and Conclusions

Mantle-derived magmas were involved in the petrogenesis of the Zahedan and Shah Kuh plutonic rocks. In Eocene time, mantle derived magmas induced melting of the accretionary wedge, dominating the formation of the granitoids whereas, in Oligocene, fractionating mantle melts with little contamination from the turbidites was the dominant process forming the evolved magmas. Mantle and crustal melts interaction and fractional crystallization are responsible for the range of compositions produced within a short time. This implies a prominent geothermal perturbation provided from mantle/asthenosphere upwellings at the bottom of the Sistan accretionary wedge.

The measured Eocene and Oligocene intrusion ages are regionally consistent with field and biostratigraphic observations along with previously published ages of magmatic rocks from the northern part of the Sistan Suture Zone. Mid-Eocene collision was inferred from mostly biostratigraphic arguments. Our study suggests that Eocene and Oligocene deformational and thermal events in the Sistan Suture Zone were controlled by late- and post-collision delamination of the mantle lithosphere beneath Central Iran, in continuity with earlier subduction beneath the Afghan Block.

4.9 Acknowledgements

This study was funded by the Swiss National Fonds (grant 2-77644-09). Thanks are due to Albrecht von Quadt and Irena Peytcheva for their support on Rb-Sr, Sm-Nd chemical separations and isotopes analysis and their discussions and critical comments on the manuscript. Marcel Guillong and Markus Wälle for their assistance on the Laser ablation ICP-MS, Karsten Kunze for his assistance for CL and BSE imaging and Lydia Zehnder for her help with the XRF analyses. Discussions with Peter Ulmer helped understanding our analytical results and clarifying our presentation. Michael Bröcker and an anonymous person are thanked for their detailed reviews and comments on a previous manuscript.

Chapter V

Conclusion

5. Discussion and Conclusion

The goal of this thesis was to better understand the geological evolution and particularly the provenance of the thick turbiditic sedimentary rocks to reconstruct the tectonic setting of the Makran and the Sistan Basins in SE Iran.

5.1 Provenance and tectonic setting of the Makran Accretionary Wedge

Studied turbiditic and deltaic sandstones and olistostrome of the onshore Makran Accretionary Wedge are Late Cretaceous to Miocene in age. Deep marine Upper Cretaceous-Oligocene turbiditic sandstones grade up to Miocene shelf and shallow water sandstones. Sandstones classify mainly as feldspathic litharenite, lithic arkose and litharenite. Their framework modes and heavy mineral spectrum reveal a continental magmatic arc as source of Upper Cretaceous-Oligocene detritus and recycling in the Miocene sandstones. Cr-spinel and blue amphibole disclose ophiolite and high pressure-low temperature metamorphic rocks (blueschists) as supplementary provenance. Such rocks are exposed in North Makran.

Detrital zircon U-Pb ages of sandstones disclose Mid-Jurassic, Late Cretaceous and Eocene magmatic activity in the source areas. In eastern Makran zircon age distributions of Upper Cretaceous-Miocene sandstones are peaking at 167 Ma (Mid Jurassic), 88.7 Ma (Late Cretaceous) and 48.9 Ma (Eocene). In western Makran dominant zircon age populations of Eocene-Oligocene sandstones are peaking at 87 Ma (Late Cretaceous) and 48.4 Ma (Eocene). Miocene sandstone have zircon ages similar to the Eocene-Oligocene sandstones and few Mid-Jurassic grains. Neoproterozoic-Cambrian (563-868 Ma) zircon grains are rare. The occurrence of Eocene zircons in Eocene sedimentary rocks implies rapid erosion-deposition. Furthermore the dominant euhedral to anhedral shapes of the detrital zircons suggest short sediment transport distances. In accordance with the north-south paleo-slope of the Makran Basin, we conclude that there was two protolith rocks as source of sedimentary rocks. Mid-Jurassic and Late Cretaceous-Eocene magmatic arc to the north, not far from today’s North Makran.

The combined U-Pb ages and Hf isotope data indicate that the protolith rocks of the Upper Cretaceous-Oligocene sedimentary rocks formed to the north of Makran during Mid-Jurassic intracontinental rifting and others in a Late Cretaceous-Eocene continental arc. Analytical results refute opinions that the Makran detritus were supplied from Himalayan sources in a Palaeo-Indus submarine fan delta complex. Instead, sources of old zircons were likely within the Lut and Central Iran Blocks. The Upper Cretaceous-Oligocene erosional scree was presumably transported by two rivers and subsequent turbiditic flows in submarine fans from a nearby complex of continental arc and ophiolites to the north into the Makran Basin.

The configuration of Tethys in the Mesozoic and Early Cenozoic involves a continental sliver extending from the Sanandaj-Sirjan/Bajgan-Durkan complexes and tapering to the Upper Cretaceous shelf limestone of Kuh-e-Birk near the Pakistan frontier (Fig. 5.1). This continental sliver stretched between two oceans, the inner ocean to the north and the outer ocean to the south (McCall, 1995). The southern outer ocean is today's Gulf of Oman and Arabian Sea, which is subducting below Eurasia (McCall, 1995). The northern, inner ocean (north of present-day Makran) was called Fannuj Ocean by (Şengör et al., 1988; McCall, 1997). This Fannuj Ocean is represented by the ophiolites and radiolarites of North Makran (McCall, 2002). The Mid-Jurassic detrital zircon linked to rifting suggest opening of the Fannuj Ocean in the Mid-Jurassic. The Fannuj Ocean began subducting below Central Iran in the Early Cretaceous and closed in the Paleogene, as indicated by the Eocene-Oligocene shallow water sedimentary rocks (Eftekhar Nezhad et al., 1983; McCall, 2002). We called the continental arc ″North Makran continental arc″ (Chapter II). Upper Cretaceous-Eocene magmatic rocks outcropping to the north of Jaz Murian depression (Samimi Namin et al., 1992) are attributed to this arc (Fig. 5.1).

5.2 Provenance and tectonic setting of the South Sistan Suture Zone

Stratigraphic age of deep marine turbiditic sandstones of the south Sistan Basin (Neh Accretionary Wedge) spans from Eocene to Oligocene. The studied sandstones classify as lithic arkose and feldspathic litharenite. Their modal framework implies magmatic arcs as main source of Eocene-Oligocene detritus. Heavy mineral suites show very variable compositions derived from continental crust sources. Cr-spinel indicates locally important contribution from exhumed ultra-mafic rocks and ophiolites. Detrital zircon grains of Eocene-Oligocene turbiditic sandstones yielded three U-Pb age populations. The oldest population, represented by ≤ 5% of studied grains, dates from Jurassic (200 Ma) to Archean (3.3 Ga). These grains are fragments reworked from continental crystalline rocks. The second population includes detrital zircons of late Early Cretaceous - Late Cretaceous age (115-70 Ma with main peak at 89 Ma). Dominantly euhedral shapes suggest that these zircon grains were derived from proximal Upper Early Cretaceous - Late Cretaceous magmatic/volcanic rocks. $\varepsilon\text{-Hf}_{(t)}$ in this age group point to mixed oceanic crust and mantle magma source rocks, likely in an intra-oceanic island arc. The third and youngest detrital zircon age population (49.5-36 Ma with peak at 49.5 Ma) also displays dominant euhedral shapes, magmatic zoning and Hf isotopic ratios of mixed mantle and continental crust compositions, likely from a transitional-continental magmatic arc. A similar island arc-continental arc evolution at the same time is reported for the Chagai-Raskoh arc, on the nearby Pakistan-Afghanistan border (Siddiqui, 2004; Nicholson et al., 2010). Therefore, we suggest that the westward continuation of this arc system, along with the associated ophiolites, was source of

South Sistan Eocene-Oligocene detritus. The Paleocene (65-55 Ma) change in provenance is attributed to the collision between the Afghan plate and an intra-oceanic island arc not considered in previous tectonic reconstructions of this part of the Alpine-Himalayan orogenic system. Like for Makran, our results refute opinions that the Sistan detritus were supplied from Himalayan sources in a Palaeo-Indus submarine fan delta complex. Instead, the Eocene-Oligocene detritus were supplied from the Afghan active margin. The Sistan Ocean, between Central Iran and the Afghan continent, is a major feature of the Tethys realm (Tirrul et al., 1983). It is considered to have initiated in the Late Jurassic-Early Cretaceous as a long NW-SE branch of Tethys (Şengör, 1990a).

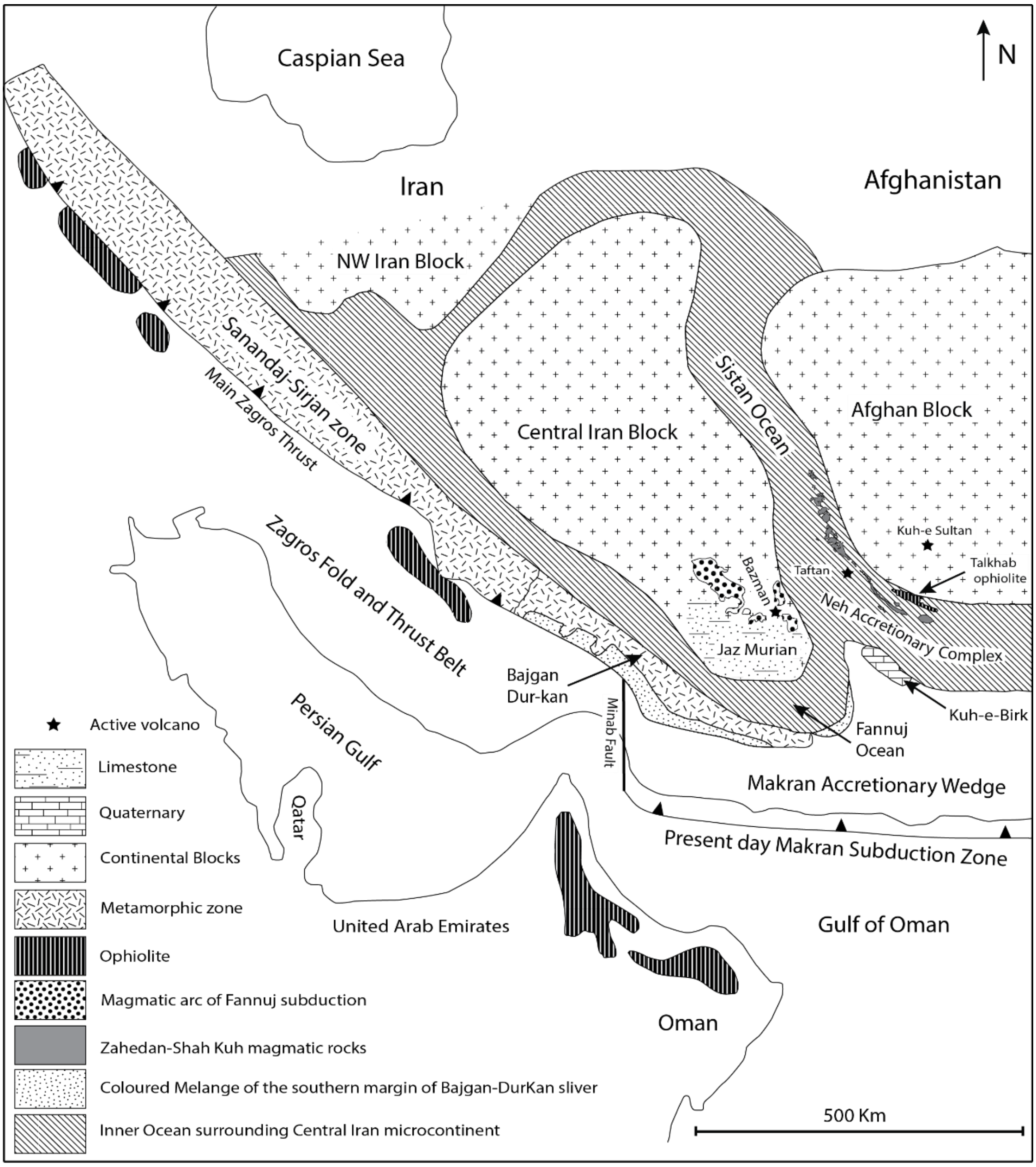

Figure 5.1: Tectonic elements of southern and central Iran modified from (McCall, 1997). Location of Cretaceous to Eocene Fannuj and Sistan interior oceans in the south and east of Central Iran continent respectively. This oceans are marked by Cretaceous ophiolites. The interior ocean is separated from the ocean located to the south by the stretched Bajgan-Dur-Kan belt outlined by the ″Coloured Melange complex″, North Makran ophiolites and Cretaceous kuh-e-Birk Limsone.

Remnants of the Sistan Ocean are found in the Cretaceous Talkhab ophiolitic mélange (Iran-Pakistan border; McCall, 1997). The inner and outer oceans discussed in Makran are likely to have merged in the southern part of the Sistan Ocean (our study area), where the Bajgan-Dur-Kan and Kuh-eBirk continental sliver ended (Fig. 5.1). The south Sistan Basin deposited in the Sistan Ocean and extends in the Eocene - Lower Oligocene deep marine turbidites of the Pakistan Makran. This basin closed after the Early Oligocene and before the shallow water Upper Oligocene sedimentary rocks (McCall, 1997). Detrital zircon and sediment provenance of the southern Sistan Basin indicates the Chaghai-Raskoh arc system as source region. The Sistan Ocean closed in the Late Eocene-Early Oligocene after eastward subduction below the Afghan microcontinent.

5.3 Age, geochemistry and tectonic setting of the Zahedan-Shah Kuh magmatic belt

The Zahedan and Shah-Kuh granite-granodiorite-rhyolite intrusions stretch along the southern segment of the Sistan Suture Zone. U-Pb zircon ages show two magmatic events. In Zahedan intrusions, plutonic rocks with Eocene crystallization age (42.7 to 44.3 Ma) are located in the northwestern part and Oligocene granitoids (28.8 to 30.9 Ma) have been found in the southeastern part. Most of the Shah Kuh granites yield Eocene ages (40.5 to 43.8 Ma); only a leucocratic dyke has concordant ages spreading from 29.3 to 46.1 Ma. The measured Eocene and Oligocene intrusion ages are regionally consistent with field and biostratigraphic observations along with previously published ages of magmatic rocks from the southern part of the Sistan Suture Zone (Camp and Griffis, 1982). $\varepsilon Hf_{(t)}$ values of the Eocene rocks with evolved crustal signature suggest that the surrounding sandstones and phyllites were involved in the production of the granitic melts. $\varepsilon Hf_{(t)}$ values of the Oligocene rocks indicate that mantle components dominated the source of Oligocene melts more than for Eocene rocks. The Rb-Sr and Sm-Nd isotopic compositions of Oligocene rocks give evidence for less crustal contribution than for the Eocene rocks, in accordance with the Hf isotopic composition of zircon grains. The Eocene plutons represent mantle magmas contaminated by ca. 50% of melt derived from the turbidites of the accretionary wedge in which they have intruded. Interaction of mantle magmas with crustal turbiditic melts is responsible for the wide range of compositions. In Oligocene time, most of the magmas were generated from mantle melting, with assimilation of the surrounding turbidites. The rare setting of within-wedge intrusions is attributed to mantle upwelling reaching wedge sediments at the inception of delamination processes, which sign the end of subduction-related deformational and thermal events in the Sistan Suture Zone, giving way to late- and post-collision delamination of the mantle lithosphere beneath Central Iran, in continuity with earlier subduction beneath the Afghan Block.

5.4 Outlook

Provenance study of the western part of the Iranian Makran will further document whether Mid-Jurassic rifting and the Cretaceous continental arc extended to the north of this region. Two separate submarine fan systems were recognized in the western and eastern parts of the study area. Studying West Makran may be instrumental in recognizing new protolith rocks and submarine fan systems.

Provenance studies in the eastern Makran is based on sandstone framework and heavy minerals (e.g. Critelli et al., 1990; Kassi et al., 2007; Kassi et al., 2013), without any paleocurrent, detrital zircon U-Pb age and Hf isotopic data. These published data are insufficient to make comparison with western Makran. Sandstone framework and heavy mineral studies helps identifying the rock type in the source area whereas interpretation of the geodynamic setting requires information on age of the protolith rocks as well as pristine magma types, as it can be quantified using detrital zircon U-Pb age and Hf isotopic data. These integrated dataset will provide a holistic picture of sediment sources in the Makran, i.e. one of the largest accretionary complexes in the world.

Provenance studies on the northern Neh Accretionary Wedge should also be carried out to better understand the geological history and tectonic setting of the Sistan Basin. This study recognized Chagi-Raskoh arc in the Afghanistan-Pakistan border as main source of sedimentary rocks. However, the question still remains open whether the same source supplied sediments to the north.

Bibliography

Aciego Pietri, J., Brookes, P., 2009. Substrate inputs and pH as factors controlling microbial biomass, activity and community structure in an arable soil. Soil Biology and Biochemistry 41, 1396-1405.

Angiboust, S., Agard, P., De Hoog, J.C.M., Omrani, J., Plunder, A., 2013. Insights on deep, accretionary subduction processes from the Sistan ophiolitic "mélange" (Eastern Iran). Lithos 156–159, 139-158.

Babazadeh, S.A., De Wever, P., 2004. Radiolarian Cretaceous age of Soulabest radiolarites in ophiolite suite of eastern Iran. Bulletin de la Société géologique de France 175, 121-129.

Bachmann, O., Dungan, M., Bussy, F., 2005. Insights into shallow magmatic processes in large silicic magma bodies: the trace element record in the Fish Canyon magma body, Colorado. Contributions to Mineralogy and Petrology 149, 338-349.

Bacon, C.R., Druitt, T.H., 1988. Compositional evolution of the zoned calcalkaline magma chamber of Mount Mazama, Crater Lake, Oregon. Contributions to Mineralogy and Petrology 98, 224-256.

Bea, F., Pereira, M., Stroh, A., 1994. Mineral/leucosome trace-element partitioning in a peraluminous migmatite (a laser ablation-ICP-MS study). Chemical Geology 117, 291-312.

Berberian, F., Berberian, M., 1981. Tectono-plutonic episodes in Iran, Zagros, Hindu Kush, Himalaya: Geodynamic Evolution. AGU, Washington, DC, pp. 5-32.

Berberian, M., King, G., 1981. Towards a paleogeography and tectonic evolution of Iran. Canadian journal of earth sciences 18, 210-265.

Blichert-Toft, J., Albarède, F., 1997. The Lu-Hf isotope geochemistry of chondrites and the evolution of the mantle-crust system. Earth and Planetary Science Letters 148, 243-258.

Bosch, D., Jamais, M., Boudier, F., Nicolas, A., Dautria, J.-M., Agrinier, P., 2004. Deep and high-temperature hydrothermal circulation in the Oman ophiolite—petrological and isotopic evidence. Journal of Petrology 45, 1181-1208.

Bouilhol, P., Jagoutz, O., Hanchar, J.M., Dudas, F.O., 2013. Dating the India–Eurasia collision through arc magmatic records. Earth and Planetary Science Letters 366, 163-175.

Bouilhol, P., Schaltegger, U., Chiaradia, M., Ovtcharova, M., Stracke, A., Burg, J.-P., Dawood, H., 2011. Timing of juvenile arc crust formation and evolution in the Sapat Complex (Kohistan–Pakistan). Chemical Geology 280, 243-256.

Bourget, J., Zaragosi, S., Ellouz-Zimmermann, S., Ducassou, E., Prins, M., Garlan, T., Lanfumey, V., Schneider, J.-L., Rouillard, P., Giraudeau, J., 2010. Highstand vs. lowstand turbidite system growth in the Makran active margin: Imprints of high-frequency external controls on sediment delivery mechanisms to deep water systems. Marine Geology 274, 187-208.

Bourget, J., Zaragosi, S., Ellouz-Zimmermann, N., Mouchot, N., Garlan, T., Schneider, J.L., Lanfumey, V., Lallemant, S., 2011. Turbidite system architecture and sedimentary processes along topographically complex slopes: the Makran convergent margin. Sedimentology 58, 376-406.

Bourget, J., Zaragosi, S., Rodriguez, M., Fournier, M., Garlan, T., Chamot-Rooke, N., 2013. Late Quaternary megaturbidites of the Indus Fan: Origin and stratigraphic significance. Marine Geology 336, 10-23.

Bröcker, M., Rad, G.F., Burgess, R., Theunissen, S., Paderin, I., Rodionov, N., Salimi, Z., 2013. New age constraints for the geodynamic evolution of the Sistan Suture Zone, eastern Iran. Lithos 170, 17-34.

Burg, J.-P., 2011. The Asia–Kohistan–India collision: review and discussion, Arc-Continent Collision. Springer, pp. 279-309.

Burg, J.-P., Dolati, A., Bernoulli, D., Smit, J., 2013. Structural style of the Makran Tertiary accretionary complex in SE-Iran, Lithosphere dynamics and sedimentary basins: The Arabian Plate and analogues. Springer, pp. 239-259.

Burg, J.P., Bernoulli, D., Smit, J., Dolati, A., Bahroudi, A., 2008. A giant catastrophic mud-and-debris flow in the Miocene Makran. Terra Nova 20, 188-193.

Byrne, D.E., Sykes, L.R., Davis, D.M., 1992. Great thrust earthquakes and aseismic slip along the plate boundary of the Makran subduction zone. Journal of Geophysical Research: Solid Earth (1978–2012) 97, 449-478.

Camp, V., Griffis, R., 1982. Character, genesis and tectonic setting of igneous rocks in the Sistan suture zone, eastern Iran. Lithos 15, 221-239.

Carter, A., Najman, Y., Bahroudi, A., Bown, P., Garzanti, E., Lawrence, R.D., 2010. Locating earliest records of orogenesis in western Himalaya: Evidence from Paleogene sediments in the Iranian Makran region and Pakistan Katawaz basin. Geology 38, 807-810.

Cerveny, P., Johnson, N., Tahirkheli, R., Bonis, N., 1989. Tectonic and geomorphic implications of Siwalik Group heavy minerals, Potwar Plateau, Pakistan. Geological Society of America Special Papers 232, 129-136.

Chen, J.H., Pallister, J.S., 1981. Lead isotopic studies of the Samail ophiolite, Oman. Journal of Geophysical Research: Solid Earth (1978–2012) 86, 2699-2708.

Clift, P.D., Lee, J.I., Hildebrand, P., Shimizu, N., Layne, G.D., Blusztajn, J., Blum, J.D., Garzanti, E., Khan, A.A., 2002. Nd and Pb isotope variability in the Indus River System: implications for sediment provenance and crustal heterogeneity in the Western Himalaya. Earth and Planetary Science Letters 200, 91-106.

Connolly, J., 2005. Computation of phase equilibria by linear programming: a tool for geodynamic modeling and its application to subduction zone decarbonation. Earth and Planetary Science Letters 236, 524-541.

Connolly, J., 2009. The geodynamic equation of state: what and how. Geochemistry, Geophysics, Geosystems 10, 1-19.

Crimes, T., McCall, G., 1995. A diverse ichnofauna from Eocene-Miocene rocks of the Makran Range (SE Iran). Ichnos: An International Journal of Plant & Animal 3, 231-258.

Critelli, S., De Rosa, R., Platt, J.P., 1990. Sandstone detrital modes in the Makran accretionary wedge, southwest Pakistan: implications for tectonic setting and long-distance turbidite transportation. Sedimentary Geology 68, 241-260.

DeCelles, P., Carrapa, B., Gehrels, G., 2007. Detrital zircon U-Pb ages provide provenance and chronostratigraphic information from Eocene synorogenic deposits in northwestern Argentina. Geology 35, 323-326.

DeCelles, P., Gehrels, G., Quade, J., LaReau, B., Spurlin, M., 2000. Tectonic implications of U-Pb zircon ages of the Himalayan orogenic belt in Nepal. Science 288, 497-499.

Deer, W.A., Howie, R.A., Zussman, J., 1992. An introduction to the rock-forming minerals. Longman London.

Delavari, M., Amini, S., Schmitt, A.K., McKeegan, K.D., Harrison, T.M., 2014. U–Pb geochronology and geochemistry of Bibi-Maryam pluton, eastern Iran: Implication for the late stage of the tectonic evolution of the Sistan Ocean. Lithos 200, 197-211.

Dickinson, W.R., 1970. Interpreting detrital modes of graywacke and arkose. Journal of Sedimentary Research 40.

Dickinson, W.R., 1985. Interpreting provenance relations from detrital modes of sandstones, Provenance of arenites. Springer, pp. 333-361.

Dickinson, W.R., Suczek, C.A., 1979. Plate tectonics and sandstone compositions. AAPG Bulletin 63, 2164-2182.

Dickinson, W.R., Valloni, R., 1980. Plate settings and provenance of sands in modern ocean basins. Geology 8, 82-86.

Dolati, A., 2010. Stratigraphy, structural geology and low-temperature thermochronology across the Makran accretionary wedge in Iran. Diss., Eidgenössische Technische Hochschule ETH Zürich, Nr. 19151, 2010.

Dolati, A., Burg, J.-P., 2013. Preliminary fault analysis and paleostress evolution in the Makran Fold-and-Thrust Belt in Iran, Lithosphere Dynamics and Sedimentary Basins: The Arabian Plate and Analogues. Springer, pp. 261-277.

Eftekhar Nezhad, J., McCall, G.J.H., 1993. Saravan geological quadrangle map: 1:250,000 Geological Survey of Iran.

Eftekhar Nezhad, J., McCall, G.J.H., Morgan, K.H., Arshadi, S., Mahdavi, m., 1983. Fannuj geological quadrangle map: 1:250,000. Geological Survey of Iran.

Eftekhar Nezhad, J., Saidi, A., Behruzi, A., 1995. Zahedan geological quadrangle map: 1:250,000. Geological Survey of Iran.
Ellouz-Zimmermann, N., Deville, E., Müller, C., Lallemant, S., Subhani, A., Tabreez, A., 2007a. Impact of sedimentation on convergent margin tectonics: Example of the Makran accretionary prism (Pakistan), Thrust Belts and Foreland Basins. Springer, pp. 327-350.
Ellouz-Zimmermann, N., Lallemant, S., Castilla, R., Mouchot, N., Leturmy, P., Battani, A., Buret, C., Cherel, L., Desaubliaux, G., Deville, E., 2007b. Offshore frontal part of the Makran Accretionary prism: The Chamak survey (Pakistan), Thrust belts and foreland basins. Springer, pp. 351-366.
Engdahl, E.R., Jackson, J.A., Myers, S.C., Bergman, E.A., Priestley, K., 2006. Relocation and assessment of seismicity in the Iran region. Geophysical Journal International 167, 761-778.
Farhoudi, G., Karig, D., 1977. Makran of Iran and Pakistan as an active arc system. Geology 5, 664-668.
Folk, R., 1968. Petrology of sedimentary rocks, 1968. Hemphills, Austin, TX, 170.
Folk, R.L., 1980. Petrology of sedimentary rocks. Hemphill Publishing Company.
Fotoohi Rad, G.R., Droop, G.T.R., Amini, S., Moazzen, M., 2005. Eclogites and blueschists of the Sistan Suture Zone, eastern Iran: A comparison of P–T histories from a subduction mélange. Lithos 84, 1-24.
Fotoohi Rad, G.R., Droop, G.T.R., Burgess, R., 2009. Early Cretaceous exhumation of high-pressure metamorphic rocks of the Sistan Suture Zone, eastern Iran. Geological Journal 44, 104-116.
Freund, R., 1970. Rotation of Strike Slip Faults in Sistan, Southeast Iran. The Journal of Geology 78, 188-200.
Fruehn, J., White, R., Minshull, T., 1997. Internal deformation and compaction of the Makran accretionary wedge. Terra Nova 9, 101-104.
Fryer, B.J., Jackson, S.E., Longerich, H.P., 1993. The application of laser ablation microprobe-inductively coupled plasma-mass spectrometry (LAM-ICP-MS) to in situ (U)- Pb geochronology. Chemical Geology 109, 1-8.
Garzanti, E., Hu, X., 2014. Latest Cretaceous Himalayan tectonics: Obduction, collision or Deccan-related uplift? Gondwana Research.
Gastaldo, R.A., 2004. The relationship between bedform and log orientation in a Paleogene fluvial channel, Weißelster Basin, Germany: implications for the use of coarse woody debris for paleocurrent analysis. Palaios 19, 587-597.
Gehrels, G., 2014. Detrital Zircon U-Pb Geochronology Applied to Tectonics. Annual Review of Earth and Planetary Sciences 42, 127-149.
Gehrels, G., Kapp, P., DeCelles, P., Pullen, A., Blakey, R., Weislogel, A., Ding, L., Guynn, J., Martin, A., McQuarrie, N., 2011. Detrital zircon geochronology of pre-Tertiary strata in the Tibetan-Himalayan orogen. Tectonics 30.
Geological Survey of Iran, 1983. Geological map of Iran at 1/100 000, Sheet 8148. Geological Survey of Iran, Tehran.
Geological Survey of Iran, 1994. Geological map of Iran at 1/250 000, Saravan Quadrangle M13 and 268 p. of explanatory text. Geological Survey of Iran, Tehran.
Geological Survey of Iran, 1995. Geological map of Iran at 1/250 000, Khash Quadrangle L12 and 90 p. of explanatory text. Geological Survey of Iran, Tehran.
Godard, M., Jousselin, D., Bodinier, J.-L., 2000. Relationships between geochemistry and structure beneath a palaeo-spreading centre: a study of the mantle section in the Oman ophiolite. Earth and Planetary Science Letters 180, 133-148.
Gradstein, F.M., Ogg, G., Schmitz, M., 2012. The Geologic Time Scale 2012 2-Volume Set. Elsevier.
Grando, G., McClay, K., 2007. Morphotectonics domains and structural styles in the Makran accretionary prism, offshore Iran. Sedimentary Geology 196, 157-179.
Griffin, W., Pearson, N., Belousova, E., Jackson, S., Van Achterbergh, E., O'Reilly, S.Y., Shee, S., 2000. The Hf isotope composition of cratonic mantle: LAM-MC-ICPMS analysis of zircon megacrysts in kimberlites. Geochimica et Cosmochimica Acta 64, 133-147.

Grigsby, J., Kassi, A., Khan, A., 2004. Petrology and geochemistry of the Oligocene-early Miocene Panjgur Formation and upper Cretaceous-Palaeocene Ispikan Formation and Wakai mélange in the Makran Accretionary Belt, southwest Pakistan. Abstract, Geological Society of America, Annual Meeting, Colorado, USA, 9th November 2004 (GSA Abstracts with Programs, 36,(5).

Guillong, M., Meier, D., Allan, M., Heinrich, C., Yardley, B., 2008. SILLS: a MATLAB-based program for the reduction of laser ablation ICP-MS data of homogeneous materials and inclusions. Mineralogical Association of Canada Short Course 40, 328-333.

Günther, D., 2002. Laser-ablation inductively-coupled plasma mass spectrometry. Analytical and bioanalytical chemistry 372, 31-32.

Haghipour, N., 2013. Active deformation and landscape evolution of the Makran Accretionary Wedge (SE-Iran). Diss., Eidgenössische Technische Hochschule ETH Zürich, Nr. 20994.

Haghipour, N., Burg, J.-P., 2014. Geomorphological analysis of the drainage system on the growing Makran accretionary wedge. Geomorphology 209, 111-132.

Haghipour, N., Burg, J.-P., Ivy-Ochs, S., Hajdas, I., Kubik, P., Christl, M., 2014. Correlation of fluvial terraces and temporal steady-state incision on the onshore Makran accretionary wedge in southeastern Iran: Insight from channel profiles and 10Be exposure dating of strath terraces. Geological Society of America Bulletin, B31048. 31041.

Haghipour, N., Burg, J.-P., Kober, F., Zeilinger, G., Ivy-Ochs, S., Kubik, P.W., Faridi, M., 2012. Rate of crustal shortening and non-Coulomb behaviour of an active accretionary wedge: The folded fluvial terraces in Makran (SE, Iran). Earth and Planetary Science Letters 355, 187-198.

Hallsworth, C., Chisholm, J., 2008. Provenance of late Carboniferous sandstones in the Pennine Basin (UK) from combined heavy mineral, garnet geochemistry and palaeocurrent studies. Sedimentary Geology 203, 196-212.

Hanghøj, K., Kelemen, P.B., Hassler, D., Godard, M., 2010. Composition and genesis of depleted mantle peridotites from the Wadi Tayin Massif, Oman Ophiolite; major and trace element geochemistry, and Os isotope and PGE systematics. Journal of Petrology 51, 201-227.

Hans, U., 2013. High-precision strontium isotope measurements on meteorites. Diss., Eidgenössische Technische Hochschule ETH Zürich, Nr. 20897, 2013.

Harms, J., Cappel, H., Francis, D., 1984. The Makran coast of Pakistan: its stratigraphy and hydrocarbon potential. Marine geology and oceanography of Arabian Sea and coastal Pakistan 3, 27.

Hawkesworth, C., Kemp, A., 2006. Using hafnium and oxygen isotopes in zircons to unravel the record of crustal evolution. Chemical Geology 226, 144-162.

Hoffman, P., 1969. Proterozoic paleocurrents and depositional history of the East Arm fold belt, Great Slave Lake, Northwest Territories. Canadian Journal of Earth Sciences 6, 441-462.

Hofmann, A., 1997. Mantle geochemistry: the message from oceanic volcanism. Nature 385, 219-229.

Holland, T., Powell, R., 1998. An internally consistent thermodynamic data set for phases of petrological interest. Journal of metamorphic Geology 16, 309-343.

Hosseini-Barzi, M., Talbot, C.J., 2003. A tectonic pulse in the Makran accretionary prism recorded in Iranian coastal sediments. Journal of the Geological Society 160, 903-910.

Hu, X., An, W., Wang, J., Garzanti, E., Guo, R., 2014. Himalayan detrital chromian spinels and timing of Indus-Yarlung ophiolite erosion. Tectonophysics 621, 60-68.

Hudson, T., Plafker, G., Peterman, Z.E., 1979. Paleogene anatexis along the Gulf of Alaska margin. Geology 7, 573-577.

Hunziker, D., 2014. Magmatic and metamorphic history of the North Makran Ophiolites and Blueschists (SE Iran): Influence of Fe3+/Fe2+ ratios in blueschist facies minerals on geothermobarometric calculations. Diss., Eidgenössische Technische Hochschule ETH Zürich, Nr. 21778.

Hunziker, D., Burg, J.-P., Caddick, M., Reusser, E., Omrani, J., 2010. Blueschists of the Inner Makran accretionary wedge, SE Iran: Petrography, geochemistry and thermobarometry, EGU General Assembly Conference Abstracts, p. 1572.

Hunziker, D., Burg, J.P., Bouilhol, P., Quadt, A., 2015. Jurassic rifting at the Eurasian Tethys margin: Geochemical and geochronological constraints from granitoids of North Makran, southeastern Iran. Tectonics 34, 571-593.

Jackson, S.E., Pearson, N.J., Griffin, W.L., Belousova, E.A., 2004. The application of laser ablation-inductively coupled plasma-mass spectrometry to in situ U–Pb zircon geochronology. Chemical Geology 211, 47-69.

Jacob, K.H., Quittmeyer, R.L., 1979. The Makran region of Pakistan and Iran: Trench-arc system with active plate subduction. Geodynamics of Pakistan 305, 317.

Jacobsen, S.B., Wasserburg, G., 1980. Sm-Nd isotopic evolution of chondrites. Earth and Planetary Science Letters 50, 139-155.

Jaffey, A., Flynn, K., Glendenin, L., Bentley, W.t., Essling, A., 1971. Precision measurement of half-lives and specific activities of U 235 and U 238. Physical Review C 4, 1889.

Jenkins, J., Turner, B., Turner, R., Hayes, G.P., Sinclair, A., Davies, S., Parker, A.L., Dart, R.L., Tarr, A.C., Villaseñor, A., Benz, H.M., 2013. Seismicity of the Earth 1900–2010 Middle East and vicinity (ver 1.1, Jan. 28, 2014). U.S. Geological Survey Open-File Report 2010–1083-K, scale 1:7,000,000.

Jones, A., 1960. Reconnaissance geology of part of West Pakistan. A Colombo Plan Cooperative Project, Govt. of Canada, Toronto,(Hunting Survey Corporation report) 550.

Karimpour, M., 2011. Review of age, Rb-Sr geochemistry and petrogenesis of Jurassic to Quaternary igneous rocks in Lut Block, Eastern Iran. Geopersia 1, 19-54.

Kassi, A.M., Grigsby, J.D., Khan, A.S., Kasi, A.K., 2015. Sandstone petrology and geochemistry of the Oligocene–Early Miocene Panjgur Formation, Makran accretionary wedge, southwest Pakistan: Implications for provenance, weathering and tectonic setting. Journal of Asian Earth Sciences 105, 192-207.

Kassi, A.M., Kasi, A.K., McManus, J., Khan, A.S., 2013. Lithostratigraphy, petrology and sedimentary facies of the Late Cretaceous-Palaeocene Ispikan Group, southwestern Makran, Pakistan. Journal of Himalayan Earth Sciences 46, 49-63.

Kassi, A.M., Khan, A.S., Kasi, A.K., 2007. Newly proposed Cretaceous-Palaeocene lithostratigraphy of the Ispikan-Wakai area, Southwestern Makran, Pakistan. Pak J Himal Earth Sci 40, 25-31.

Kassi, A.M., Khan, A.S., Kelling, G., Kasi, A.K., 2011. Facies and cyclicity within the Oligocene-Early Miocene Panjgur Formation, Khojak–Panjgur Submarine Fan Complex, south-west Makran, Pakistan. Journal of Asian Earth Sciences 41, 537-550.

Kemp, A., Hawkesworth, C., Paterson, B., Kinny, P., 2006. Episodic growth of the Gondwana supercontinent from hafnium and oxygen isotopes in zircon. Nature 439, 580-583.

Kemp, A., Wormald, R., Whitehouse, M., Price, R., 2005. Hf isotopes in zircon reveal contrasting sources and crystallization histories for alkaline to peralkaline granites of Temora, southeastern Australia. Geology 33, 797-800.

Kinny, P.D., Maas, R., 2003. Lu–Hf and Sm–Nd isotope systems in zircon. Reviews in Mineralogy and Geochemistry 53, 327-341.

Kopp, C., Fruehn, J., Flueh, E., Reichert, C., Kukowski, N., Bialas, J., Klaeschen, D., 2000. Structure of the Makran subduction zone from wide-angle and reflection seismic data. Tectonophysics 329, 171-191.

Košler, J., Fonneland, H., Sylvester, P., Tubrett, M., Pedersen, R.-B., 2002. U–Pb dating of detrital zircons for sediment provenance studies—a comparison of laser ablation ICPMS and SIMS techniques. Chemical Geology 182, 605-618.

Kukowski, N., Schillhorn, T., Huhn, K., von Rad, U., Husen, S., Flueh, E.R., 2001. Morphotectonics and mechanics of the central Makran accretionary wedge off Pakistan. Marine Geology 173, 1-19.

Qayyum, M., Niem, A.R., Lawrence, R.D., 1996. Newly discovered Paleogene deltaic sequence in Katawaz basin, Pakistan, and its tectonic implications. Geology 24, 835-838.

Qayyum, M., Niem, A.R., Lawrence, R.D., 2001. Detrital modes and provenance of the Paleogene Khojak Formation in Pakistan: implications for early Himalayan orogeny and unroofing. Geological Society of America Bulletin 113, 320-332.

Leier, A.L., Kapp, P., Gehrels, G.E., DeCelles, P.G., 2007. Detrital zircon geochronology of Carboniferous–Cretaceous strata in the Lhasa terrane, Southern Tibet. Basin Research 19, 361-378.
Ludwig, K.R., 2003. User's manual for Isoplot 3.00: a geochronological toolkit for Microsoft Excel. Kenneth R. Ludwig.
Ludwig, R., 1874. Geologische Bilder aus Italien. Bull. Soc. Imprim. Nat. Mosc 48, 42-131.
MacKenzie, W.S., Donaldson, C., Guilford, C., 1982. Atlas of igneous rocks and their textures. Longman.
Mange, M.A., Maurer, H.F., 1992. Heavy minerals in colour. Chapman & Hall London.
Mange, M.A., Wright, D.T., 2007. High-resolution heavy mineral analysis (HRHMA): a brief summary. Developments in Sedimentology 58, 433-436.
Mariano, A.N., 1989. Cathodoluminescence Emission-Spectra of Rare-Earth Element Activators in Minerals. Rev Mineral 21, 339-348.
Martens, J., 1932. Piperine as an immersion medium in sedimentary petrography. American Mineralogist 17, 198-199.
Masson, F., Anvari, M., Djamour, Y., Walpersdorf, A., Tavakoli, F., Daignières, M., Nankali, H., Van Gorp, S., 2007. Large-scale velocity field and strain tensor in Iran inferred from GPS measurements: new insight for the present-day deformation pattern within NE Iran. Geophysical Journal International 170, 436-440.
McCall, G., 1983. Mélanges of the Makran, southeastern Iran. Ophiolitic and related mélanges 66, 292-299.
McCall, G., 1985. Geological report of East Iran Project-Area No:1 (North Makran & South Baluchistan). Geological Survey of Iran Report No.57, 634.
McCall, G., 1995. The inner Mesozoic to Eocene ocean of South and Central Iran and the associated microcontinents. GEOTECTONICS C/C OF GEOTEKTONIKA 29, 490-497.
McCall, G., 1997. The geotectonic history of the Makran and adjacent areas of southern Iran. Journal of Asian Earth Sciences 15, 517-531.
McCall, G., 2002. A summary of the geology of the Iranian Makran. Geological Society, London, Special Publications 195, 147-204.
McCall, G., 2003. A critique of the analogy between Archaean and Phanerozoic tectonics based on regional mapping of the Mesozoic-Cenozoic plate convergent zone in the Makran, Iran. Precambrian Research 127, 5-17.
McCall, G., Kidd, R., 1982. The Makran, Southeastern Iran: the anatomy of a convergent plate margin active from Cretaceous to Present. Geological Society, London, Special Publications 10, 387-397.
McCall, J., Rosen, B., Darrell, J., 1994. Carbonate deposition in accretionary prism settings: Early Miocene coral limestones and corals of the Makran Mountain Range in Southern Iran. Facies 31, 141-177.
McCulloch, M., Wasse, G., 1978. Sm-Nd and Rb-Sr Chronolog3 Continental Crust Format. Science 200, 2.
Meunier, S., 1877. Composition et origine du sable diamantifere de Du Toit's Pan (Afrique australe). CR Acad. Sci., Paris 84, 250-252.
Morgen, K.H., McCall, G.J.H., Huber, H., Samimi Namin, M., 1979. Pishin geological quadrangle map: 1:250,000. Geological Survey of Iran.
Morton, A.C., Hallsworth, C.R., 1999. Processes controlling the composition of heavy mineral assemblages in sandstones. Sedimentary Geology 124, 3-29.
Naing, T., Bussien, D., Winkler, W., Nold, M., Von Quadt, A., 2014. Provenance study on Eocene–Miocene sandstones of the Rakhine Coastal Belt, Indo-Burman Ranges of Myanmar: geodynamic implications. Geological Society, London, Special Publications 386, 195-216.
Nicholson, K., Khan, M., Mahmood, K., 2010. Geochemistry of the Chagai–Raskoh arc, Pakistan: Complex arc dynamics spanning the Cretaceous to the Quaternary. Lithos 118, 338-348.
Norman, M., 1974. Improved techniques for selective staining of feldspar and other minerals using amaranth. US Geol. Surv. J. Res 2, 73-79.
Pang, K.-N., Chung, S.-L., Zarrinkoub, M.H., Khatib, M.M., Mohammadi, S.S., Chiu, H.-Y., Chu, C.-H., Lee, H.-Y., Lo, C.-H., 2013. Eocene–Oligocene post-collisional magmatism

in the Lut–Sistan region, eastern Iran: Magma genesis and tectonic implications. Lithos 180–181, 234-251.
Pang, K.-N., Chung, S.-L., Zarrinkoub, M.H., Mohammadi, S.S., Yang, H.-M., Chu, C.-H., Lee, H.-Y., Lo, C.-H., 2012. Age, geochemical characteristics and petrogenesis of Late Cenozoic intraplate alkali basalts in the Lut–Sistan region, eastern Iran. Chemical Geology 306–307, 40-53.
Pang, K.N., Chung, S.L., Zarrinkoub, M.H., Chiu, H.Y., Li, X.H., 2014. On the magmatic record of the Makran arc, southeastern Iran: Insights from zircon U-Pb geochronology and bulk-rock geochemistry. Geochemistry, Geophysics, Geosystems 15.
Patchett, P., Tatsumoto, M., 1980. Hafnium isotope variations in oceanic basalts. Geophysical Research Letters 7, 1077-1080.
Patchett, P., Tatsumoto, M., 1981. A routine high-precision method for Lu-Hf isotope geochemistry and chronology. Contributions to Mineralogy and Petrology 75, 263-267.
Patchett, P.J., 1983. Importance of the Lu-Hf isotopic system in studies of planetary chronology and chemical evolution. Geochimica et Cosmochimica Acta 47, 81-91.
Perelló, J., Razique, A., Schloderer, J., 2008. The Chagai porphyry copper belt, Baluchistan province, Pakistan. Economic Geology 103, 1583-1612.
Pettijohn, F., Potter, P., Siever, R., 1974. Sand and sandstone. Soil Science 117, 130.
Platt, J., Leggett, J., Young, J., Raza, H., Alam, S., 1985. Large-scale sediment underplating in the Makran accretionary prism, southwest Pakistan. Geology 13, 507-511.
Platt, J.P., Leggett, J.K., 1986. Stratal extension in thrust footwalls, Makran accretionary prism: implications for thrust tectonics. AAPG Bulletin 70, 191-203.
Platt, J.P., Leggett, J.K., Alam, S., 1988. Slip vectors and fault mechanics in the Makran accretionary wedge, southwest Pakistan. Journal of Geophysical Research: Solid Earth (1978–2012) 93, 7955-7973.
Poldervaart, A., Eckelmann, F.D., 1955. Growth phenomena in zircon of autochthonous granites. Geological Society of America Bulletin 66, 947-948.
Rad, G., Droop, G., Burgess, R., 2009. Early Cretaceous exhumation of high-pressure metamorphic rocks of the Sistan Suture Zone, eastern Iran. Geological Journal 44, 104-116.
Rad, G.F., Droop, G., Amini, S., Moazzen, M., 2005. Eclogites and blueschists of the Sistan Suture Zone, eastern Iran: a comparison of P–T histories from a subduction mélange. Lithos 84, 1-24.
Remond, G., 1977. Applications of cathodoluminescence in mineralogy. Journal of Luminescence 15, 121-155.
Richards, J.P., Kerrich, R., 2007. Special paper: Adakite-like rocks: their diverse origins and questionable role in metallogenesis. Economic Geology 102, 537-576.
Richards, J.P., Spell, T., Rameh, E., Razique, A., Fletcher, T., 2012. High Sr/Y magmas reflect arc maturity, high magmatic water content, and porphyry Cu±Mo±Au potential: examples from the Tethyan arcs of Central and Eastern Iran and Western Pakistan. Economic Geology 107, 295-332.
Ricou, L.-E., 1994. Tethys reconstructed: plates, continental fragments and their boundaries since 260 Ma from Central America to South-eastern Asia. Geodinamica Acta 7, 169-218.
Rioux, M., Bowring, S., Kelemen, P., Gordon, S., Dudás, F., Miller, R., 2012. Rapid crustal accretion and magma assimilation in the Oman-UAE ophiolite: High precision U-Pb zircon geochronology of the gabbroic crust. Journal of Geophysical Research: Solid Earth (1978–2012) 117.
Roddaz, M., Said, A., Guillot, S., Antoine, P.-O., Montel, J.-M., Martin, F., Darrozes, J., 2011. Provenance of Cenozoic sedimentary rocks from the Sulaiman fold and thrust belt, Pakistan: implications for the palaeogeography of the Indus drainage system. Journal of the Geological Society 168, 499-516.
Rubatto, D., Gebauer, D., 2000. Use of cathodoluminescence for U-Pb zircon dating by ion microprobe: some examples from the Western Alps, Cathodoluminescence in geosciences. Springer, pp. 373-400.

Ruh, J.B., 2013. Dynamic Evolution of Thin-skinned Fold-and-thrust Belts: Field Study, Magnetostratigraphy and Numerical Modelling Applied to the Zagros and Makran Mountains (Iran). ETH.

Ruh, J.B., Gerya, T., Burg, J.P., 2013. High-resolution 3D numerical modeling of thrust wedges: Influence of décollement strength on transfer zones. Geochemistry, Geophysics, Geosystems 14, 1131-1155.

Saadat, S., Stern, C.R., 2011. Petrochemistry and genesis of olivine basalts from small monogenetic parasitic cones of Bazman stratovolcano, Makran arc, southeastern Iran. Lithos 125, 607-619.

Saccani, E., Delavari, M., Beccaluva, L., Amini, S., 2010. Petrological and geochemical constraints on the origin of the Nehbandan ophiolitic complex (eastern Iran): Implication for the evolution of the Sistan Ocean. Lithos 117, 209-228.

Sadeghian, M., Bouchez, J., Nedelec, A., Siqueira, R., Valizadeh, M., 2005. The granite pluton of Zahedan (SE Iran): a petrological and magnetic fabric study of a syntectonic sill emplaced in a transtensional setting. Journal of Asian Earth Sciences 25, 301-327.

Sahandi, M.R., Arshadi, S., Mahdavi, M., Huber, H., Ghorashi, M., Nogol-e Sadat, A.A., 1996. Iranshahr geological quadrangle map: 1:250,000 Geological Survey of Iran.

Salters, V.J., Hart, S.R., 1991. The mantle sources of ocean ridges, islands and arcs: the Hf-isotope connection. Earth and Planetary Science Letters 104, 364-380.

Samimi Namin, M., Arshadi, S., Aghanabati, A., 1992. Jahan Abad geological quadrangle map: 1:250,000. Geological Survey of Iran.

Samimi Namin, M., Arshadi, S., Aghanabati, A., 1994. Khash geological quadrangle map: 1:250,000. Geological Survey of Iran.

Samimi Namin, M., Behroozi, A., Arshadi, S., 1986. Narreh-Now geological quadrangle map: 1:250,000. Geological Survey of Iran.

Schnetzler, C., Philpotts, J.A., 1970. Partition coefficients of rare-earth elements between igneous matrix material and rock-forming mineral phenocrysts—II. Geochimica et Cosmochimica Acta 34, 331-340.

Shabani Goraji, K., 2015. Trace fossils in Eocene flysch deposits of Saravan and Mehrestan, southeast of Iran. WALIA journal 31, 11-18.

Siddiqui, M., 2004. Crustal evolution of Chagai-Raskoh arc terrane, Balochistan, Pakistan: Unpublished Ph. D. thesis, Peshawar, Pakistan, University of Peshawar.

Siddiqui, R., Haque, M., Hussain, S., 1988. Geology and petrography of Paleocene mafic lavas of Chagai island arc, Balochistan. Pakistan. Geol. Surv. Pak., IR 361, 18.

Sláma, J., Košler, J., Condon, D.J., Crowley, J.L., Gerdes, A., Hanchar, J.M., Horstwood, M.S., Morris, G.A., Nasdala, L., Norberg, N., 2008. Plešovice zircon—a new natural reference material for U–Pb and Hf isotopic microanalysis. Chemical Geology 249, 1-35.

Smale, D., 1990. Distribution and provenance of heavy minerals in the South Island: a review. New Zealand journal of geology and geophysics 33, 557-571.

Stocklin, J., 1968. Structural history and tectonics of Iran: a review. AAPG Bulletin 52, 1229-1258.

Sun, S.-S., McDonough, W.F., 1989. Chemical and isotopic systematics of oceanic basalts: implications for mantle composition and processes, in: Saunders, A.D., Norry, M.J. (Eds.), Magmatism in the ocean basins. Geological Society Special Publication, London, pp. 313-345.

Şengör, A., 1990a. A new model for the late Palaeozoic—Mesozoic tectonic evolution of Iran and implications for Oman. Geological Society, London, Special Publications 49, 797-831.

Şengör, A., Altıner, D., Cin, A., Ustaömer, T., Hsü, K., 1988. Origin and assembly of the Tethyside orogenic collage at the expense of Gondwana Land. Geological Society, London, Special Publications 37, 119-181.

Şengör, A.M.C., 1990b. Plate tectonics and orogenic system research after 25 years: a Tethyan perspective. Earth-science Reviews 27, 1-201.

Thirlwall, M.F., Walder, A.J., 1995. In situ hafnium isotope ratio analysis of zircon by inductively coupled plasma multiple collector mass spectrometry. Chemical Geology 122, 241-247.

Tilton, G., Hopson, C., Wright, J., 1981. Uranium-lead isotopic ages of the Samail Ophiolite, Oman, with applications to Tethyan ocean ridge tectonics. Journal of Geophysical Research: Solid Earth (1978–2012) 86, 2763-2775.
Tirrul, R., Bell, I., Griffis, R., Camp, V., 1983. The Sistan suture zone of eastern Iran. Geological Society of America Bulletin 94, 134-150.
Tirrul, R., Griffis, R.J., Camp, V.E., 1980. Geology of the Zabol Quadrangle, 1.250,000: Report submitted to the Geological and Mineral Survey of Iran, in: Iran, G.a.M.S.o. (Ed.). Geological and Mineral Survey of Iran, Tehran, p. 180 p.
Ueda, K., Gerya, T.V., Burg, J.P., 2012. Delamination in collisional orogens: Thermomechanical modeling. Journal of Geophysical Research: Solid Earth (1978–2012) 117.
Van Achterbergh, E., Ryan, C., Jackson, S., Griffin, W., 2001. Data reduction software for LA-ICP-MS. Laser-Ablation-ICPMS in the earth sciences—principles and applications. Miner Assoc Can (short course series) 29, 239-243.
Veiga-Pires, C., Moura, D., Rodrigues, B., Machado, N., Campo, L., Simonetti, A., 2009. Provenance of Quaternary sands in the Algarve (Portugal) revealed by U–Pb ages of detrital zircon. Sedimentary Processes, Environments and Basins: A Tribute to Peter Friend (Special Publication 38 of the IAS) 22, 327.
Verdel, C., Wernicke, B.P., Hassanzadeh, J., Guest, B., 2011. A Paleogene extensional arc flare-up in Iran. Tectonics 30, TC3008.
Vervoort, J.D., Blichert-Toft, J., 1999. Evolution of the depleted mantle: Hf isotope evidence from juvenile rocks through time. Geochimica et Cosmochimica Acta 63, 533-556.
Vervoort, J.D., Patchett, P.J., Blichert-Toft, J., Albarède, F., 1999. Relationships between Lu–Hf and Sm–Nd isotopic systems in the global sedimentary system. Earth and Planetary Science Letters 168, 79-99.
Vigny, C., Huchon, P., Ruegg, J.C., Khanbari, K., Asfaw, L.M., 2006. Confirmation of Arabia plate slow motion by new GPS data in Yemen. Journal of Geophysical Research: Solid Earth (1978–2012) 111.
von Rad, U., Delisle, G., Lückge, A., 2002. On the formation of laminated sediments on the continental margin off Pakistan. Marine geology 192, 425-429.
von Rad, U., Schaaf, M., Michels, K.H., Schulz, H., Berger, W.H., Sirocko, F., 1999a. A 5000-yr record of climate change in varved sediments from the oxygen minimum zone off Pakistan, Northeastern Arabian Sea. Quaternary research 51, 39-53.
Von Rad, U., Schulz, H., Khan, A.A., Ansari, M., Berner, U., Čepek, P., Cowie, G., Dietrich, P., Erlenkeuser, H., Geyh, M., 1995. Sampling the oxygen minimum zone off Pakistan: glacial-interglacial variations of anoxia and productivity (preliminary results, SONNE 90 cruise). Marine geology 125, 7-19.
von Rad, U., Schulz, H., Riech, V., den Dulk, M., Berner, U., Sirocko, F., 1999b. Multiple monsoon-controlled breakdown of oxygen-minimum conditions during the past 30,000 years documented in laminated sediments off Pakistan. Palaeogeography, Palaeoclimatology, Palaeoecology 152, 129-161.
Walker, R., Jackson, J., 2004. Active tectonics and late Cenozoic strain distribution in central and eastern Iran. Tectonics 23, TC5010.
Walker, R.T., Gans, P., Allen, M.B., Jackson, J., Khatib, M., Marsh, N., Zarrinkoub, M., 2009. Late Cenozoic volcanism and rates of active faulting in eastern Iran. Geophysical Journal International 177, 783-805.
Warren, C.J., Parrish, R.R., Waters, D.J., Searle, M.P., 2005. Dating the geologic history of Oman's Semail ophiolite: insights from U-Pb geochronology. Contributions to Mineralogy and Petrology 150, 403-422.
Weislogel, A.L., Graham, S.A., Chang, E.Z., Wooden, J.L., Gehrels, G.E., Yang, H., 2006. Detrital zircon provenance of the Late Triassic Songpan-Ganzi complex: Sedimentary record of collision of the North and South China blocks. Geology 34, 97-100.
Weltje, G.J., von Eynatten, H., 2004. Quantitative provenance analysis of sediments: review and outlook. Sedimentary Geology 171, 1-11.
White, R., Klitgord, K., 1976. Sediment deformation and plate tectonics in the Gulf of Oman. Earth and Planetary Science Letters 32, 199-209.

White, R., Powell, R., Holland, T., 2007. Progress relating to calculation of partial melting equilibria for metapelites. Journal of Metamorphic Geology 25, 511-527.
White, R.S., 1982. Deformation of the Makran accretionary sediment prism in the Gulf of Oman (north-west Indian Ocean). Geological Society, London, Special Publications 10, 357-372.
White, R.S., Louden, K.E., 1982. The Makran continental margin: structure of a thickly sedimented convergent plate boundary. Studies in continental margin geology 34, 499-518.
Woodhead, J., Hergt, J., Shelley, M., Eggins, S., Kemp, R., 2004. Zircon Hf-isotope analysis with an excimer laser, depth profiling, ablation of complex geometries, and concomitant age estimation. Chemical Geology 209, 121-135.
Yang, B., Luff, B., Townsend, P., 1992. Cathodoluminescence of natural zircons. Journal of Physics: Condensed Matter 4, 5617.
Zarrinkoub, M.H., Pang, K.-N., Chung, S.-L., Khatib, M.M., Mohammadi, S.S., Chiu, H.-Y., Lee, H.-Y., 2012. Zircon U–Pb age and geochemical constraints on the origin of the Birjand ophiolite, Sistan suture zone, eastern Iran. Lithos 154, 392-405.
Zeh, A., Gerdes, A., Klemd, R., Barton, J.M., 2007. Archaean to Proterozoic crustal evolution in the central zone of the Limpopo Belt (South Africa–Botswana): constraints from combined U–Pb and Lu–Hf isotope analyses of zircon. Journal of Petrology 48, 1605-1639.
Zuffa, G.G., 1985. Optical analyses of arenites: influence of methodology on compositional results, Provenance of arenites. Springer, pp. 165-189.

Acknowledgements

First, I would like to thank Jean-Pierre Burg for having me as a good PhD student. I am very grateful for all the support and the freedom to meander through different fields of geoscience. I learned a lot about geology during discussions and several field trips.

I want to thank Wilfried Winkler for introducing me to the topic of Provenance analysis and for his continuous supports during lab work and field work and the great time we had in the field.

Thanks go to Yani Najman and Barbara Carrapa for reviewing this thesis and being part of the committee.

Thanks are due to Albrecht von Quadt and Irena Peytcheva for their support on Rb-Sr, Sm-Nd chemical separations and isotopes analysis and their discussions and critical comments, Markus Wälle and Marcel Guillong for their assistance on the Laser ablation ICP-MS, Karsten Kunze for his assistance for CL and BSE imaging, Lydia Zehnder for her help with the XRF analyses, Frowin Pirovino for his help on sandstone thin sections and Silvia Spezzaferri and Carla Mueller for fossil determinations.

Many thanks to Regula Schaelchili and Ingrid Okanta for their help and support since the first day I arrived in Zurich.

I express my sincere thanks to Jonas Ruh, with whom I had so many good weeks in the field and during my PhD.

I am also very grateful to Sanjay Kumar Mandal for the great time we spent together and for interesting discussions.

Thanks to the Makran Team: Jonas, Marine, Daniela, Negar and Mohammad Faridi.

It was a pleasure sharing an office with Sanjay, Marine, Nima, Elizaveta, Maria, Shankar, Amaneh, Stephane and Barbara. Thanks for the great times we shared together work related and non-work related.

Furthermore, many thanks go to Sarah, Vangelis, Filippo, Claudio, Daniel, Anna, Stefania, Luca, Rolf, Pinar, Julien, Bjarne, Nil, Matteo, Marcel, Jan, Saima and my Iranian friends Hamed and Mohammadreza for the nice moments shared over these last four years.

Geological survey of Iran deserves special thanks for its contribution to this project. Thanks to Mohammad Reza Ghassemi (GSI) for his role in setting up the field project with our team, and for providing abundant logistical support throughout the project.

Last but not least, I want to thank my parents, Zolfenaz and Eltefat for all the support and patience.

Curriculum Vitae

Name	Ali Mohammadi
Birth	September 20th, 1979
Place of Birth	Marand (Iran)
Citizenship	Iranian

Education

2011-2015 **PhD in Structural Geology and Tectonics,** *ETH* Zurich, Switzerland

PhD's Thesis: Provenance analysis and detrital zircons: Keys to the tectonic setting of the Makran and Sistan basins in Iran

Committee: Prof. Dr. Jean-Pierre Burg
Prof. Dr. Wilfried Winkler
Prof. Dr. Yani Najman
Prof. Dr. Barbara Carrapa

2002-2005 **MSc in Geology (Sedimentology),** Tehran University, Iran

Master's Thesis: Holocene (?) Depositional history of Urmia Lake, based on the study of cores collected along the SH-K High way.

Committee: Prof. Dr. Abdol-Hossein Amini
Dr. Mostafa Shahrabi
Prof. Dr. Hosein Rahimpour Bonab

1997-2001 **BSc in Geology,** Tabriz University, Iran

Professional and Teaching Experience

2011-2015 **Research and Teaching assistant,** ETH Zurich, Switzerland.

2005-2011 **Sedimentologist,** Marine Geology Department, Geological Survey of Iran

2004-2005 **Geotechnical site manager,** Mandro-Chase Groups (Consulting Engineers), Iran

Languages

Turkish (Azerbaijani)	Mother Tongue
Turkish	Fluent in writing and speaking
Persian	Fluent in writing and speaking
English	Fluent in writing and speaking